MINIATURE ATOMIC BEAMS AND ITS APPLICATION IN QUANTUM OPTICS

A Dissertation
Presented to
The Academic Faculty

By

Bochao Wei

In Partial Fulfillment
of the Requirements for the Degree
Doctor of Philosophy in the
School of Physics

Georgia Institute of Technology

December 2022

MINIATURE ATOMIC BEAMS AND ITS APPLICATION IN QUANTUM OPTICS

Thesis committee:

Dr. Chandra Raman
School of Physics
Georgia Institute of Technology

Dr. Colin Parker
School of Physics
Georgia Institute of Technology

Dr. Ali Adibi
School of Electrical and Computer Engineering
Georgia Institute of Technology

Dr. Brian Kennedy
Department of Physics
Georgia Institute of Technology

Dr. Robert Wyllie
Georgia Tech Research Institute
Georgia Institute of Technology

Date approved: December 2, 2022

ACKNOWLEDGMENTS

Many thanks are due to my research advisor, Prof. Chandra Raman, for his tremendous support and guidance during my Ph.D. study. He patiently guided me in learning all the experimental skills and valuable knowledge in atomic physics. His unique insights and novel ideas always inspire me and help me in solving many challenges in my research. Besides research, I greatly appreciate our time spent together during the pandemic and his support for my future career.

I thank Prof. Ali Adibi, Prof. Brian Kennedy, Prof. Colin Parker, and Dr. Robert Wyllie for serving on my thesis committee and spending time reviewing my thesis. Special thanks to our collaborator Prof Ali Adibi for working patiently with me and educating me about nanophotonics. The cavity QED project is only possible with their excellent ideas and high-quality chips.

I would like to thank Ali Dorche for working with me and providing the microring resonators and the edge coupling chip. He also played a crucial role in the early stage of the slot resonator project. I thank Tianren Fan for helping with the microring resonator characterization and fiber cleaving. I also thank Ashkan Zandi, Xi Wu, Tyler Brown, Kirsten Masselink, and Muliang Zhu for their efforts and time in the slot resonator project. I am grateful for our collaborators Dr. Spencer Olson and Dr. Matthew Squires from AFRL. I thank them for supporting my research and providing the chance to study magnetically trapped cold atoms interacting with resonators on a chip. I thank Prof. Farrokh Ayazi's group for fabricating the silicon collimators, which inspired many following works.

I am deeply grateful to the members of the Raman lab. Chao Li is an excellent scientist who I learned extensively from. He was in charge of the silicon collimator project and fabricated many custom rubidium ovens for my research. We worked together a lot, and I learned many experimental skills and knowledge from him. Alex Crawford and I worked together on achieving the edge coupling in free space and the slot resonator project. She

iii

TABLE OF CONTENTS

LIST OF FIGURES

SUMMARY

The utilization of thermal atoms can enable further miniaturization and scalability of atomic devices and facilitate more applications of quantum information science in daily life. Thermal atomic beams can be easily generated and maintained compared with cold atoms. They also offer a longer coherence time and transverse Doppler-free interaction compared with thermal vapor. However, thermal atomic beams are rarely utilized in small-scale atomic devices. This thesis discussed novel approaches to generate miniature atomic beams and demonstrated their application in the field of quantum optics.

We first introduced the chip-scale collimator based on etching microchannels on a silicon wafer. The generated atomic beams were characterized, and a six-month continuous test was conducted to determine this device's long-term performance and robustness. In another approach, the collimator is fabricated by laser etching collimating channels on a stainless steel plate using femtosecond laser micromachining techniques. This collimator is then integrated into a rubidium dispenser to create an atomic source with an overall size of only 18 mm$\times$ 12 mm$\times$ 2 mm. Through time-of-flight measurements, we found that the collimator also greatly reduced the temperature of atoms emitted from the dispenser.

We then studied the combination of our chip-scale atomic beams with nanophotonic resonators to achieve strong coupling in the cavity QED field. Master equation simulations are implemented to understand the dynamics of flying atoms interacting with microresonators. The prospect and expected signal of magnetically trapped cold atoms interacting with resonators on-chip were also discussed. An edge coupling strategy was experimentally demonstrated to enable an efficient coupling between the free space laser beam and silicon nitride waveguide on the chip. Furthermore, the characteristics of a slot resonator designed for achieving unprecedented single atom cooperativity with atomic beams were discussed.

In another direction, a customized photon time tagging system with an accuracy of ± 50

ps is built. A novel two-fiber photon correlation method is implemented to characterize the velocity of single atoms in our miniature atomic beam. Through velocity selection, slow single atoms in our miniature atomic beams were isolated, and atoms with velocity 20 times smaller than the mean velocity were observed. Photon statistics from single atoms in our atomic beam were measured and studied theoretically. High values of the second-order and third-order correlation functions were found, which indicate its potential to be a source of photon pairs or triplets. Our observations showed the prospect of a bottom-up approach to building a thermal quantum system with trackable slow single atoms in an atomic beam.

CHAPTER 1

INTRODUCTION

1.1 Background and motivation

Alkali atoms offer an excellent platform for studying light-atom interaction and atom-atom interaction. Their simple electronic structure and energy levels allow scientists to easily control and manipulate them with lasers. The isolated alkaline atoms are well-defined quantum systems, and every atom of the same kind in the universe has identical dynamics that depend only on fundamental constants. This property leads to countless novel fundamental studies and quantum technologies in atomic optics.

One research direction in this field points to better control and precise manipulation of neural cold atoms in a laboratory environment. Some examples are quantum gas microscope [1, 2], trapped atoms with a cavity [3, 4, 5], and optical tweezers [6, 7, 8]. Ultra-cold atoms are utilized and are well-controlled and manipulated with minimum noise. However high-performance devices in this regime are usually bound to a laboratory environment due to their complicated system, core component size, and high power consumption. Along with the requirement for ultra-high vacuum (UHV), they are not ideal for miniaturization and scalability.

In another direction, tremendous efforts have been made in recent years to make portable, scalable, and chip-scale atomic devices[9, 10]. Their performance might not be the best compared with lab-environment setups, but they can provide adequate functionality to general users and make a more significant technological and economic impact.

In this direction, the semiconductor industry's technology, advances in microelectromechanical systems (MEMS), and the dramatic progress made in atomic optics are combined. Numerous research has been done to bring cold atoms into chip scale [10, 11]. Magneto-

optical traps (MOT) with a single laser beam are demonstrated with pyramidal mirror structures [12, 13], and planar diffraction patterns [14, 15, 16]. Microfabricated wires on the chip are used to create localized magnetic traps to control cold atoms and even a Bose-Einstein condensate (BEC) [17, 18]. But these localized traps still need to be loaded from a separate big vacuum apparatus.

The complication and high power consumption of magneto-optical traps (MOT) make them hard to miniaturize. In addition, because of the Helium permeation and long-lasting outgassing, ion pumps are usually connected to the package to meet the requirement of UHV for cold atoms. With these burdens, full chip scale cold-atom devices remain elusive [11].

On the other hand, more and more attention has been drawn to miniature atomic devices using thermal atoms. Thermal vapors can be easily generated and maintained using simple heaters, running current through alkaline dispensers [19] or focusing the laser beam on an alkali pill [20]. Many miniature atomic devices have been demonstrated using micro vapor cells [9], for example, miniature alkali vapor cell clocks [21, 22], laser frequency reference [23], magnetometers [24, 25, 26]. The micro vapors cells suffer from broad doppler broadening and fast decoherence from collisions with the wall. The inclusion of buffer gasses and wall coatings can mitigate the decoherence process but will create a much broader homogeneous broadening, and the characteristics can change over time [9, 11].

Atomic beams can achieve transverse doppler-free interactions with simple passive collimation. It has a longer coherence time compared with vapor cells and can also offer continuous operation and high atom density. These advantages of the atomic beams make them promising for miniature atomic devices. For example, atomic beam clocks can have a better performance than their vapor cell peers [9]. The atomic beams are also widely used in the quantum optics field to interact with cavity to measure vacuum Rabi splitting [27], achieve quantum memory[28], study Rydberg atoms [29, 30] ,test fundamental science [31, 32, 33] and study quantum computing [34, 35].

However, the atomic beam apparatus used to be bulky and not scalable, hindering its implementation in portable atomic devices. This thesis presents three important contributions we made in utilizing atomic beams for a new generation of miniature atomic devices. The first part of the thesis will discuss our work in making atomic beams miniature and versatile. With our chip-scale atomic beams, the third chapter of the thesis will discuss our efforts to demonstrate the scalable platform for strong atom-photon interaction with microresonators. Then, the fourth chapter will focus on our research in isolating and utilizing single atoms in a thermal atomic beam for chip-scale quantum devices.

1.2 Thesis outline

This thesis is organized as follows:

In chapter two, two approaches to generating miniature atomic beams are discussed, and the properties of the atomic beams are characterized. In the first approach, microchannels are etched on a silicon wafer to create highly collimated rubidium atomic beams. The guiding microchannels are precisely defined by lithography and can be tailored to specific applications. The lifetime and robustness of the device are tested over six months. The second approach combined femtosecond laser micromachining techniques and versatile alkali dispensers. A collimator is fabricated by laser drilling 46 collimating channels on a 600 μm thick stainless steel plate. The rubidium dispenser and collimator plate are bonded together by ceramic adhesive to create an atomic beam source with an overall size of only 18 mm$\times$ 12 mm$\times$ 2 mm. The temperature of the atomic beams is also much lower than the dispenser because of their collision with the collimator plate, which mitigated a big drawback of alkali dispensers. This approach provides less collimation compared with the first one, but it does not require special handling of pure rubidium, and the overall size is much smaller.

The third chapter of the thesis will focus on the efforts to combine our chip-scale atomic beams with nanophotonic resonators to achieve strong coupling in the cavity QED field.

Our chip-scale atomic beams can be delivered by lithographically defined microchannels. We proposed to integrate the atomic channels and microresonators on the same silicon wafer, and the nanometer level alignment is naturally satisfied. High quality factor microring resonators were fabricated by Ali Dorche from Prof Ali Adibi's group and were carefully characterized. Extensive master equation simulations are implemented to understand the dynamics of flying thermal atoms with resonators. We studied the expected signals and possible constraints for experiments. Besides thermal atoms, simulations were conducted to study the dynamics of trapped cold atoms with microring resonators. Both grating coupling and edge coupling are explored to couple light in and out of the resonators. An edge coupling method was demonstrated to enable an efficient coupling between the free space laser beam and silicon nitride waveguide on the chip. Besides resonators with a microring structure, horizontal slot resonators are also studied. More simulations and experimental efforts are discussed to understand its interaction with atomic beams and to extract the figure of merit for cavity QED — single atom cooperativity.

In the fourth chapter, the experimental setup we built for enabling single-photon time tagging and correlation analysis is discussed. Single atoms in our miniature atomic beams are isolated, and their photon statistics are characterized. We used velocity selection to select the slow atoms in a thermal atomic beam and implemented a novel two-fiber photon correlation method to measure their velocity. Our correlation method is able to distinguish the slow atoms with velocities around 15 m/s, which constitute a ratio of only 10^{-6} of the thermal atomic beam. Photon statistics from single atoms in our atomic beam were also measured by using the Hanbury Brown and Twiss configuration. We observed high values of the second-order and third-order correlation functions, which indicate its potential to be a source of photon pairs or triplets for quantum optics. The theoretical analysis of the observed data was explained. Monte Carlo wave function simulations mimicking our experiment were also conducted to compare with our theory. Our work paves the way for a bottom-up approach to building thermal quantum systems.

CHAPTER 2

MINIATURE ATOMIC BEAMS FOR PORTABLE ATOMIC DEVICES

2.1 Introduction

Generating thermal atomic beams is one of the first approaches scientists utilized to study atoms' properties and their interactions with external fields. It is a great atomic source that can provide continuous, directional, and isolated atoms that do not suffer from transverse Doppler shifts and atom collisions.

Usually, to generate an alkali atomic beam, an oven containing pure alkali metals will be heated, and high atomic vapor pressure is created. Then the vapor passes through a collimator to form a highly directional beam. Two typical types of collimators often used by atomic physicists are shown in Figure 2.1. The first type is constructed by aligning two small coaxial apertures in a bigger tube. The vacuum wall between two apertures is usually actively cooled to low temperatures. As a result, the off-axis atoms will be trapped on the cold walls, and only on-axis atoms can pass. Recirculating ovens [36, 37] are designed to cool the off-axis atoms into liquid form and return them to the oven. However, most of these designs add too much complexity to the oven.

The second type of oven composes of one or an array of long channels aligned in the same direction. The channels are heated to the same or higher temperature than the oven. Off-axis atoms hit the wall, are diffusively reflected in all directions and have a high probability of returning to the source oven. The bigger the divergent angle, the higher the probability of returning to the source. The collimation is thus achieved, and the divergence angle HWHM (half-width at half-maximum of the flux angular distribution) $\theta_{1/2}$ roughly equals to $0.8d/L$ [38, 39]. The total number of atoms enters the entrance of a channel per second equals $\frac{1}{4}n\bar{v}A_s$, where n is the atom density in the oven, $\bar{v}$ is the average atom
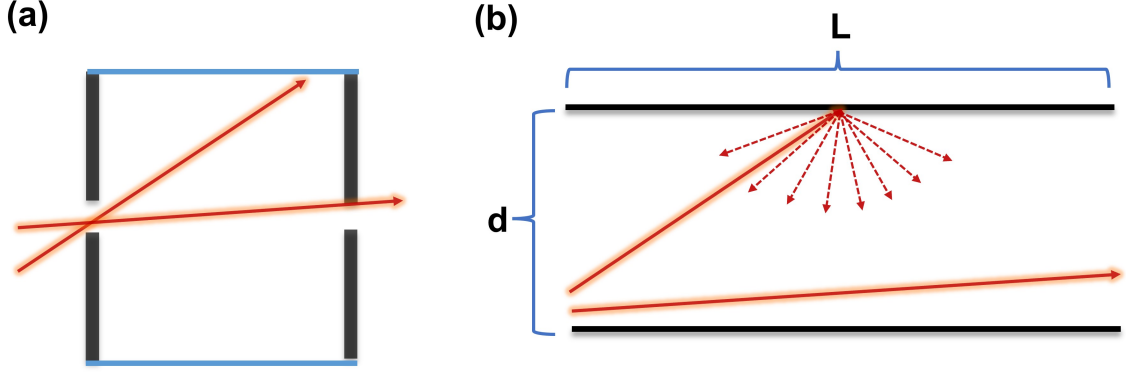
Figure 2.1: (a) Aperture collimator. The wall between two apertures is usually cooled to a low temperature to trap the off-axis atoms. (b) Channel collimator. The off-axis atoms will collide with the wall, and diffusive reflect in all directions.

velocity, and A_s is the cross-section area of the channel. For a transparent channel which means the mean free path of the atom is longer than the channel length L, the total flux exiting the channels is [39]:

$$F = \frac{1}{4}Wn\bar{v}A_s \tag{2.1}$$

With W being the transmission probability or Clausing factor [40]. The factor W depends only on the geometry of the channel, the aspect ratio (d/L). For circular channels $W \approx \frac{4d}{3L}$. For a channel collimator with an aspect ratio of $d/L = 1/30$, we get $W \approx 0.04$, meaning that around 96% atoms are reflected back to the source while the on-axis flux remains the same. Since for most of the applications, only on-axis flux is useful. Channel collimators provide a huge advantage because they will elongate the oven lifetime by a factor of $1/W \sim L/d$ without harming the performance. Capillaries formed by stacking thin stainless tubes have been used as the collimator to extend the estimated lifetime of a lithium oven to 50 years [41].

The mentioned collimator designs are mostly bulky and used together with big vacuum apparatus. In the following sections, we will discuss our efforts in building miniature and scalable channel collimators for portable atomic devices with a long lifetime.
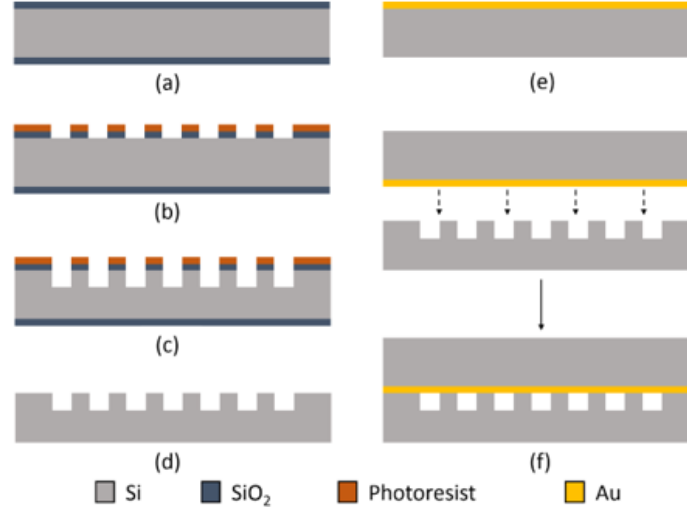
Figure 2.2: Fabrication procedure. (a): Grow Oxide (b): Pattern PR and Etch Oxide (c): Silicon DRIE (d): Strip PR/oxide mask (e): Evaporate Au (f): Si/Au Eutectic Bonding. Figure taken from Ref [38].

2.2 Atomic beams on silicon chips

When I joined the lab, Chao Li was in charge of the silicon collimator project. Planar collimation arrays in silicon are fabricated to create chip-scale collimators that allow for great flexibility and control over the array elements. Besides the normal long-channel design, a special cascaded collimator is achieved by creating two gaps on the channels to allow off-axis atoms to escape.

The properties of the generated beams are measured and analyzed. I helped with some of the characterizations. Then, I conducted the lifetime and robustness test of this silicon collimator. The results of our silicon collimator have been published in Ref [38] and Ref [42], in which I am a co-author. Some of the sentences and figures in this chapter are from these two publications.

The fabrication of the silicon collimator is done by our collaborator—Prof. Ayazi's group. The fabrication process is described in Ref [38], and I repeated it here for the reader's convenience. The fabrication process (see Figure 2.2) includes two silicon wafers bonded together to form an enclosed structure. First, about 2 μm of oxide was grown on

(a)   **(b)**
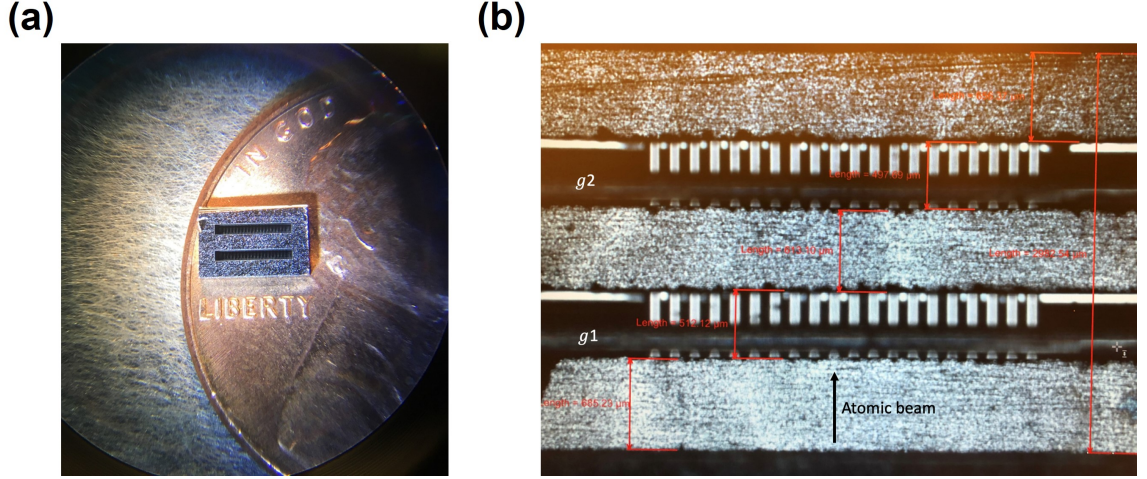
Figure 2.3: (a) The image of a cascaded collimator with a penny. (b)Microscope image of the cascaded collimator in the top view showing the two gap regions g1 and g2, where the capping wafer was removed. Atoms propagated through the channels in the direction of the arrow. Some of the channel walls are still visible after dicing due to the asymmetry of the dicing blade. The widths of the gaps g1 and g2 are around 500 μm. Figure taken from Ref [38].

the base wafer (a). Then, about 3 μm of positive photoresist was patterned, and the oxide was etched in an RIE process, which formed the mask for the collimators (b). After the oxide etching, the collimators were etched using the Bosch DRIE process up to the required depth of 100 μ m (c). The wafer was then cleaned, and the remaining oxide was etched away in 49% HF solution to form the completed base wafer (d). Gold was evaporated on the capping wafer (e). The two wafers were then bonded together using a Si–Au eutectic bond at 450 °C. Finally, the different dies were diced across the wafer according to the length of the collimators to give us a completely sealed structure with access to the two ends of the collimator lengths (f). The cascaded collimator was realized by partially dicing through the bonded wafers in two places (see Figure 2.3(b)). The diced region widths were g1, g2 = 510, 500 μ m. Some of the channel walls are still visible after dicing due to the asymmetry of the dicing blade. The image of the cascaded collimator with a penny is shown in Figure 2.3 (a). The size of the collimator is only 1 mm $\times$ 5 mm $\times$ 3 mm ($h \times w \times l$).

Figure 2.4 (c)-(d) shows the front-view images of the bonded collimator and Figure 2.4

(e) shows the scanning electron microscope images of the fabricated channels before bonding. Each channel has a length $L = 3$ mm and a cross-section area of $100\ \mu$m $\times\ 100\ \mu$m. The bonding of the two wafers provided an array of long channels with an aspect ratio of $L/d = 30$. One end of the array was connected to a rubidium source and the output flux of the channels were probed on the other end in the vacuum using free space fluorescence detection. Figure 2.4 (b) shows a top view fluorescence image of 20 individually visible atomic beams generated by a cascaded collimator.

Figure 2.4: The planar concept for atomic beams. (a) In a fully planar vision, atoms propagate from a source region into a planar device that has been lithographically etched into a silicon chip. Shown schematically are multiple sequential operations, including beam formation by collimation, laser deceleration and/or cooling, atom interferometry or other sensing protocols using guided atoms, followed by detection. Blue arrows indicate the direction of the atomic beam propagation. (b) Rubidium atom beam collimation as the first nontrivial element demonstrated in this work. The adjacent image shows the experimentally observed fluorescence output of 20 individually resolved collimation channels. (c) Optical and (d) scanning electron micrograph (SEM) end images of the channels show the etched base wafer and sealing capping wafer. (e)–(g) SEM top images before bonding the capping wafer showing microchannels that (e) collimated the atomic beam, (f) produced a focusing beam, and (g) created two beams propagating at a relative angle of 12 degrees. Channel dimensions in (e) are $100\ \mu$m $\times\ 100\ \mu$m $\times\ 3$ mm (h $\times$ w $\times$ l) dimension, with 50 μm wall thickness between channels. Figure taken from Ref [38].

Figure 2.5: A picture of our atomic oven for our silicon collimators using rubidium ampoules. A copper tube going through an aluminum blank KF40 flange forms the main part of the oven. The parts on the right of the flange will be in the vacuum. A rubidium ampoule has been inserted into the copper tube near the left end. The left end of the tube has been pinched off to make a seal. Rubidium vapors can be generated by heating the copper tube on the left. Image taken by Chao Li.

2.2.1 Set up and fluorescence spectroscopy

We used pure rubidium metal contained in sealed ampoules to introduce rubidium vapors into the silicon collimator chip. A custom-made oven is designed to accommodate the silicon chip and the ampoule. As shown in Figure 2.5, a 101 copper tube going through a KF40 flange is used as the oven body. After loading the ampoule, the left end of the tube is sealed by pinching it off with the cold welding technique. The right end of the tube is terminated with a special holder to hold the silicon collimator. A nichrome heater is wrapped around the holder to keep the collimator temperature higher than other parts of the oven to prevent clogging. After installing it in the vacuum chamber and pumping the chamber to a high vacuum, the copper tube near the ampoule is clamped down with pliers to break the ampoule. In order to remove possible cold spots, thermal breaks with low thermal conductivity (Ultem plastic) are also used between the copper tube and the KF flange.

The oven with our collimator is installed in a 6-inch by 6-inch cubic vacuum chamber

that can reach 10^{-7} torr. The oven is heated to 100 °C to generate enough rubidium vapor pressure. A Toptica external cavity laser is used to probe the atoms at ^{87}Rb D2 line. The probe laser is kept linearly polarized by passing a $\lambda/2$ waveplate and a polarizing beam splitter. The laser is placed to probe the atoms only $\approx$6 mm away from the channels to capture the atoms with all angular divergence. Careful alignment is done with the probe beam to maximize the fluorescence peak height and minimize the full-width half maximum of the fluorescence spectrum. By doing this, we make sure the probe beam is perpendicular to the atomic beam to eliminate the effect of the longitudinal velocity distribution. Atomic fluorescence was collected by two f = 75 mm 2-inch diameter plano-convex lenses and then focused onto a photodiode (Thorlabs DET100A2). The photocurrent is amplified by a current preamplifier (DL Instrument Model 1211, with a Gain of 10^8 V/A) realizing a rise time of 0.04 ms. The laser is scanned at a frequency of 5 Hz to make sure the signal rise time is much longer. Both the saturated spectroscopy from the rubidium reference cell for the frequency calibration and the fluorescence spectrum from the atomic beam are recorded and averaged over 64 traces by an oscilloscope (TDS2024C).

The spectral data of the ordinary collimator and the cascaded collimator is shown in Figure 2.6(a). They are taken with the same oven temperature, laser size, and laser power (saturation parameter s equals 1.2). Multiple hyperfine resonances between the ^{87}Rb $5S_{1/2}$, F = 2 ground state and the $5P_{3/2}$, F'= 1,2,3 levels appeared as narrow peaks as a function of the probe frequency. The strongest such peak is the F'= 3 level, centered at zero frequency offset. The natural linewidth of this transition is 6 MHz, while our laser linewidth is less than 1 MHz. The width of this peak is wider because of the power broadening and the Doppler broadening due to the transverse velocity distribution of the emitted atoms. For the single straight collimator, this peak has a full width half maximum (FWHM) of 42 MHz, but contains broad wings visible up to 400 MHz detuning.

As a comparison, the data for the cascaded collimator only has a FWHM of 18 MHz. The collimation is greatly improved, and the off-axis atoms are suppressed with our cas-
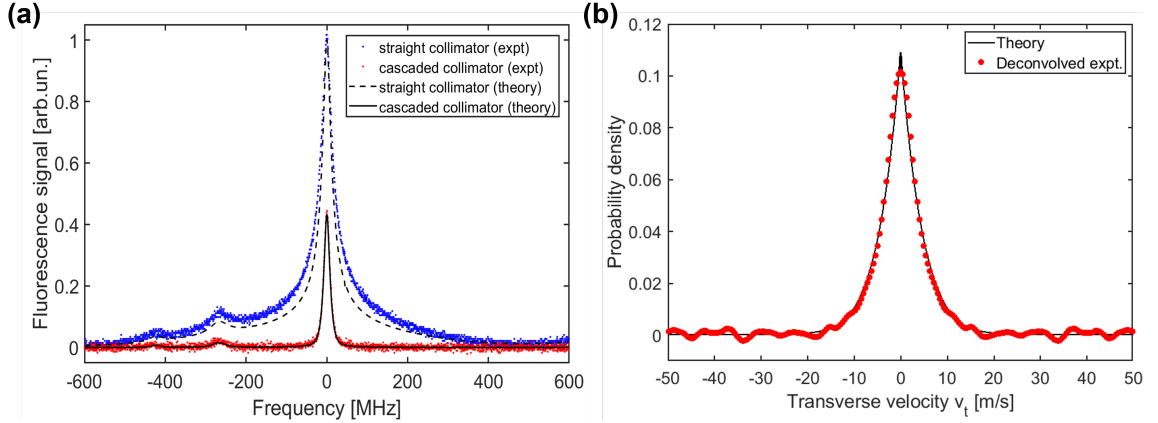
Figure 2.6: (a) Measured atomic fluorescence spectra versus excitation laser frequency showing the transverse Doppler distribution of the atomic beam. Peaks at 0, 267, and -424 MHz correspond to transitions between the hyperfine F = 2 ground level and F' = 3, 2, 1 excited levels in ^{87}Rb, respectively. The data from the ordinary collimator (blue) and the cascaded collimator (red) are shown. The saturation parameter is around 1.2. Solid and dashed lines are corresponding theoretical calculations. (b) Transverse velocity distribution of the cascaded collimator derived from the measurement by deconvolution, along with the theoretical prediction from Monte Carlo simulations. Figure taken from Ref [38].

caded design. Using a deconvolution procedure, we estimated that the transverse Doppler broadening had a HWHM = 4 m/s, which implies a very narrow beam divergence angle $\theta_{1/2}$ = 0.013 rad. The transverse velocity distribution by deconvolution is shown in Figure 2.6 (b). The details of the theory and more data can be found in Ref [38].

2.2.2 Long-time characterization

A crucial metric for any atomic source is the lifetime. For portable atomic devices, their lifetime is usually determined by the lifetime of the oven because it is very difficult to change the oven without introducing contamination or degradation. There are two concerns about this silicon collimator that we would like to address.

First, the microchannels have a cross-section of 100 μm $\times$ 100 μm and a length of 3 mm. Such a small cross area and a big aspect ratio (30) bring concerns that the rubidium atoms may accumulate on the wall and clog the channels. Second, the silicon wall between each channel is only 50 μm thick. The thickness of the gold layer for Si/Au Eutectic
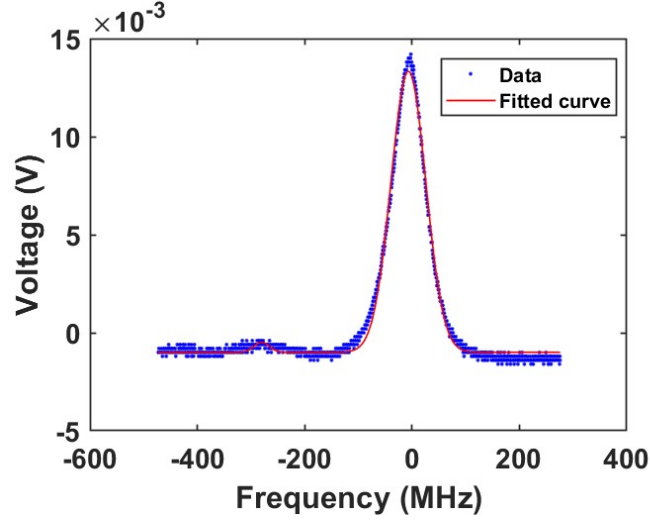
Figure 2.7: A typical fluorescence spectrum with 100 °C oven temperature. The blue dots are the fluorescence signal. The red curve is the fitted curve using two Gaussian peaks centered at 0 and -267 MHz.

bonding is only around 1 μm. Therefore, the robustness of the delicate structures under intense rubidium vapor exposure also needs to be tested. We performed a lifetime test under continuous operation for a period of 6 months at various fixed temperatures with a focusing type collimator as shown in Figure 2.4 (f). The focusing-type collimator has 29 channels pointing to a focal point that is 2 cm away from the nozzle exit, with a maximum angle of 0.1 rad. It doesn't have the gaps as the cascaded collimator. We used this focusing type collimator because its structure is essentially the same as other types of collimators, and it is not needed for other projects. The same cubic vacuum chamber is used, and a stainless steel plate with a 9 mm diameter hole in the center is placed around 2 cm away from the collimator. The size of the stainless steel is 9 cm in width and 5 cm in length. The plate allows the atomic beam to pass but will block the potential vapor build-up in our probe region over time. The laser is placed 6 cm away from the collimator. The laser and the collecting setup are the same as what we mentioned in subsection 2.2.1. The laser power was kept the same throughout the test, with a saturation parameter of 3.9.

We recorded the fluorescence spectrum around three times per week to monitor both the peak height and the spectrum shape. We also used a CCD camera to take an image near the

13

(a) **(b)**
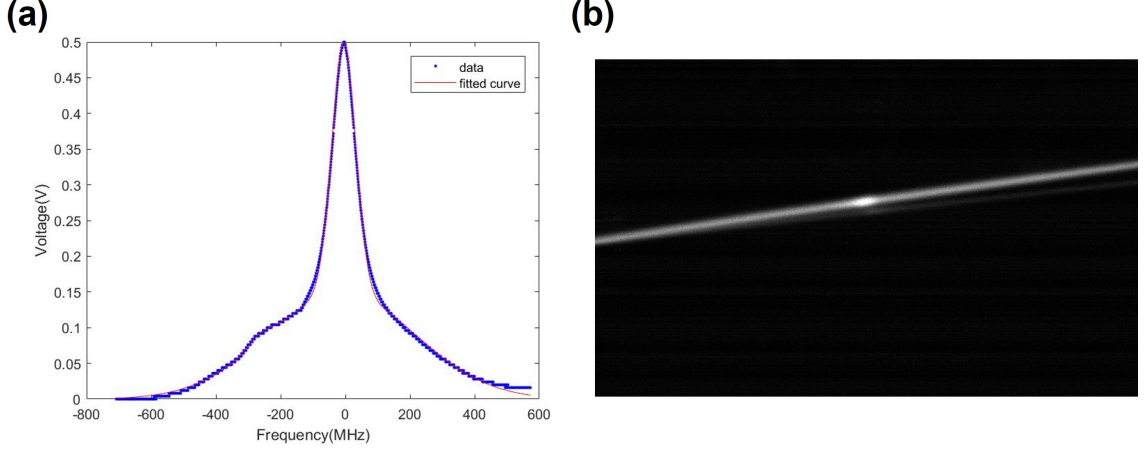
Figure 2.8: (a) A fluorescence spectrum with 150 °C oven at 1450 hours. The total signal is fitted with three Gaussian peaks representing the contribution from vapor, atomic beams F=2 to F'=3, and F=2 to F'=2, the fitted amplitudes are 0.1591, 0.3840 and 0.0077 respectively. (b) A CCD camera image of the vapor and the atomic beam with 150 °C oven at 2050 hours. The vapor component was getting higher. The brighter region in the center is the beam component, and the vapor makes the laser path visible.

collimator to check the output of every individual microchannel. The oven temperature was set at 100 °C at the beginning and increased to 125 °C at 1150 h and 150 °C at 1320 h. The vapor accumulated quickly at 150 °C. Thus, we reduced the temperature back to 125 °C at 2390 h to lower the vapor pressure. Figure 2.7 shows a typical spectrum with 100 °C oven where the vapor is negligible. The ^{87}Rb D2 line F=2 to F'=3 is centered at zero frequency. The FWHM of the peak is much wider compared with the result in subsection 2.2.1 because the focusing type collimator makes the longitudinal velocity component contribute to the spectrum. On the other hand, the tail is not as pronounced compared with the ordinary collimator because the laser beam is much farther away from the collimator (6 cm vs 6 mm), and atoms with large divergent angles won't be detected. The height and HWHM of the F=2 to F'=3 peak are extracted by fitting the spectrum with two Gaussian peaks. One Gaussian peak centered at 0 frequency represents the contribution from F=2 to F'=3, and another Gaussian peak center at 267 MHz represents the contribution from F=2 to F'=2. When the oven was increased to 150 °C, the emitted atoms fully coated the inner surface of the vacuum chamber, and the background rubidium vapor pressure slowly built up. As

14

(a)

(b)
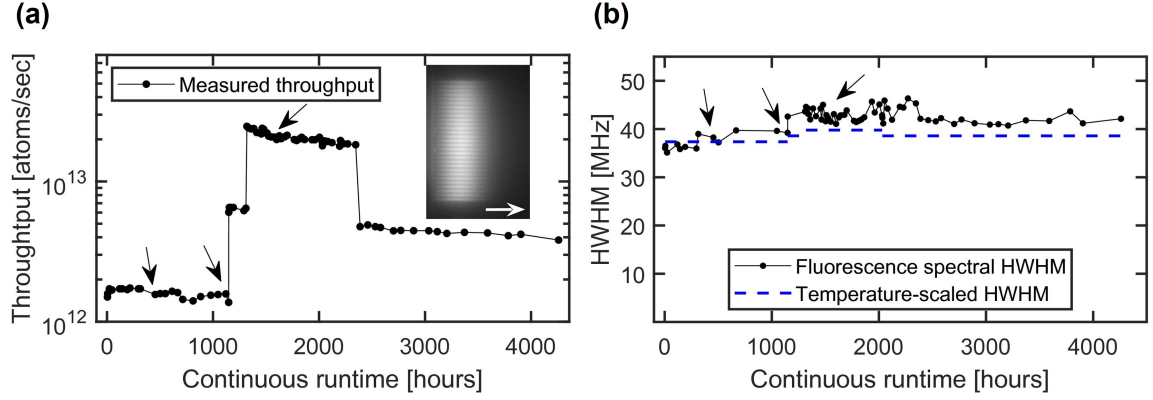
Figure 2.9: (a) The calculated total throughput over the continuous test. The temperature is 100 °C from 0 to 1150 h, 125 °C from 1150 to 1320 h, 150 °C from 1320 to 2390 h, and back to 125 °C from 2390 h to the end. (b) Black dots connected by lines show the measured HWHM of the atomic beam fluorescence spectra. The blue dashed lines show the benchmarks that are scaled to 125 °C and 150 °C using the averaged value at 100 °C.

shown in Figure 2.8, the vapor component is handled by adding another Gaussian peak centered at zero and a HWHM around 260 MHz into the fitting process. The heights and HWHMs of all three Gaussian peaks are fitted and extracted from the signal when the vapor component started to show up. To prove that the vapor was not from a broken collimator, we turned the oven off for a day to get the vapor pumped away. Then in the next spectrum data, the vapor component became negligible again.

A camera image as an inset in Figure 2.9 (a) for the atomic beam fluorescence right after the channel exit indicates all 29 channels are working well (no clogging). The white arrow on the inset marks the propagation direction of the atomic beams. Three black arrows mark the time at 454, 1120, and 1510 hours in Figure 2.9 (a) and Figure 2.9 (b) when we took camera images for the collimator output. None of the channels was clogged or showed any problem.

The total throughput vs time is shown in Figure 2.9 (a). The details of how to calculate the total throughput will be discussed in the next section. As we mentioned above, the oven temperature is set to 100 °C at the beginning, 125 °C at 1150 h, 150 °C at 1320 h, and 125 °C again at 2390 h. Before we had to stop and disassemble the setup for another

project, this oven had run for over 4200 h, and none of the microchannels showed any sign of clogging. It can be noticed in Figure 2.9 (a) that the throughput is decaying slowly within the same temperature, which might result from the migrating of Rb inside the oven from hotter spots to colder spots. The coating of Rb on the vacuum windows over time and the drift of laser alignment may also contribute to this decaying effect. Since the flux is around an order of magnitude higher at 150 °C and three times higher at 125 °C, our results imply a continuous operation time at 100 °C of over 19000 hours, more than two years, without failure. This test proved that our microfabricated atomic beams are reliable and robust at different temperatures and can have a very long lifespan. This validated the advantage of long-channel collimators. Because the off-axis atoms will tend to return back to the source, the transmission probability or Clausing factor W in $\frac{1}{4}Wn\overline{v}A_s$ makes the lifetime $1/W$ times longer.

While the total flux might be constant, an open question is whether the collimator angular divergence might experience long-term drifts. To address this, in Figure 2.9(b), we have plotted the extracted HWHM of the measured fluorescence spectrum over the same, roughly six months, time period. It is seen to be quite constant over this time period, ruling out severe long-term degradations or changes in the MEMS fabricated structures due to interaction with rubidium. For reference, we have plotted dashed lines that show the $\sqrt{T}$ variation of the most probable atomic velocity, where T is the temperature in Kelvins. If the transverse velocity distribution is only influenced by temperature, the HWHM should follow the dashed line.

Our data after 1320 h are approximately 10% higher than this line. The possible reason is that the mean free path of the atoms is smaller than the 3 mm channel length when the temperature is at 125 °C and 150°C [42]. The collisions between atoms will make the transverse distribution broader. But their influence, if any, is relatively stable over time.
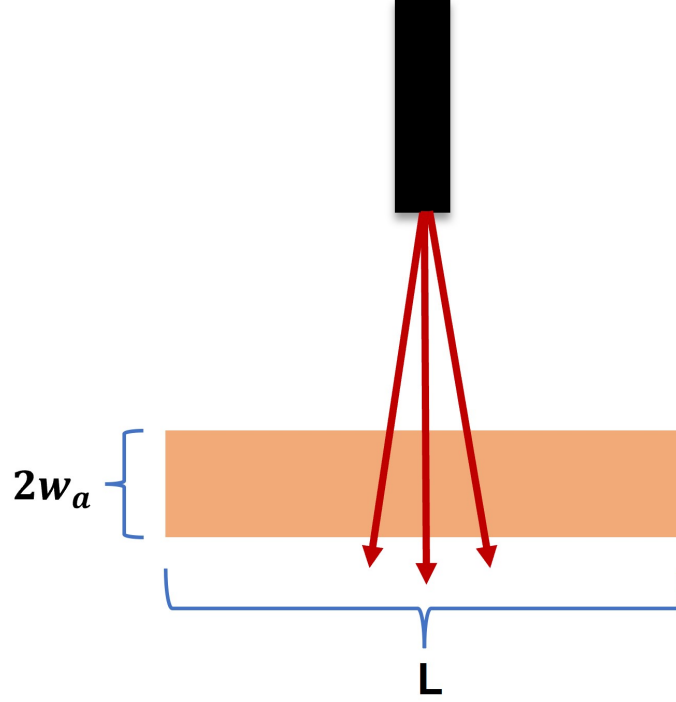
Figure 2.10: The diagram for atomic beams and our collection region.

2.2.3 Total throughput calculation

In this section, we will discuss the procedure to calculate the total throughput from the spectrum data. As shown in Figure 2.10, our laser beam and the imaging system's field of view define a collection region where atoms are excited, and the emitted photons are collected by our photodiode. The laser beam has a Gaussian beam waist radius w_a along the atomic beam direction and w_b in the perpendicular direction (into the page). The diameter of the field of view defined by the imaging system is L. The volume of the collection region is $V = \pi w_a w_b \cdot L$, and the cross-section of the region is $S = 2 w_b L$. We will show later that L doesn't affect our calculation.

The photon scattering rate for one atom is [43]:

$$R_{sc}(w) = \frac{\Gamma}{2} \frac{s}{1 + s + 4(\frac{w - w_0}{\Gamma})^2} \tag{2.2}$$

Where $\Gamma \approx 2\pi \times 6.06$ MHz is the natural linewidth, w_0 is the resonance frequency, w

17

is the laser frequency, s is the saturation parameter. The total scattering photon rate is a convolution between the transverse velocity distribution ($p(v_t)$) and the scattering rate [44]:

$$\gamma(w) = \overline{n} \cdot V \int_{-\infty}^{\infty} dv_t p(v_t) R_{sc}(w - kv_t) \tag{2.3}$$

Where $\overline{n}$ is the averaged density of atoms in the collection volume V, k is the wavevector for the laser. The detected voltage on our oscilloscope is:

$$V_{out}(w) = \hbar w_0 \gamma(w) \eta R_{resp} G = \hbar w_0 \eta R_{resp} G \cdot \overline{n} \cdot V \int_{-\infty}^{\infty} dv_t p(v_t) R_{sc}(w - kv_t) \tag{2.4}$$

Where $R_{resp} = 0.6$ A/W is the responsivity of the photodiode, $G = 10^8$ V/A is the gain of the current amplifier, and $\eta = 1.2\%$ is the overall photon collection efficiency that is subjected to the transmission of optics and the solid angle over which the emitted photons could be collected. $V_{out}(w)$ is the spectrum data shown in Figure 2.7. By using the whole spectrum data $V_{out}(w)$ and combining a Fourier transform routine with Tikhonov regularization [38], we can do a deconvolution and get the velocity distribution $p(v_t)$. With the extracted velocity distribution, we can calculate an averaged photon scattering rate at zero detuning:

$$\overline{R}_{sc}(w_0) = \int_{-\infty}^{\infty} dv_t p(v_t) R_{sc}(w_0 - kv_t) \tag{2.5}$$

Then, we can calculate the average atom density $\overline{n}$ by just utilizing the voltage at zero detuning $V_{out}(w_0)$:

$$V_{out}(w_0) = \hbar w_0 \eta R_{resp} G \cdot \overline{n} \cdot V \cdot \overline{R}_{sc}(w_0) \tag{2.6}$$

The atom flow (atoms/s) is $F = \overline{n} \cdot S \cdot \overline{v}$, where v is the averaged velocity $\sqrt{\frac{8k_B T}{\pi m}}$ (k_B Boltzmann constant,T oven temperature, m rubidium mass). Thus we can write the measured flow as:

$$\frac{V_{out}(w_0)}{\hbar w_0 \eta R_{resp} G \cdot V \cdot \overline{R}_{sc}(w_0)} \cdot S \cdot \overline{v} \tag{2.7}$$

By using $V = \pi w_a w_b \cdot L$ and $S = 2w_b L$, we get the measured flow:

$$F = \frac{V_{out}(w_0) \cdot \overline{v}}{\hbar w_0 \eta R_{resp} G \cdot \frac{\pi w_a}{2} \cdot \overline{R}_{sc}(w_0)} \qquad (2.8)$$

After getting the measured flow, we still need the fraction χ of the total throughput travel through our collection volume to calculate the total throughput. Monte–Carlo simulations with our collimator structure and probing configuration are done by utilizing the Molflow+ package [45]. The collection region is the cylindrical region formed by our probe laser. By counting the atoms entering our collection region and dividing it by the total emitted atoms (total throughput in the simulation) from our channels, we can get the fraction of the total throughput that flies into our collection volume χ. The χ is around 1.2% with the configuration of our long-time test because the probe laser is 6 cm away from the collimator. Furthermore, the measured flow is the ^{87}Rb atoms in F=2 ground states. For natural rubidium samples, ^{87}Rb has an abundance of 27.83%. The ratio of ^{87}Rb atoms in F=2 ground states is $5/8$. By setting $\kappa_r = 27.83\% \times 5/8$ to be the total ratio, we get the total throughput:

$$F_{total} = \frac{F}{\chi \cdot \kappa_r} \qquad (2.9)$$

2.2.4   Summary

In summary, we have discussed atomic beam collimators on silicon chips, the first element in a fully planar atomic device for integrated atomic quantum technologies. The cascaded collimator design offers a very narrow beam divergence angle $\theta_{1/2} = 0.013$ rad within a 3 mm distance. Our collimators can greatly reduce the size of quantum devices that utilizes atomic beams. The long-time performance is also tested by running continuously for over 4200 hours. The robustness and reliability of the collimator make it suitable for portable devices like atomic clocks, gyroscopes, atom-photonic devices, etc.

2.3 Miniature atomic beams with alkali dispensers

We have discussed our silicon collimators in the last section. But one drawback for the silicon collimators is that the size of the associated oven is still big (see Figure 2.5). The length of the oven is around 20 cm, and it is hard for mass production. The ampoule can contain a large amount of rubidium which provides a very long lifetime, but it can also make the whole oven more complicated and bulky.

Therefore, although the collimator has been made miniaturized, a good atomic source besides rubidium ampoules is also vital for portable atomic devices. Alkali-containing compounds can also produce pure alkali vapor by reacting with reducing agents at a high temperature. For example, rubidium pills are an alternative atomic source based on rubidium chromate. It can be handled in the ambient air and activated by heat. Many researchers are able to put the alkali pills in bonded silicon-glass microcells and use a high-power laser for activation [11]. If $ZrAl_2$ is used as the reducing agent, the chemical reaction below can happen with heat to release pure rubidium vapor [11]:

$$2Rb_2CrO_4 + ZrAl_2 \rightarrow 4Rb + Cr_2O_3 + Al_2O_3 + ZrO_2 \tag{2.10}$$
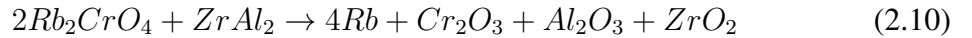
Alkali metal dispensers [46] holds a mixture of rubidium chromate and a reducing agent within a metal container, which has a trapezoidal cross-section with a small slit to allow alkali metal vapor to exit (see Figure 2.11). They are sold commercially, usually for alkali coating applications, such as producing photocathodes. These dispensers have been adapted by atomic physicists to load magneto-optic traps (MOT) [47, 48, 49, 19]. A current of several amps is passed through the dispenser to generate heat. Once the temperature is high enough, the chemical reduction reaction process will start producing alkali vapor. The reaction rate is sensitive to the temperature. Thus changing the supply current can easily control the atom flux. They are small in size and can be handled in ambient air. The active area of the dispenser we used (SAES RB/NF/3.4/12 FT 10) is around 6 mm $\times$1 mm. These

«**FT** type»

FT = terminal length 10
A = active length 12-17-25

All dimension in millimetres
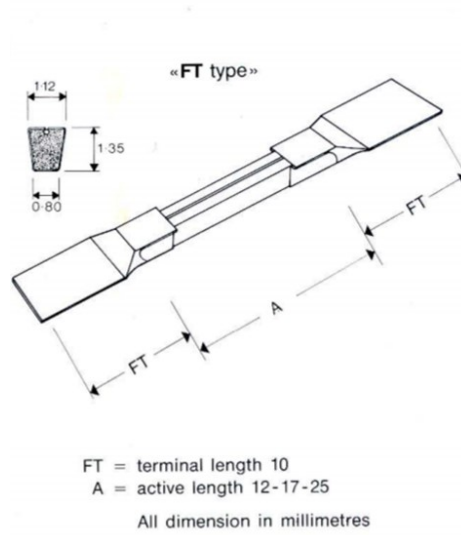
Figure 2.11: A drawing of the SAES alkali dispenser from ref [46].

properties can significantly reduce the complexity of the atomic oven and make it suitable for miniature atomic devices.

However, the high temperature needed to initiate the reactions that produce alkali vapor (550-850 °C) creates significant challenges for integration into a chip environment, as they present a considerable source of radiative heat that can influence other chip components. Moreover, at such elevated temperatures, the emitted atomic flux from a dispenser has a substantial longitudinal velocity and must first thermalize with room temperature surfaces in order to be captured in a magneto-optical trap [19]. For this reason, dispenser activation and subsequent utilization of the rubidium vapor are often performed in two separate steps.

In this section, we demonstrate a compact technique for the generation of directed atomic beams from an alkali dispenser, which can be useful for miniature applications demanding line-of-sight to the alkali source. For such applications, the broad angular distribution of alkali vapor emitted from a bare dispenser is unacceptable since it can degrade the signal-to-noise ratio as well as contaminate nearby electronic or photonic components. In our approach, laser micromachined holes in a collimator plate deliver atoms primarily in the forward direction. We also find that as the beam is generated, atoms rapidly thermalize with the collimator to a considerably lower temperature, as determined by measurements

21
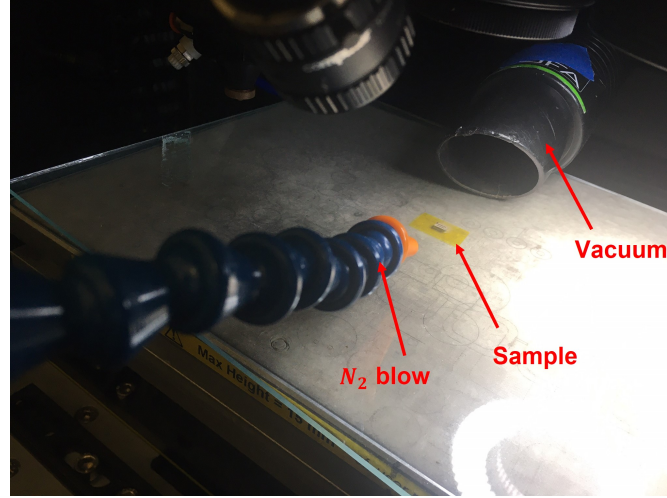
Figure 2.12: Femtosecond laser machining set up. The nozzle on the left side is connected to a N_2 cylinder to blow the vaporized material away from the material and toward the vacuum tube. The sample is fixed on the translational stage by a tape.

of the longitudinal velocity. Combined with its small size, this collimated source can be easily packaged close to other chip-scale components. Our device will find application in the targeted delivery of neutral atoms to microscope volumes on-chip, including on-chip cavities or nanophotonic devices for cavity QED [50, 51]. Our results have been published in Ref [52].

2.3.1 Fabrication

We drilled microchannels in a 600 μm thick stainless steel plate to collimate the emitted rubidium atoms. This collimator plate is fabricated using the femtosecond laser microma-chining technique (OPTEC WS-Flex USP). Femtosecond laser machining uses ultra-short laser pulses with a wavelength of around 1030 nm to ionize and remove the material via photo-ablation. The laser beam waist at focus is around 10 μm, limiting this machine's capability to fabricate smaller-scale structures. The shortest pulse length is around 222 fs and is tunable to 7 ps. With a maximum power of 4 W or the pulse energy of 65 μJ, this laser machining technique is effective on polymers, metals, ceramics, glass, silicon, single crystals, polymorphic crystals, etc. A picture of the setup is shown in Figure 2.12. Since
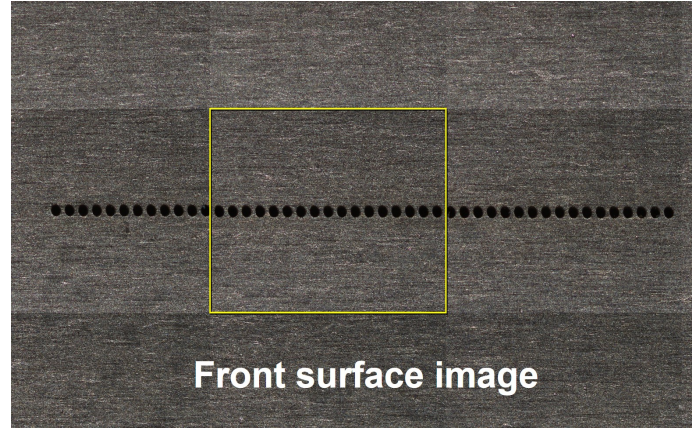
Figure 2.13: The fabricated stainless steel collimator. The diameter of the holes is around 100 μm, and the spacing is 160 μm. The size of the plate is 18 mm $\times$ 12 mm.

the material is vaporized and ionized by the laser pulse, we need to use nitrogen air blow combined with a simple vacuum hose to blow them away. Otherwise, the vaporized material will drop back to the surface and block further processing. For the laser machining settings, the cutting works by defining lines for the laser to pass. To cut a cylindrical microchannel with the stainless steel plate, one cutting layer is achieved by adding circles and hatching lines spaced by 10 μm within them to cut all the material within the circles. One layer is repeated ten times to remove at least 2 μm of the tough stainless steel. Because of the Gaussian beam divergence, the focus of the laser beam cut the fastest and needs to be tuned to cut through the plate. Thus, after finishing a layer, the focus of the laser is moved down 1 μm to move the focus of the laser beam into the material and cut deeper. Furthermore, 300 such layers are created in the software to cut through the 600 μm thick stainless steel plate. As for the diameter of the channels, we tried 50 μm, 100 μm, and 150 μm. The channels with 50 μm diameter, corresponding to an aspect ratio of 12, will provide better collimation. With that high aspect ratio and small diameter, the fabricated dimension of the channels is 72 μm on top and 40 μm on the bottom. However, a portion of the fabricated channels is still opaque (not through holes) because the femtosecond laser beam got blocked by the melted stainless steel. Thus, we choose to test the collimator with a diameter around 100 μm.

The plate we eventually used is shown in Figure 2.13. We cut 46 channels in the center of the plate with a spacing of 160 μm that fully covers the active length of the dispenser (The active length is around 6 mm). The aspect ratio of the channels is around 6:1. As a result of this aspect ratio and the nature of laser micro-machining, the fabricated channels have varying diameters across the plate. As shown in Figure 2.14(b), the entrance diameter is around 115 μm while the exit is an ellipse with $2a \approx 45$ μm and $2b \approx 70$ μm. The plate is positioned with the entrance facing the dispenser to achieve better collimation. The overall device dimensions are around 18 mm$\times$ 12 mm$\times$ 2 mm and could be further reduced. Then, a high-temperature ceramic adhesive (PELCO) is applied between the dispenser and the collimator to hold them together while serving as an insulating spacer. Applying the ceramic adhesive is done in ambient air, and after the adhesive is dried for 20 minutes, the device is put into an oven to cure for 1 hour at 100 °C. This adhesive provides both ultra-low electrical and thermal conductivity so that the current mostly runs through the dispenser and creates a temperature difference between the dispenser and the collimator. The adhesive also seals the space between the dispenser and the collimator to avoid leakage, thereby creating a small cavity that acts as a rubidium reservoir. The off-axis atoms are more likely to return to this reservoir and be saved. Although this procedure requires handling the dispenser in ambient air, we have noticed that the dispensers are not noticeably degraded. The apparatus is shown schematically in Figure 2.14(a).

2.3.2 Transverse velocity distribution

The device was put inside a cubic vacuum chamber that reached a pressure around 4×10^{-7} torr. The two terminals (leads) of the dispenser are connected to a two-pin Conflat electric feedthrough through electrical inline connectors. Then, a high current supply (0-30 A) is used to supply current to the dispenser.

The device was activated by running an 8 A current for around 10 minutes. After activation, the current was lowered to around 6 A, and a relatively steady flux of rubidium
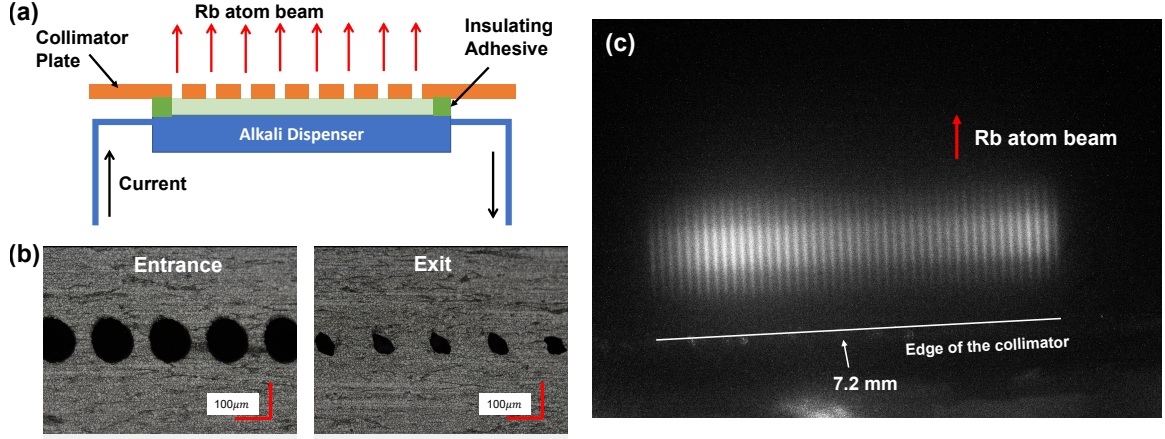
Figure 2.14: (a) Overview of the atomic beam apparatus. The length of the collimator plate is 18 mm, and 46 channels span across 7.2 mm to cover the active length of the dispenser. (b) The detailed view of the entrance and exit channel shape and the length of the scale bar is 100 μm. The entrance faces the dispenser. (c) The CCD camera image of the atomic beams fluorescence. The laser beam enters from the right, and the atomic beams travel toward the top. A white line is added at the position of the collimator edge. It also shows the initial span of the atomic beams ($\sim$7.2 mm).

atoms was produced. The generated miniature atomic beams can be seen in Figure 2.14(c). The operating current is greater than the bare dispenser because of the small exit area ($\sim$0.12 mm^2) and the extra heat load from the collimator plate and ceramic adhesive.

A laser beam was sent perpendicular to the atomic beam direction. Laser spectroscopy at the ^{87}Rb D2 line is used to measure the transverse speed distribution. A current of 6.5 A was run through the dispenser, and the fluorescence was collected by using a 2 inches lens set with a numerical aperture of around 0.24 and a silicon photodetector (Thorlabs Model DET100A2). The photocurrent passes through a current preamplifier (Model 1211 DL Instruments) with a gain of 10^9 V/A. Figure 2.14(c) is the image of the beam fluorescence with our laser locked to the ^{87}Rb D$_2$ $F = 2$ to $F' = 3$ transition. All 46 channels are clearly visible.

The atomic beam fluorescence spectrum is shown in Figure 2.15 (a) together with the saturated absorption spectrum of ^{87}Rb from a reference cell for identification of the spectral lines. The full width at half maximum (FWHM) is 220 MHz. The spectrum is a convolution between the scattering rate R_{sc} and the atoms' transverse Doppler distribution $n(v_t)$. Using
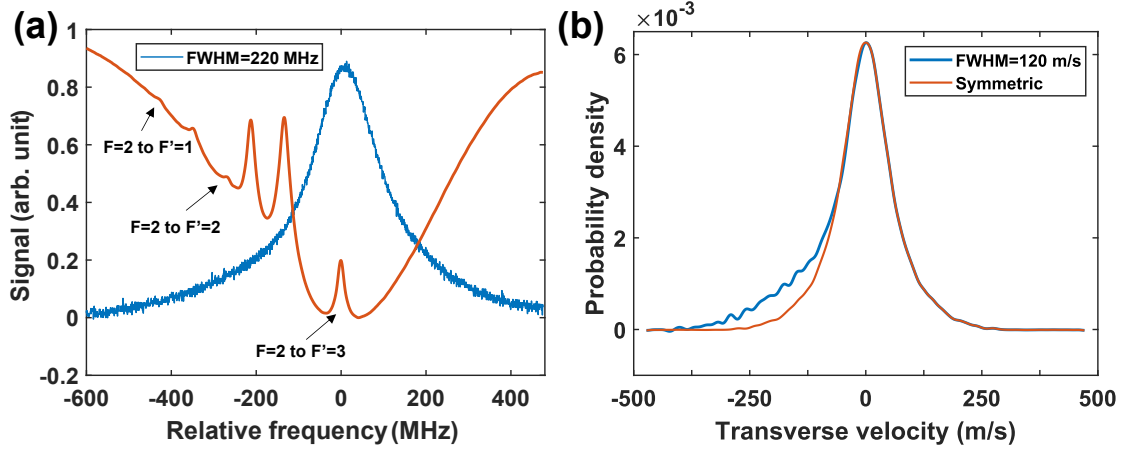
Figure 2.15: (a) Measured fluorescence spectrum (blue) with the ^{87}Rb saturated spectrum (red). (b) The transverse velocity distribution after deconvolution. The red curve is the ideal symmetric shape. The discrepancy around negative 200 m/s results from the influence of F=2 to F'=2, 1 transition.

the deconvolution technique as we have discussed in subsection 2.2.3, and given our laser intensity $I = 2$ mW with beam size $w = 0.586$ mm, we can deduce the transverse speed distribution as shown in Figure 2.15 (b). The FWHM for the transverse speed distribution is around 120 m/s. The deconvolution process here only considered a single $F = 2$ to $F' = 3$ hyperfine level, while the $F = 2$ to $F' = 2, 1$ transitions contribute to the asymmetric shape around -200 m/s [42]. The FWHM here is much bigger than the silicon collimator that was discussed earlier because the aspect ratio d/L is only 1/6 compared with 1/30 with the silicon collimator.

2.3.3 Longitudinal velocity distribution

The next step is to measure the longitudinal speed distribution of the atomic beams. Since the atomic vapor is generated by the chemical reaction under $550 - 850°$C temperature rather than heating rubidium metals to a steady temperature, the velocity distribution of the emitted atomic beams remains an open question. There is a layer of ceramic adhesive with low temperature conductivity between the fabricated stainless steel collimator and the dispenser. Therefore, the collimator is mainly heated by the radiation from the dispenser and
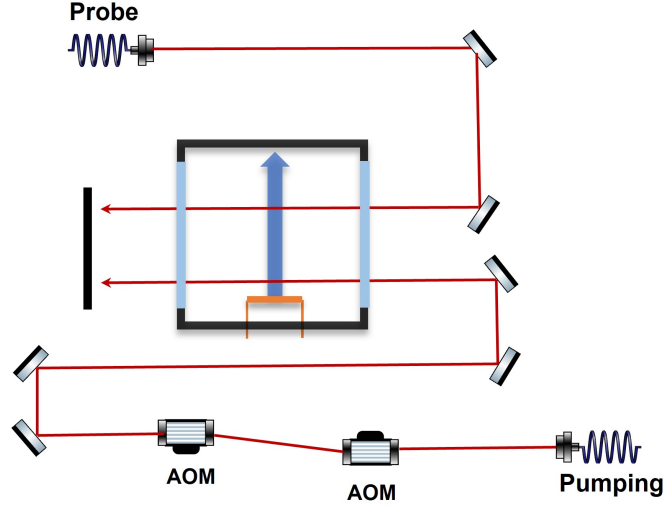
Figure 2.16: The optical diagram of the setup. The probe and pump laser beams are coupled from another optical table. The two AOM are used to create pulses of the pumping beam without creating any frequency shift.

should have a much lower temperature. The emitted fast atoms from the chemical reaction are expected to collide with the wall of the collimator, which will make the emitted atoms thermalize with our stainless steel collimator and have a much lower average velocity. One common way to measure the longitudinal velocity distribution is by sending the probe at an angle (e.g. 45°) relative to the atomic beam direction and measuring the longitudinal Doppler shift spectrally. This method works well with highly collimated atomic beams with a large mean velocity but has many sources of error for a moderately collimated beam or atoms with slow velocity. First, this method can be easily affected by the transverse velocity distribution. If the transverse velocity is not negligible, it is hard to find a well-defined atomic beam direction, and the Doppler effect observed will be contributed by both the longitudinal and transverse velocities. Then, the power broadening and the contributions from other hyperfine transitions will also cause errors in the calculation of velocity distribution with this method.

We measured the longitudinal velocity distribution by using a modified time of flight technique [53]. In our time-of-flight technique, a locked pumping laser is tuned to the ^{87}Rb D$_2$ $F = 2$ to $F' = 2$ transition that selects atoms with nearly zero transverse velocity,

pumping them into the dark hyperfine ground state $F = 1$. The optical diagram is shown in Figure 2.16. The pump laser is first sent into an acoustic-optical modulator (AOM), and its frequency is increased by 80 MHz. Then a second acoustic-optical modulator is used to decrease the pump laser frequency by 80 MHz. Therefore, the pump frequency remains unchanged, but we can create pulses of the pump beam by turning the AOM on and off. A function generator is used to create a 1 kHz TTL signal to control the on and off of the AOM while providing the trigger signal for our oscilloscope. The pump laser is placed very close to the stainless steel collimator to pump all the atoms before they diverge, as shown in Figure 2.17(a) inset. A probe beam locked to the ^{87}Rb D$_2$ $F = 2$ to $F' = 3$ transition is located downstream from the pump to detect the atoms with nearly zero transverse velocity. The fluorescence from the probe beam is collected by a micro-photomultiplier tube (Hamamatsu H12403-20), and the output current from the micro-photomultiplier is amplified by a current amplifier (DLPCA-200) with a gain of 10^5 V/A. The rise time for the current amplifier at this gain is around 900 ns.

The separation between our pump and probe laser beams is $L = 20$ mm, while the diameters of both beams are $d_1 = d_2 = 1.2$ mm. The dispenser current was increased to 7 A to increase the signal-to-noise ratio. In this configuration, the atoms we pumped and probed are the atoms with near-zero transverse velocities. Thus the longitudinal velocity measurement is not affected by the transverse component. The power broadening and other hyperfine transitions also won't affect our signal. Therefore we can measure the longitudinal velocity accurately, especially with the slow atoms ($v < 100$ m/s). While the pump beam is on, all atoms, with around zero transverse velocity, enter the dark state, and the probe fluorescence will be zero. By switching off the pump, atoms in the bright state $F = 2$ will enter the probe region with a time of arrival that depends on their velocity. Thus following the switch-off, the detector records a time-dependent fluorescence signal $S(t)$ that starts from zero and gradually reaches a steady state. Figure 2.17(a) shows the data after averaging over 64 traces with our oscilloscope (TDS2024C). The fluorescence
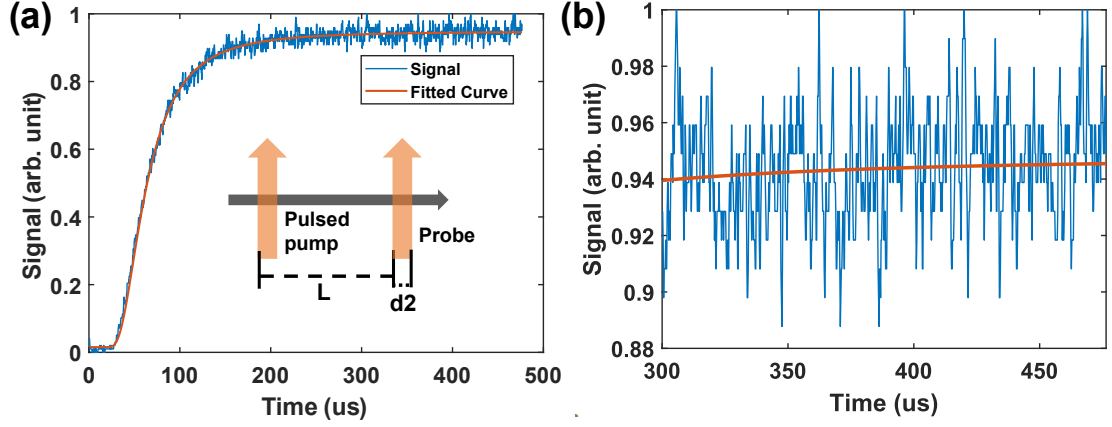
Figure 2.17: (a) The recover signal of the time of flight measurement. Time zero is when the pump laser pulse is switched off. The fitted curve assumes a Maxwell distribution with $u = 302$ m/s. The inset is the diagram for the time of flight setup. (b) Zoomed-in plot for the signal of slow atoms between 44.5 m/s and 70m/s. The red line is the theoretical curve.

signal in the steady state will depend on the density of atoms in the probe region. Assuming a Maxwell Boltzmann longitudinal speed distribution [54], we can write our signal as:

$$
S(v,t) = \begin{cases} 0 & vt \leq L \\ c \cdot v^2 e^{-\frac{v^2}{u^2}} \cdot (vt - L) & L \leq vt \leq L + d_2 \\ c \cdot v^2 e^{-\frac{-v^2}{u^2}} \cdot d_2 & vt \geq L + d_2 \end{cases} \tag{2.11}
$$

In which L is the distance between the pump beam and the probe beam, d_2 is the diameter of the probe beam, c is the amplitude factor that does not depend on v, and $u = \sqrt{2kT/m}$ is the most probable speed. Then, our total signal at time t, including all velocity groups, is:

$$
\begin{aligned}
S(t) &= \int_{L/t}^{\infty} S(v,t)dv \\
&= c\left(\int_{\frac{L}{t}}^{L+d_2/t} v^2 e^{\frac{-v^2}{u^2}} \cdot (vt - L)dv + \int_{\frac{L+d_2}{t}}^{\infty} v^2 e^{\frac{-v^2}{u^2}} \cdot d_2 dv \right)
\end{aligned} \tag{2.12}
$$

This formula is fitted to our signal by minimizing the squared error, as shown in Figure 2.17,

yielding a peak velocity of $u = 302$ m/s, corresponding to a Maxwell distribution with a temperature of around 204 °C. This temperature is significantly lower than the expected operating temperature of the dispenser ($> 600°$C), indicating that the atoms thermalize with the colder surfaces of the collimator plate before exiting the device. Thus it produces slower atoms on average compared with the bare dispenser.

These findings demonstrated that the temperature of the emitted atoms from our device is much lower than the dispenser, which suggests that direct line-of-sight laser cooling might be possible using this integrated dispenser collimator, thus avoiding contamination of the vacuum chamber or miniature cell.

To further quantify the slow atoms, we can calculate the difference of $S(t)$ at time t_1 and t_2:

$$S(t_1) - S(t_2) =$$
$$c \int_{\frac{L}{t_1}}^{\frac{L+d_2}{t_1}} v^2 e^{-\frac{v^2}{u^2}}(vt_1 - L)dv - c \int_{\frac{L}{t_2}}^{\frac{L+d_2}{t_2}} v^2 e^{-\frac{v^2}{u^2}}(vt_2 - L)dv + c \int_{\frac{L+d_2}{t_1}}^{\frac{L+d_2}{t_1}} v^2 e^{-\frac{v^2}{u^2}}d_2dv$$

$$(2.13)$$

By setting $v_i = \frac{L+d_2}{t_i}$ for $i = 1, 2$, and using $d_2 << L$, we get:

$$S(t_1) - S(t_2) \approx c \cdot v_1^2 e^{-\frac{v_1^2}{u^2}} d_2 \cdot \frac{d_2}{t_1} - c \cdot v_2^2 e^{-\frac{v_2^2}{u^2}} d_2 \cdot \frac{d_2}{t_2} + c \int_{v_1}^{v_2} t_1 v^2 e^{-\frac{v^2}{u^2}} d_2dv \quad (2.14)$$

The first two terms are proportional to d_2^2 and are ignored with $d_2 << L$, we have

$$S(t_1) - S(t_2) \propto \int_{v_1}^{v_2} v^2 e^{-\frac{v^2}{u^2}} dv \quad (2.15)$$

This means that the difference of $S(t)$ between time t_1 and t_2 is proportional to the density of atoms between velocity v_1 and v_2. Figure 2.17 (b) shows the zoomed-in plot between $t_1 = 476$ $\mu s, t_2 = 303$ μs which corresponding to $v_1 = 44.5$ m/s and $v_2 = 70$ m/s. By using the fitted $S(t)$ and normalization $S(\infty) - S(0) = 1$, the atom density within

$v_1 = 44.5$ m/s and $v_2 = 70$ m/s is calculated to be 0.61% of the entire atom density. By comparison, the theoretical ratio for a Maxwell distribution is 0.67%, which is very close to our measured value. Since in Figure 2.17 (b), the amplitude of the noise is much higher than the change of the signal, one might argue that the contributions from slow atoms need more supportive evidence. To further confirm these observations, we implemented the likelihood ratio test between the null hypothesis and the alternative hypothesis. The null hypothesis is that there are no slow atoms in that velocity range. Thus $S(t)$ should be flat, and the observed signal is just Gaussian noise. The alternative hypothesis is that the theoretical equation (Equation 2.12) is valid for slow atoms and the observed signal is $S(t)$ plus Gaussian noise. We can calculate the likelihood of each scenario happening with its hypothesis. The likelihood ratio p_r of the alternative hypothesis to the null hypothesis is calculated to be 1.1×10^4. Thus the signal shows strong evidence for the existence of slow atoms in a thermal beam. These slow atoms are easier to control and can be captured by a MOT downstream or might be used directly for on-chip applications.

Here, we can also notice that the signal-to-noise ratio is limited even with a well-designed time-of-flight technique and detection with a micro-photomultiplier tube combined with a current amplifier. It is still very challenging to unambiguously detect the slow atoms with velocity $v < 45$ m/s in a thermal beam. In Chapter 4, we will show how to directly detect these slow atoms by implementing a novel technique based on single photon correlations,

2.3.4 Long-term performance

The long-term performance of this device was characterized by monitoring the flux at variable supply currents. A PC oscilloscope Picoscope (5242D) is used for this test. The PC oscilloscope needs to connect with a laptop but provides more functionalities compared with a benchtop oscilloscope. The probe laser was scanned over several GHz around ^{87}Rb D_2 line F=2 to F'=3 transition. An alarm function is implemented to save both the signal
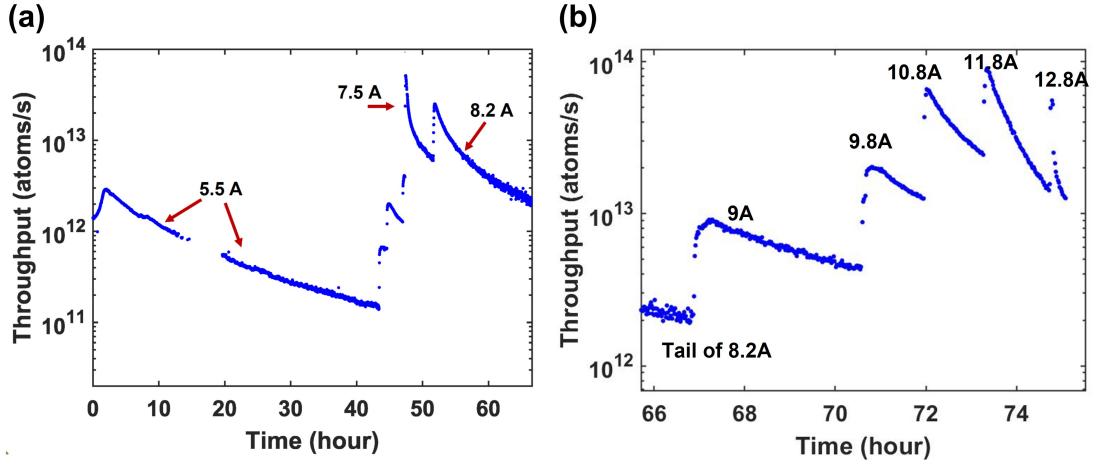
Figure 2.18: Throughput vs time curves of the integrated dispenser collimator. (a) Current was run through the dispenser in intervals of ~0.5 A ranging from 5.5 A to 8.2 A. Curves with a current of 5.5 A, 7.5 A, and 8.2 A are labeled. Overnight, the laser scan region drifted out of the ^{87}Rb D$_2$ F=2 to F'=3 transition and caused a gap in the 5.5 A data. (b) Currents higher than 8.2 A. The currents are increased to an extremely high range to accelerate the process while serving as a current limit test for our device.

data and the saturated spectrum data to the laptop every minute.

The initial current was 5.5 A, and it was increased in steps of ~0.5 A to 8.2 A. The total throughput of the device is calculated by using the methods and procedures mentioned in subsection 2.2.3 and Ref. [42]. The calculated throughput value at different currents and times is shown in Figure 2.18. With an elevated current through the dispenser, the flux first rapidly increased and then slowly decreased on a time scale of hours. This behavior is typical for alkali dispensers, according to its spec sheet [46]. A feedback loop may be integrated into the system in the future to produce a constant flux. After 8.2 A, the input current to the dispenser was gradually increased to 12.8 A to test when the device would fail. After around 20 minutes at 12.8 A, the collimator plate detached because of the thermal expansion mismatch between the ceramic adhesive and metal surfaces. This indicates the current limit of this device should be around 12 A.

The total test lasted around 75 hours. By integrating the area under the curves, we calculated that the rubidium emitted during this test was around 0.18 mg. The device was run for around 12 hours at 6.5 A before this long-term performance test. As a comparison, a

bare rubidium dispenser will be empty in around 4 hours at 7 A [19]. Our device lifetime is greatly increased due to the collimator, which blocks and saves the off-axis atoms while maintaining the on-axis flux. For applications that only need to operate the atomic beam as necessary, such as MOT capturing and trapping, this device can last much longer. Applications requiring higher collimation can use a stainless steel collimator with a higher aspect ratio which would provide an even longer lifetime.

2.3.5   Summary

Our observations indicate that the hot atoms from the dispenser rapidly thermalize with the collimator plate with a transit distance of only around 600 μm (the thickness of the collimator plate). As a result, the temperature of the atoms is lowered by a factor of 3 compared with the bare dispenser. To explore this effect further, we replaced the stainless steel collimator plate with the silicon collimator from our previous work (section 2.2) and built a conventional dispenser oven in a stainless steel tube of 3/4 inch diameter. The temperature of the collimator is monitored and fixed to around 110 $^\circ$ (for more details, see our publication [52]). The data with this conventional design also demonstrate the hot atoms from the dispenser thermalize with the collimator wall and oven wall first before coming out, which supports our theory.

In summary, We have demonstrated a versatile and compact approach to creating atomic beams using a collimator-integrated dispenser. In our design, the collimation plate is integrated onto the dispenser itself, which serves the dual purpose of shielding the environment from the high dispenser operation temperature as well as reducing the effective temperature of the atomic beam. Our results show that atomic beam technology can be considerably miniaturized without compromising its useful properties, which will extend its applications to small-scale quantum devices. For example, even further integration could be achieved by incorporating dispenser material directly into the collimation plate.

CHAPTER 3

CAVITY QED ON CHIP WITH ATOMIC BEAMS AND MICRORESONATORS

3.1 Introduction

Numerous applications in quantum optics, communications, and computing rely on strong interactions between single atoms and photons [3, 55, 56, 57]. Atoms can be used as nodes in a quantum network to create, process, and store quantum information. Photons can be used as channels to transfer information and link different nodes together [58, 59]. An efficient and scalable platform for strong atom-photon interaction is thus a long-standing goal of both fundamental and technological significance.

To efficiently create entanglement between single atoms and single photons, the interaction strength between them must be strong enough. Although we could easily use a laser beam to excite the atoms to measure the spectrum, the probability of a single atom interacting with a single photon is very small. The maximum possible resonant cross-section σ_{sc} between photons and a two-level atom in free space is $3\lambda^2/2\pi$ [43]. The probability P for a photon to be absorbed is σ_{sc}/A_{eff}, where A_{eff} is the area of the laser beam [56]. For example, if the laser beam has a diameter of 1 mm, the probability is only around $3.7 \cdot 10^{-6}$. Even with a diffraction-limited focusing spot with NA=0.5 and $A_{eff} \approx \lambda^2$, the maximum interaction probability is only around 15%, which is not ideal for single-photon single-atom interaction. Cavity Quantum Electrodynamics (Cavity QED) is usually utilized to increase the probability of entanglement between them. A single photon can experience many round-trips inside a cavity, and the interaction strength is thus enhanced. The enhanced probability $\sigma_{sc}N_{trips}/A_{eff}$ is proportional to the figure of merit— single atom cooperativity C, which will be discussed later. Macroscopic cavities in free space (Fabry-Perot cavities) have shown great success in achieving strong interaction with the

atoms [60, 61, 62]. In recent years, there has been lots of effort to utilize microtoroidal cavities [63, 64], nanofibers [65, 66], nanophotonic structures [67, 68, 51], and microring resonators [69, 50] to create micro-platforms for strong atom-photon interaction. Several motivations are the driving force. First, by using modern micro-fabrication techniques, the new platforms can be more scalable and robust, showing a promising approach to chip-scale quantum devices. Second, the single-atom cooperativity C is the figure of merit for single-photon and single-atom interaction. It is inversely proportional to the mode volume. In these micro-structures, the light is tightly confined, and the mode volume is extremely small, leading to a larger cooperativity value.

Most of the demonstrated results use free-fall cold atom [70] or trapped cold atoms [67]. It requires substantial effort to cool, transport, and trap the atoms near the dielectric surface of the nanophotonic system. Miniaturization and scalability are hindered by these additional requirements. Moreover, there is a mismatch of timescales between the nanoseconds required to strongly couple atoms and photons in microresonators and the milliseconds to seconds required for atomic cooling and trap loading. This limits the duty cycle of quantum devices based on atoms and photons.

In contrast, laser-slowed or even fast thermal atomic beams possess many of the prerequisites for quantum device fabrication [38]. In the previous chapter, we demonstrated our highly collimated chip-scale atomic beams with silicon lithography. These atomic beams can be easily generated and continuously operated. We have also shown its robustness and reliability on six months scale. Since it is feasible to integrate the atomic channels and microresonators on the same silicon wafer, the micrometer level alignment is naturally satisfied. This chapter will focus on our efforts in trying to combine chip-scale atomic beams with Si_3N_4 micro-resonators to create a novel and scalable platform for strong interactions between single atoms and single photons.

3.2 Theoretical background

The coupling between an atom and an optical mode is governed by the Jaynes–Cummings Hamiltonian [3, 43]:

$$H = H_A + H_F + H_{AF} = \hbar\omega_a\sigma^\dagger\sigma + \hbar\omega(a^\dagger a + \frac{1}{2}) - \vec{d}\cdot\vec{E} \tag{3.1}$$

In which $\sigma = |g\rangle\langle e|$ is the atomic lowering operator; a is the photon annihilation operator; ω_a and ω are the atomic and cavity angular resonance frequencies, respectively. The last term is the dipole form of the atom-field interaction Hamiltonian H_{AF}. We have

$$\vec{d} = \vec{d}_{ge}(\sigma + \sigma^\dagger) \tag{3.2}$$

Here, $\vec{d}_{ge}$ is the dipole matrix element for the atomic transition between the ground state and the excited state. The electric field can be written as [71, 43]:

$$\vec{E}(\vec{r}, t) = -\sqrt{\frac{\hbar w}{2\epsilon_r\epsilon_0}}[f(\vec{r})a(t) + f^*(\vec{r})a(t)^\dagger] \tag{3.3}$$

Where ϵ_r, ϵ_0 are the relative permittivity and vacuum permittivity and ϵ_r also have a spatial dependence in our system, $f(\vec{r})$ is the normalized cavity mode function defined by

$$f(\vec{r}) = \frac{\sqrt{\epsilon_r}E(\vec{r})}{\sqrt{\int d^3r \cdot \epsilon_r |E(\vec{r})|^2}} \tag{3.4}$$

We can choose the phase to make $f(\vec{r})$ real and positive [43]. Then combine $\vec{d}$ and $\vec{E}(\vec{r}, t)$, we get:

$$H_{AF} = -\vec{d}\cdot\vec{E} = -\sqrt{\frac{\hbar w}{2\epsilon_r\epsilon_0}}\vec{d}_{ge}\cdot f(\vec{r})(\sigma + \sigma^\dagger)(a + a^\dagger) \tag{3.5}$$

We define the atom-cavity field coupling energy

$$\hbar g(\vec{r}) = -\sqrt{\frac{\hbar w}{2\epsilon_r \epsilon_0}} \vec{d}_{ge} \cdot f(\vec{r}) \qquad (3.6)$$

The $g(\vec{r})$ factor characterizes the interaction strength between the atom and the cavity mode and $2g(\vec{r})$ is called the single photon Rabi frequency (the reason will be explained later). To better understand and calculate this factor, we define the mode volume V of the cavity as

$$V = \int dr^3 \frac{\epsilon_r |E(\vec{r})|^2}{\max(\epsilon_r |E(\vec{r})|^2)} \qquad (3.7)$$

Combined V with the definition of $f(\vec{r})$, we can get

$$f(\vec{r}) = \frac{1}{\sqrt{V}} \cdot \frac{\sqrt{\epsilon_r} E(\vec{r})}{\max(\sqrt{\epsilon_r}|E(\vec{r})|)} \qquad (3.8)$$

$$g(\vec{r}) = -\sqrt{\frac{w}{2\hbar\epsilon_r\epsilon_0}} \vec{d}_{ge} \cdot f(\vec{r}) = g_0 \cdot \frac{\sqrt{\epsilon_r}|E(\vec{r})|}{\cdot \max(\sqrt{\epsilon_r}|E(\vec{r})|)} \qquad (3.9)$$

Where $g_0 = -\vec{d}_{ge} \cdot \hat{\xi} \sqrt{\frac{w}{2\hbar\epsilon_r\epsilon_0 V}}$ is the maximum possible value of $g(\vec{r})$. $\hat{\xi}$ is the unit polarization vector of the field mode at the location of the atom. This formula will be used to calculate the interaction strength in different locations in our atomic beam-resonator system.

Thus, H_{AF} becomes

$$H_{AF} = \hbar g(\vec{r})(\sigma + \sigma^\dagger)(a + a^\dagger) \qquad (3.10)$$

Then, we move into the interaction picture and make the rotating-wave approximation to drop the fast oscillating terms [43]. We get

$$H_{AF} = \hbar g(\vec{r})(\sigma a^\dagger + \sigma^\dagger a) \qquad (3.11)$$

The total Hamiltonian after dropping the vacuum-field energy constant $\frac{1}{2}\hbar\omega$ is

$$H = \hbar\omega_a\sigma^\dagger\sigma + \hbar\omega a^\dagger a + \hbar g(\vec{r})(\sigma a^\dagger + \sigma^\dagger a) \tag{3.12}$$

This is the well-known Jaynes-Cumming Hamiltonian.

To solve the dynamics of Jaynes-Cumming Hamiltonian, we decompose the state in terms of the joint eigenstates of H_A and H_F:

$$|\psi\rangle = \sum_{n=0}^{\infty}(c_{g,n}|g,n\rangle + c_{e,n}|e,n\rangle) \tag{3.13}$$

Here, g, e represents the atom in the ground state or excited state, respectively, and n means the Fock state with n photons. By using Schrodinger's equation, we can get the pairs of equations for all values of n:

$$\partial_t c_{e,n} = -i(\omega_a + n\omega)c_{e,n} - i\sqrt{n+1}g(\vec{r})c_{g,n+1}$$
$$\partial_t c_{g,n+1} = -i(n+1)\omega c_{g,n+1} - i\sqrt{n+1}g(\vec{r})c_{e,n} \tag{3.14}$$

By considering the resonance case, which means $\Delta = w_a - w = 0$, and assuming the system is initially in state $|g, n+1\rangle$, we can solve the equations to get the population [43]:

$$P_{e,n} = \frac{1}{2}(1 - \cos(2\sqrt{n+1}g(\vec{r})t))$$
$$P_{g,n+1} = \frac{1}{2}(1 + \cos(2\sqrt{n+1}g(\vec{r})t)) \tag{3.15}$$

Thus, when we have n+1 photons in the cavity, the Rabi frequency is $2\sqrt{n+1}g(\vec{r})$. For a single photon in the cavity, we have n=0, and $2g(\vec{r})$ is the single photon Rabi frequency. We can also see that the energy exchange rate between the atom and the cavity is proportional to $g(\vec{r})$.

By diagonalizing the 2 ×2 matrix in Equation 3.14, we can get the eigenenergies and
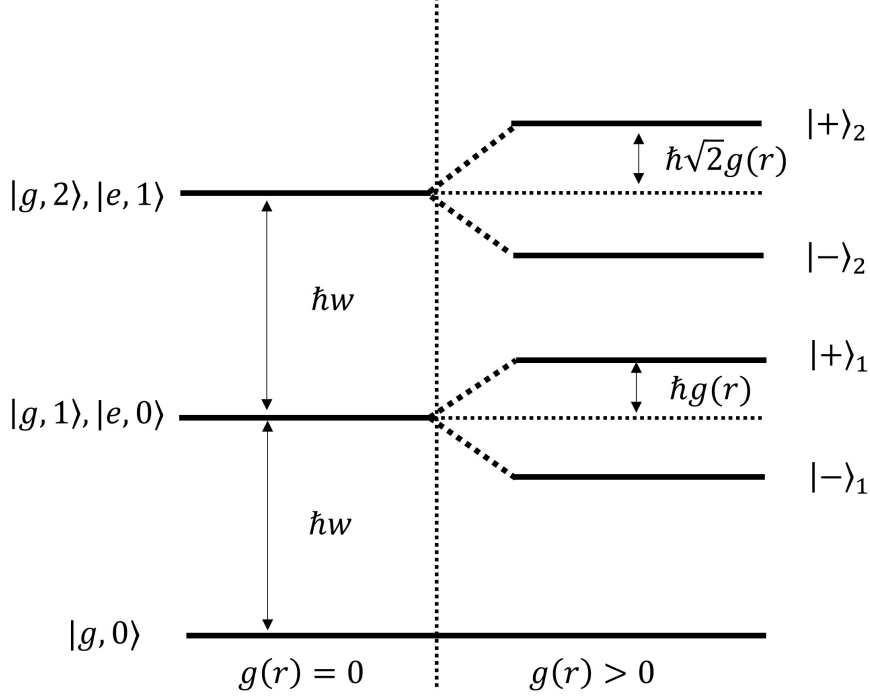
Figure 3.1: The eigenvalue diagram for the Jaynes-Cummings Hamiltonian. The left side is without any atom-cavity coupling $g(r) = 0$, and the right side is after introducing the interaction term $g(r) > 0$. The splitting is proportional to $g(r)$ and the number of photons.

eigenstates of the dressed state picture

$$
\begin{aligned}
E_{n,\pm} &= n\hbar\omega \pm \sqrt{n}\hbar g(\vec{r}) \\
|\pm\rangle_n &= \frac{1}{\sqrt{2}}(|e, n-1\rangle \pm |g, n\rangle)
\end{aligned}
\tag{3.16}
$$

The diagram of energy levels is shown in Figure 3.1. The splitting with a single photon equals $2\hbar g(\vec{r})$, which is also called vacuum-Rabi splitting.

To understand the dynamics of an atom interacting with the resonator, we need to add the outside world into the system, which includes the coupling of input light, the cavity dissipation mechanisms, and the atomic dissipation.

First, some basics of the cavity will be discussed. The cavity lifetime τ_c is defined to be the time the energy stored in a cavity decays to $1/e$ of its value. Thus, the cavity energy decay rate is $\kappa = 1/\tau_c$, and some papers use the same symbol κ for 'field decay rate,' which is just half of the energy decay rate defined here. The quality factor Q of the cavity is defined

as 2π times the cavity lifetime in terms of the number of optical cycles

$$Q = 2\pi \cdot \tau_c / \tau_p = \frac{\omega}{\kappa} \tag{3.17}$$

Here, τ_p is the inverse of optical frequency, and ω is the angular frequency of the cavity mode. On the other hand, the finesse F of a cavity is defined as 2π times the cavity lifetime in terms of the number of round trips

$$F = 2\pi \cdot \tau_c / \tau_t = \frac{2\pi}{\kappa n \cdot L/c} = \frac{Q\lambda}{n \cdot L} \tag{3.18}$$

Where L is the round trip distance in the cavity, $\tau_t = n \cdot L/c$ is the round trip time, n is the refractive index, and λ is the wavelength of the cavity mode. We can notice that finesse depends on the cavity length and refractive index, which is less convenient for comparing nanophotonic resonators. Thus, the finesse F is usually used in free-space cavities like Fabry-Perot cavities, while the quality factor Q is frequently used in micro-resonators fabricated with nanophotonic techniques.

For nanophotonic resonators (e.g., micro-ring, micro-disk, and micro-toroid resonators), waveguides or tapered fibers are used to couple light in and out of the resonator. There will be a coupling quality factor Q_{couple} besides the intrinsic quality factor $Q_{intrinsic}$. $Q_{intrinsic}$ depends on the resonator's propagation loss, as we have discussed. Q_{couple} is the inverse of the energy coupling rate between the waveguide (or fiber) and the resonator, which can be tuned by the distance between them. When $Q_{couple} = Q_{intrinsic}$, destructive interference makes the transmitted field vanish, and all the input light is coupled into the resonator [72, 73]. It is named the critical coupling condition, and the total quality factor Q becomes

$$\frac{1}{Q} = \frac{1}{Q_{couple}} + \frac{1}{Q_{intrinsic}} = \frac{2}{Q_{intrinsic}} \tag{3.19}$$

If the coupling is weaker, $Q_{couple} > Q_{intrinsic}$, the resonator is under-coupled. If the

coupling is stronger, $Q_{couple} < Q_{intrinsic}$, the resonator is over-coupled. In the scope of this thesis, we focus on critically coupled resonators. The quality factor and the cavity energy decay rate we refer to will be the total quality factor and total cavity decay rate ($\kappa = \kappa_{intrinsic} + \kappa_{coupling}$).

The next step is to include the input laser. We can add an extra term in the Hamiltonian in Equation 3.12, the Hamiltonian with the external laser driving term in a rotating frame becomes [43]:

$$H = \hbar(\omega_a - \omega_L)\sigma^\dagger\sigma + \hbar(\omega - \omega_L)a^\dagger a + \hbar g(\vec{r})(\sigma a^\dagger + \sigma^\dagger a) + \hbar\xi(a + a^\dagger) \tag{3.20}$$

Where ω_L is the input laser frequency and $\xi = \sqrt{\kappa P/\hbar\omega_L}/2$ under the critical coupling condition, κ is the total cavity energy decay rate, and P is the power of the input laser. This extra term deposits energy into the system over time.

In order to introduce the cavity decay and the atom's spontaneous decay, we use the density matrix ρ and introduce the environmental reservoirs to the system. The Master equation for the density operator is [3, 43]:

$$\partial_t\rho = -\frac{i}{\hbar}[H, \rho] + \Gamma D[\sigma]\rho + \kappa D[a]\rho \tag{3.21}$$

The Lindblad superoperator $D[c]\rho$ is given by $D[c]\rho = c\rho c^\dagger - 1/2(c^\dagger c\rho + \rho c^\dagger c)$ for $c = \sigma, a$. The second term corresponds to the atomic decay, and Γ is the spontaneous emission rate. The third term corresponds to cavity decay, and κ is the total cavity energy decay rate. Figure 3.2 shows the calculated cavity transmission by solving Equation 3.21 with a fixed atom and without an atom ($g = 0$). The input laser has a power of 7.56 pW, and its frequency is scanned over 1 GHz. The total quality factor is set to be 10 million and $g/2\pi = 250$ MHz. The transmission spectrum agrees with the dressed state picture (Figure 3.1). With $g > 0$, a single resonance peak is split into two peaks separated by $2g$, which demonstrates the vacuum-Rabi splitting.
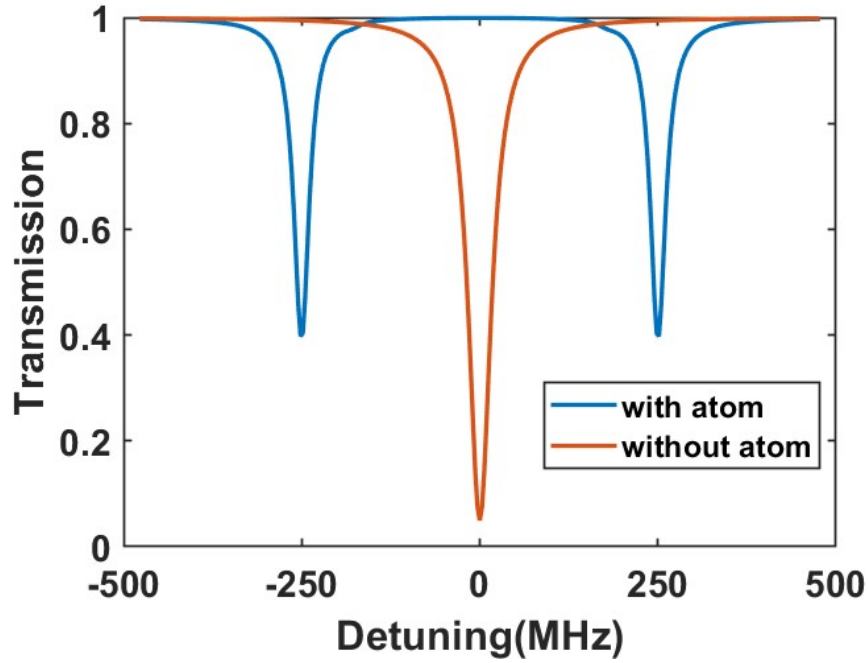
Figure 3.2: The calculated transmission spectrum of a micro-ring resonator with and without an atom. The total quality factor is 10 million. The input laser power is 7.56 pW, and $g/2\pi = 250$ MHz. With an atom, the single resonance peak is split into two, and the splitting separation is $2g$.

Finally, the figure of the merit for cavity QED is the single atom cooperativity C. It is a dimensionless value defined as

$$C = \frac{2g^2}{\kappa\Gamma} \tag{3.22}$$

The single atom cooperativity is the square of g factor divided by the product of two dissipation rates, which indicates the ratio between the coherent and incoherent effects in a coupled system. The inverse of C is also often referred to be the critical atom number, which gives the number of atoms required to strongly change the cavity transmission. To achieve a strong interaction between a single atom and a single photon, we need $C > 1$. In this case, even a single atom is able to induce a large effect on cavity transmission. If $g \gg (\kappa, \Gamma)$, the coherent process happens faster than any dissipation mechanism, then the system is in the 'strong coupling' regime.

By using the definition of g (Equation 3.9) in C (Equation 3.22) and combining the defini-

tion of quality factor Q (Equation 3.17), we find that

$$C \propto \frac{Q}{V} \left| \frac{\epsilon_r E(\vec{r})}{\max(\epsilon_r E(\vec{r}))} \right|^2 \tag{3.23}$$

We can see that, to achieve large cooperativity, we need to maximize Q/V and direct the atoms toward the maximum electric field. The small mode volume is one of the biggest advantages of nanophotonic resonators.

3.3 Micro-ring resonator

In this section, we will experimentally demonstrate a high-performance silicon nitride (Si_3N_4 or, in short, SiN) microring resonator and show, through simulations, that it is capable of strongly interacting with slow atomic beams during their microseconds-long transit time above the resonator. We also show that racetrack versions of these resonators can be combined with thermal atomic beams, which substantially reduces the vacuum requirement and laser overhead and paves the way toward highly integrated quantum devices using atoms on chips. The results in this section have been published in Ref. [50].

The proposed integrated platform is shown in Figure 3.3. We can integrate the silicon channels we described in Chapter 2 with the nanofabricated microresonators on the same chip. Rubidium atoms from an atomic source, either a slow atomic beam from a 2D+ magneto-optical trap (MOT) or a beam of fast atoms from a thermal vapor, pass through the microchannels, fly above the resonator, and strongly interact with it through the evanescent field. Lithographically defined microchannels of several mm in length help with atomic beam collimation and alignment with the resonator. The alignment between atoms and the resonator is a huge issue for many other platforms [67, 63]. The alignment is crucial for the interaction since the mode volume for these microresonators is extremely small. Our precisely controlled channel size and location will align the atoms and the resonator naturally on the same chip, offering a huge advantage in scalability and robustness. As we discussed in Chapter 2, the microchannels can be freely tailored for different applications, and great collimation can be achieved to minimize excess contamination by the atoms to the resonator.

3.3.1 Fabrication and characterization

The high-quality factor (high-Q) micro-ring resonator is fabricated by Ali Dorche in Prof. Ali Adibi's group at Georgia Tech and characterized by Ali Dorche and myself. More
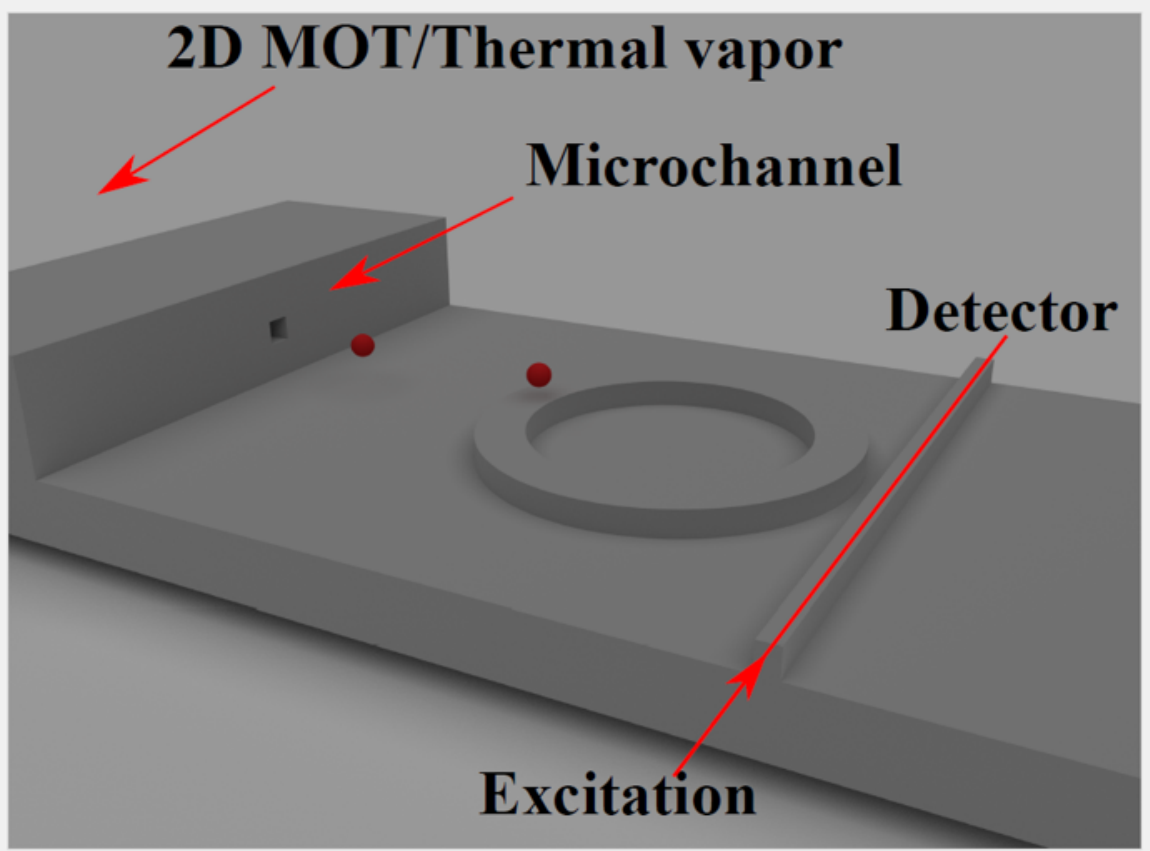
Figure 3.3: Schematic of the proposed integrated platform for cavity QED. The microchannels for atoms and the micro-resonators are integrated on the same chip. Collimated atomic beams fly above the resonator and interact with it via the evanescent field from the resonator. The resonator is coupled with a waveguide to guide photons in and out.

details about fabrication can be found in our publication [50].

In our platform, the microresonator should allow a strong interaction of the atom flying above the resonator with the evanescent tail of the electric field of a resonant mode. This requires a thin SiN film with air-clad. Furthermore, the microresonator needs to have a reasonably small radius for the single atom cooperativity parameter $C \propto Q/V$ increases with decreasing mode volume V. The requirements for efficient atom-photon interactions impose trade-offs among the degrees of freedom to achieve high Qs in microresonators. High-Q microresonators are usually achieved with a large radius, tight field confinement, and oxide-clad. Our requirements, along with the increased Rayleigh scattering at typical wavelengths of atomic transition [74], highlight the challenges to achieve high-Q [75]. Our

deposited SiN layer has a measured thickness of 287 nm. The width of the waveguide bent to form the microring resonator is chosen $w_f = 5$ μm to minimize the effect of the surface roughness at the inner wall of the microresonator. Another reason for choosing a larger width and radius than Ref [69] is because atomic beams are faster with a larger spatial distribution than trapped atoms. A bigger resonator increases the overlap with flying atoms as well as their interaction time. The outer radius of the ring is $R_o = 35$ μm to ensure an appropriate quality of the resonant modes, i.e., avoiding significant curvature while increasing the coupling factor g, and having a large-enough spectral distance between different families of transverse resonant modes. The second-order radial TE mode has a higher Q than the first-order one as its electric field peak is farther away from the outer ring sidewall, thus lowering the scattering losses. The bus waveguide coupled to the microring resonator has a width of 770 nm at the coupling region to ensure appropriate coupling.

The fabrication process starts with a planar polished oxidized silicon (Si) wafer, with 5 μm thermal oxide that is formed by dry-wet-dry oxidation process, forming a 300 nm-thick dry silicon dioxide (SiO_2) layer on top to ensure the high quality of the oxide region at the interface with the devices. The SiN layer for defining the waveguide and microresonator is deposited by LPCVD at a Tystar nitride furnace, with agent gases of dichlorosilane (DCS) and ammonia at $800°C$. The stoichiometric SiN (i.e., Si$_3$N$_4$) is deposited by adjusting the agents' ratio, leading to a refractive index around 2 at $\lambda = 632$ nm. The deposition time is adjusted to reach a SiN thickness of about 290 nm (the actual measured thickness on the sample has been 287 nm). The sample is cleaned in two steps: first AMI solution (acetone, methanol, isopropanol), nitrogen blow dry, followed by a short BOE 6:1 (buffered oxide etchant) wet etching, running DI (deionized) water, and nitrogen blow dry. The sample is then baked on a hot plate to remove any moisture and prepare it for electron-beam resist coating. Flowable oxide (DOW corning FOx 16) is then spun on the SiN thin film, followed by baking the sample on a hot plate. The devices are patterned using electron beam lithography (EBL) with current $I = 2$ nA. The EBL parameters are optimized to minimize
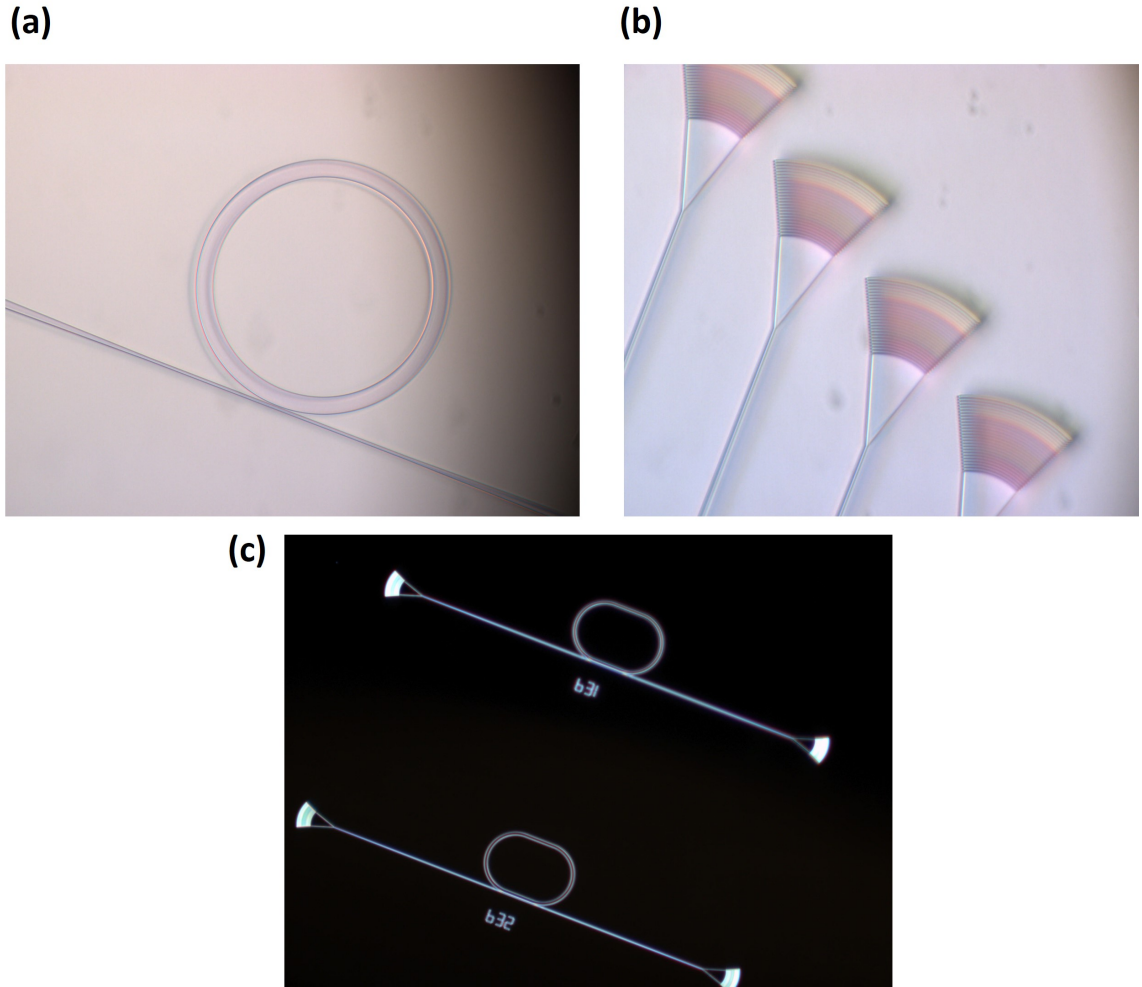
Figure 3.4: The optical image of the fabricated resonator and grating couplers. (a) A fabricated microring resonator coupled with a waveguide. (b) Some fabricated gratings coupled with waveguides. They can convert light from the vertical direction into the horizontal waveguide. The color in the grating results from the interference of visible light. (c) The picture of the total device ready for characterization.

the edge roughness in the mask. After developing the sample in 25% Tetramethylammonium hydroxide (TMAH electronic grade) and nitrogen blow dry, the sample is etched in inductively coupled plasma (ICP) reactive ion etching (RIE) machine, with an optimized flow of oxygen, argon, and carbon tetrafluoride (CF_4) as the etching agents. The selectivity of SiN:FOx has been around one. The process is followed by short wet etching in BOE 6:1 (to avoid major undercutting) and nitrogen blow dry.

Figure 3.4 shows some optical images we took under a microscope with different mag-
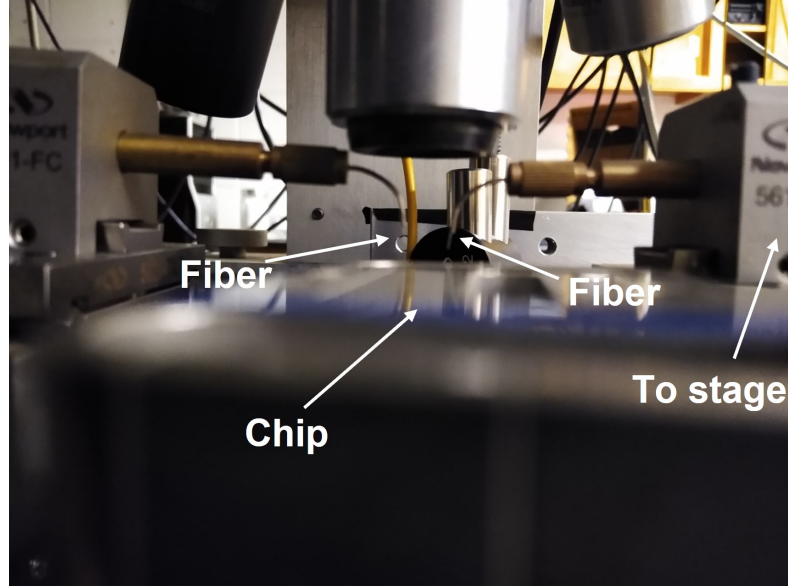
Figure 3.5: The characterization setup. Two fibers are fixed to around 80 degrees normal to the chip surface and are aligned by 5-axis stages to the input and output gratings on the chip. A $50\times$ long working distance objective is used together with a microscope system to see the microstructures.

nifications. The waveguide is tapered to a narrower width to couple light into and out of the resonator. The distance between the resonator and the waveguide is tuned to near the critical coupling condition. Two gratings are used to couple light in and out of the waveguide.

To characterize the Q of the microresonators, the continuous-wave (CW) laser light from a tunable diode laser is coupled to the fiber and passed through a fiber polarization controller. Then, as shown in Figure 3.5, the other end of the fiber is cleaved, and the tip of the fiber is fixed by a mount and a 5-axis translational stage. The fiber tip is around 80 degrees normal to the chip and is aligned to the gratings by using the stage and the imaging system. A Mitutoyo long working distance (LWD) objective is needed for the imaging system because of the vertical clearance requirement by the vertical fiber tip. The output grating is also similarly aligned with a multimode fiber tip to couple light out. A Si-amplified detector is used to detect the transmitted light and output an amplified voltage signal. The CW laser is swept in the wavelength range $\lambda = 770 - 780.5$ nm with 0.05 pm
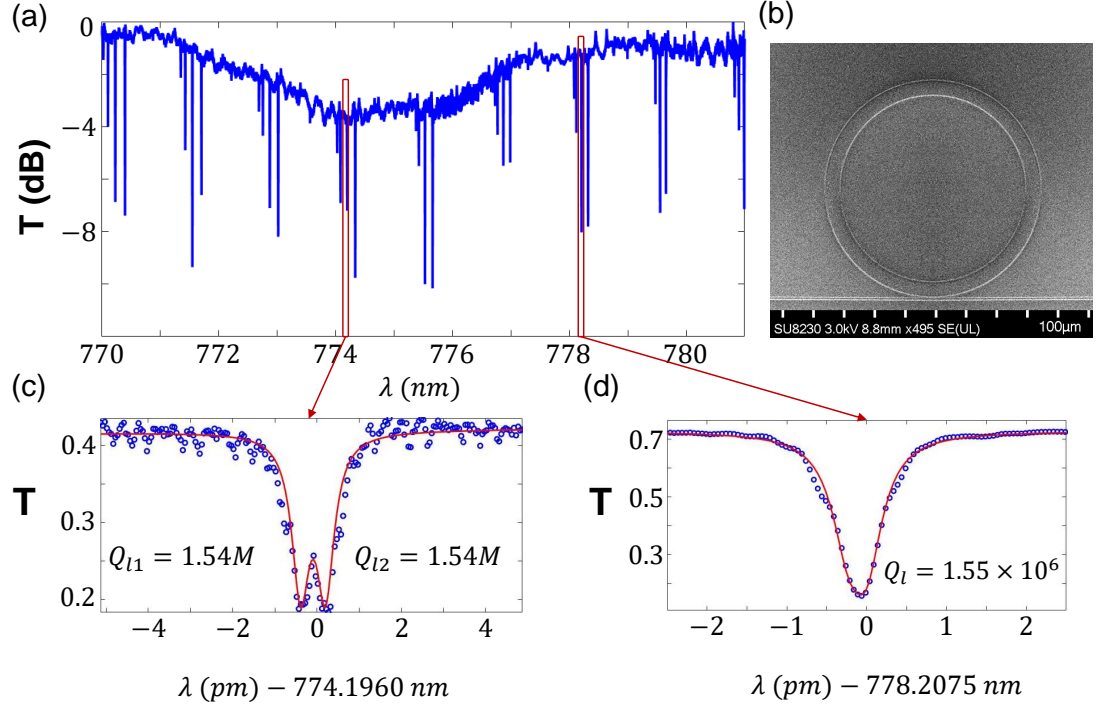
Figure 3.6: Optical characterization of the microring.(a) Normalized transmission through the waveguide, and (b) the scanning electron microscope (SEM) image of the fabricated microresonator with an outer radius of 35 μm and a width of 5 μm formed in a 287 nm-thick SiN on a $\mathrm{SiO_2}$ substrate. The microresonator is coupled to a bus waveguide with a gap distance of 100 nm. The gap size and the bus waveguide width are selected to achieve proper coupling to the $\mathrm{TE_1}$ mode of the resonator. The observed results show the operation in the under-coupled regime. In (a) families of modes spaced by ~ 1 nm can be seen. Within each family, the spacing is large enough to avoid intermode coupling. The $\mathrm{TE_1}$ family mode represents high-Q resonances as shown in the zoomed-in plots in (c) and (d). Loaded Qs at both resonant wavelengths $\lambda = 774$ (778.2) nm are above 1.5×10^6. Blue circles are experimental data and the solid red lines are fits to a double Lorentzian curve to account for the splitting of degenerate counter-clockwise resonant modes.

resolution. The collected transmission from the detector is then fitted to two-Lorentzian curves to take into account the intracavity coupling between counter-propagating modes. This facilitates the characterization of Qs associated with these modes. The characterization results are shown in Figure 3.6. The zoomed linear transmissions for two longitudinal resonant modes at $\lambda = 774.2$ nm and $\lambda = 778.2$ nm are depicted in Figure 3.6(c), and Figure 3.6(d), respectively, showing Qs larger than 1.5×10^6 for both modes. Figure 3.6(c) indicates the splitting between the counterclockwise and clockwise modes at $\lambda = 774.2$

49

nm. The splitting is proportional to the coupling between them, so for the resonant mode at $\lambda = 778.20745$ nm, the coupling is negligible. This resonator can be temperature tuned to the D_2 resonance of the ^{87}Rb atom at 780.24 nm. Since the chip needs to be heated to avoid atomic deposition, a shorter resonant wavelength is desired so that an increasing temperature will increase the resonant wavelength to the rubidium transition. The spectral temperature sensitivity is around $\approx$5.7 GHz/K. With $Q = 1.5 \times 10^6$, the resonance width (FWHM) is 256 MHz, which is much broader than the atomic resonance width of 6 MHz for Rubidium. Standard electronics with a temperature control of 1-2 mK or better can be used to achieve a good lock to the atomic transition while heating the device to an elevated temperature.

3.3.2   Simulations

From the introduction section in this chapter, we know that to simulate the dynamics of atoms interacting with the microresonators, we need to solve the Master equation (Equation 3.21) with the Hamiltonian (Equation 3.20). We can get the cavity decay rate κ from our characterization data, but the $g(\vec{r})$ factor needs to be calculated carefully with the simulated electric field of the resonator.

From Equation 3.9 we know

$$g(\vec{r}) = g_0 \cdot \frac{\sqrt{\epsilon_r}|E(\vec{r})|}{\cdot \max(\sqrt{\epsilon_r}E(\vec{r}))} \tag{3.24}$$

With $g_0 = -\overrightarrow{d}_{ge} \cdot \hat{\xi}\sqrt{\frac{w}{2\hbar\epsilon_r\epsilon_0 V}}$, and $V = \int dr^3 \frac{\epsilon_r|E(\vec{r})|^2}{\max(\epsilon_r|E(\vec{r})|^2)}$. The electric field distribution of the $\text{TE}_{1,486}$ mode is simulated by COMSOL and shown in Figure 3.7(a). The subscript numbers 1 and 486 indicate the radial and azimuth mode numbers, respectively. This TE mode is used because it has a higher Q than the first-order one, as its electric field peak is farther away from the outer ring sidewall, thus lowering the scattering losses.

In the Matlab program, a 4000×60000 grid (vertically more accurate) is generated to
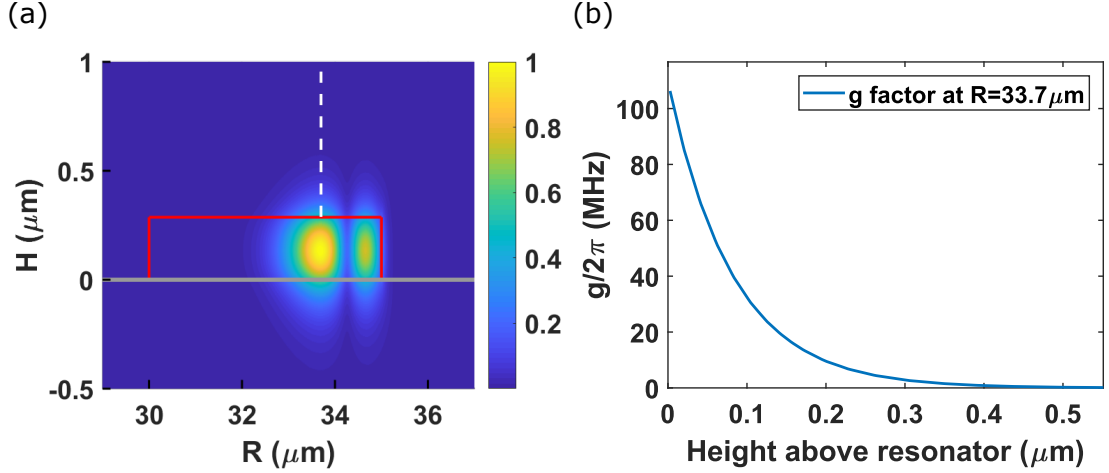
Figure 3.7: High-Q SiN resonator for strong atom-light interaction. (a) Normalized electric field distribution at the cross-section of the microresonator for the mode $\text{TE}_{1,486}$ with subscripts 2 and 486 showing the radial and azimuth mode numbers. The width of the SiN film bent to form the microring is 5 μm, with a height of 287 nm, and an outer radius of 35 μm. Red lines show the boundary of the SiN resonator, and the gray line shows the boundary of the SiO_2 substrate. (b) The atom-resonator coupling factor $g(z)$ along the vertical dashed line in (a) at the lateral maximum of the resonator mode intensity at radius $R = 33.7$ μm.

interpolate the electric field data from the COMSOL simulation to increase the resolution. Then, each grid cell is used as dA for integration in three dimensions. Since the resonator is a micro-ring, cylindrical symmetry is used for doing the calculation. The spatial varying ϵ_r of the system (Si_2O_3, SiN, and air) is also included in the calculation. The value of $g(R, z)$ at $R_0 = 33.7$ μm above the resonator surface is shown in Figure 3.7(b), where z is the height above the resonator surface, and R is the radius to the center axis of the ring. It is noticed that $g(R_0, z)$ decreases very fast with z, since it is an evanescent field, emphasizing the importance of air-cladding in resonator design. Our resonator achieves a single-photon vacuum Rabi frequency $2g(R_0, z_0) = 2\pi \times 64$ MHz around $z_0 = 100$ nm above the resonator while achieving a high Q with air-cladding. The single-atom cooperativity parameter is $C(R_0, z_0) = 4g(R_0, z_0)^2/\kappa\gamma \approx 2.7$ exceeds 1.

We can see from Figure 3.7(b) that the closer our flying atoms are to the resonator surface, the stronger the interaction is. But the limitations are the strong nonlinear Casimir-Polder force with the surface. We used an approximate formula for the Casimir-Polder
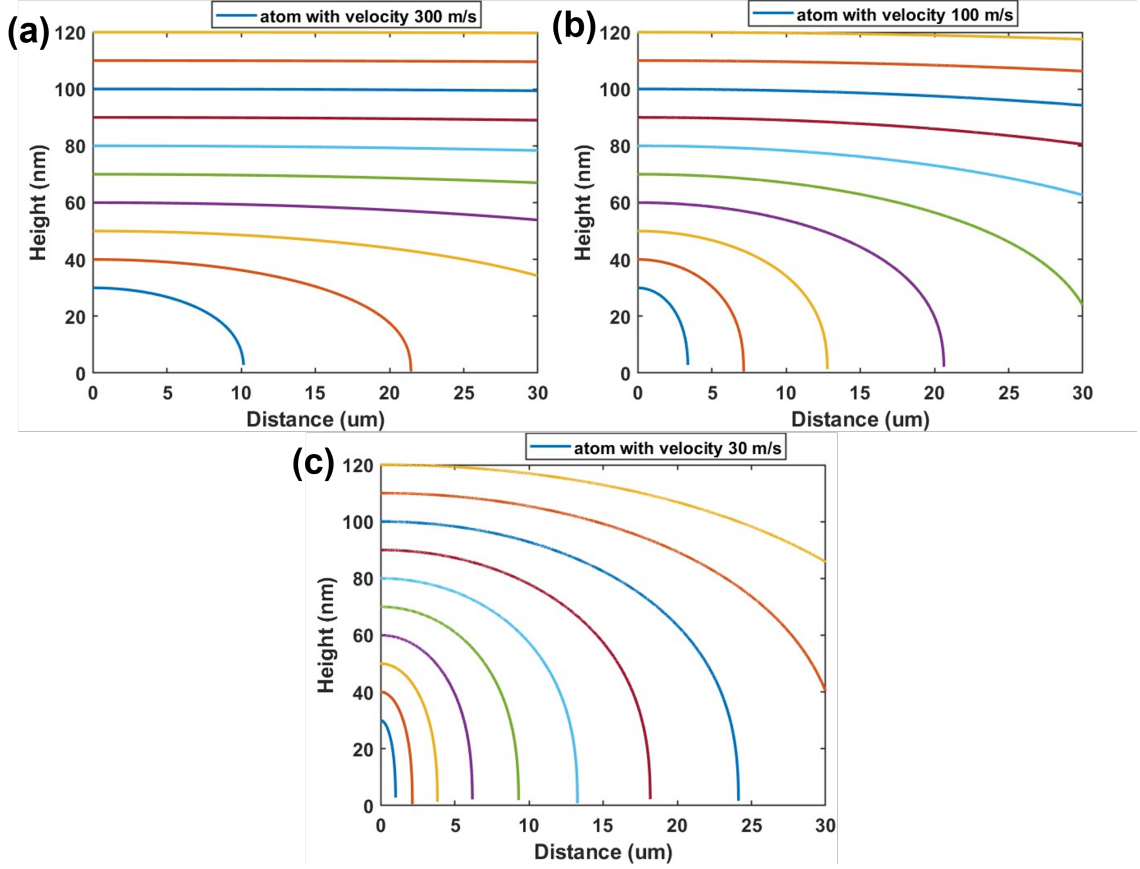
Figure 3.8: The atomic trajectories with different velocities and distances from the surface. (a) Atoms with a velocity of 300 m/s. (b) Atoms with a velocity of 100 m/s. (c) Atoms with a velocity of 30 m/s.

potential for Rb atoms (Ref [67] supplement)

$$U(z) = \frac{-C_3 \frac{\lambda_{\text{eff}}}{2\pi}}{z^3 \cdot \left(z + \frac{\lambda_{\text{eff}}}{2\pi}\right)} \tag{3.25}$$

Where $C_3/\hbar = 2\pi \times 1500$ Hz·μm^3, and $\lambda_{\text{eff}} = 650$ nm for SiN. We can see that the force increases dramatically when it gets closer to the dielectric surface. The different trajectories of atoms with different velocities are shown in Figure 3.8. The vertical (z) direction velocity is set to zero, and the transverse velocity of 300, 100, and 30 m/s is simulated with different heights from 30 nm to 120 nm. The faster the atom is, the closer it can get to the resonator without crashing, but the shorter the transit time. The transit time needs to be long enough to accumulate enough photons for an accurate measurement.

Thus, the system needs to be optimized with the interaction strength and the interaction time based on specific applications.

Figure 3.9(b) shows the transmission of the cavity versus laser detuning for both an empty cavity and a cavity containing one stationary atom 100 nm above the resonator at $R = 33.7$ μm. The peak splitting is the well-known vacuum Rabi splitting that is proportional to $2g(\vec{r})/2\pi$. If we set the excitation laser to zero-detuning and lock the resonator to the atomic transition, the presence of an atom will cause the transmission of the cavity to increase. With a constant excitation power, this will result in an increasing photon flux in the detector. For moving atoms, the change of the photon flux depends on $g(\vec{r}(t))$, and with single-photon counting modules as the detector, we can achieve the real-time monitoring of an atom transit.

The spatial coordinate of the atom, $\vec{r}(t)$, is computed and updated classically with an initial velocity and the Casimir force. Then, the corresponding $g(\vec{r}(t))$ is extracted based on the atom's location. We applied the adiabatic approximation in solving the Master equation (Equation 3.21) with slow atomic beams because the time scale for atomic transit (microseconds) over the resonator is much slower than the internal state evolution time (tens of nanoseconds) given $((g,\ \gamma,\ \kappa)/2\pi \approx (32, 6, 256)$ MHz) and we will confirm this approximation by full time-dependent calculations later. The Master equation is solved using the instantaneous value of $g(\vec{r}(t))$. The steady state of the master equation with each $g(\vec{r}(t))$ value is calculated, and the expected value for cavity decay and atomic decay is calculated accordingly.

Sample transits for atoms with different velocities are shown in Figure 3.9(c). The signals are displaced in time for a clearer view. The resonator size is the same as that in Figure 3.6 with a Q of 1.5×10^6. The extinction ratio at the critical coupling condition is assumed to be 13 dB. The horizontal and vertical velocities of the atom are set to zero. The number of transmitted photons increases as an atom flies closer to the resonator surface, and the double peak in the signal results from the two nodes in the TE$_1$ field distribution
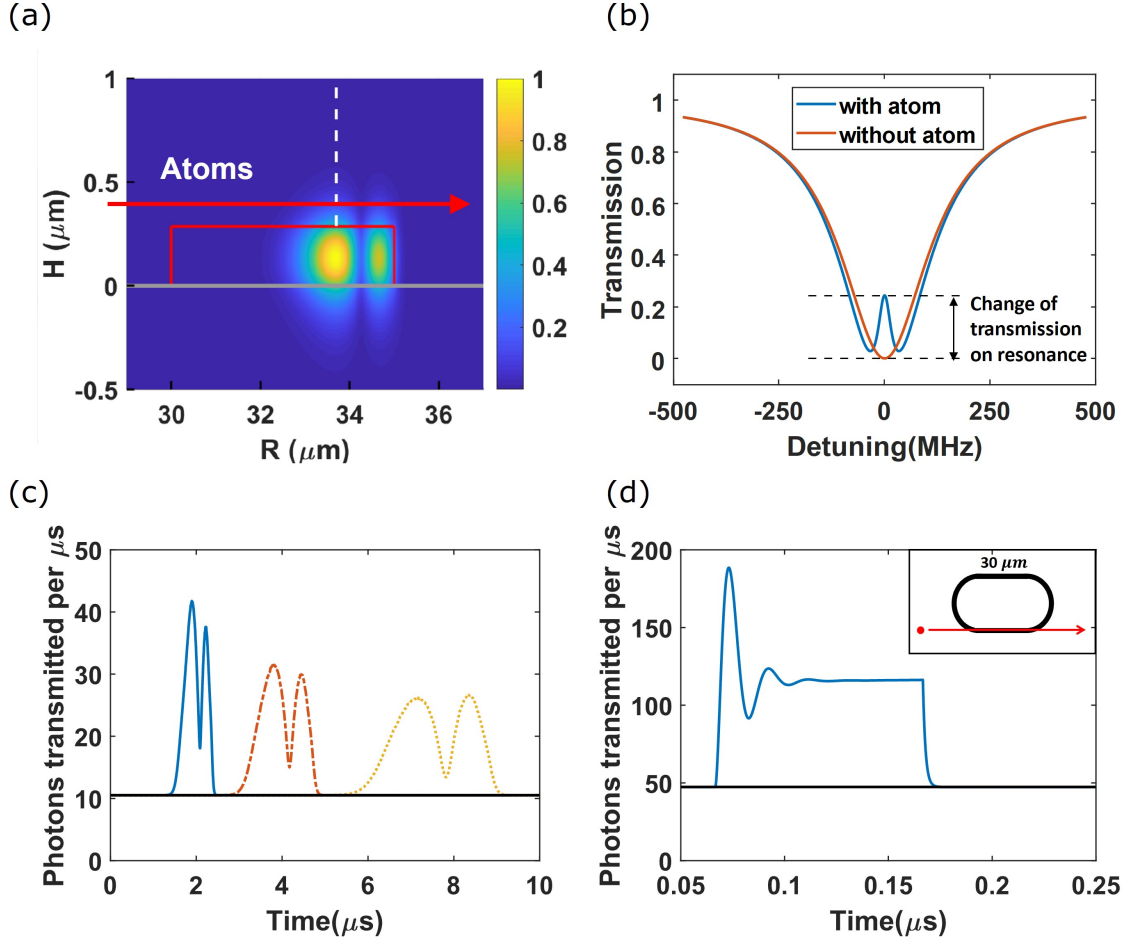
Figure 3.9: (a) The atoms transit through the evanescent field above the resonator. (b) Transmission spectra of excitation photons, with $g/2\pi = 32$ MHz, loaded $Q = 1.5 \times 10^6$, and 52.9 pW optical excitation power under the ideal critical coupling condition (the average number of photons in the resonator at zero detuning is ~ 0.12). The cavity is locked on resonance for atom sensing. (c) The detector signal when an atom flies above the resonator. The black reference line is the background signal from the imperfect critical coupling condition. Blue line: $v = 3$ m/s, $h_0 = 150$ nm; Red dash: $v = 1.5$ m/s, $h_0 = 190$ nm; Orange dot: $v = 0.8$ m/s, $h_0 = 230$ nm. The excitation power is 52.9 pW. The vertical and horizontal velocities are set to be zero. h_0 is the vertical distance between atoms and the top resonator surface. (d) The detector signal when an atom flies above a racetrack resonator (shown in the inset, with an extinction ratio of 13 dB in the critical coupling regime), with velocity $v = 300$ m/s, $h_0 = 100$ nm, and excitation power of 231.8 pW. The resonator is locked to $w_0 + kv_a$ to compensate the Doppler effect.

54

(See Figure 3.9 (a)). Atoms with a broad range of longitudinal velocities can be detected. The atom's height and longitudinal velocity determine the signal intensity and duration, respectively. The faster the atom, the closer it can be to the resonator without crashing and the more intense (but shorter) signal it creates. With these constraints, we estimate that atoms with 0.2 m/s to 30 m/s longitudinal velocities can be detected without crashing on the resonator. The atom beams with such velocities can be generated from a $2D^+$ MOT [76, 77] and delivered via microchannels as shown schematically in Figure 3.3. Interestingly, the ring configuration allows us to detect the same atom twice, and the time interval can be used to calculate the longitudinal velocity of the atom as well.

While the ratio $g/\kappa \approx 0.12$ achieved does not yet allow reversible atom-photon interactions, their interaction is still sufficiently strong to enable quantum device applications. For example, we envision that our platform could be used for a single-photon switch by single atoms, similar to what has been demonstrated using macroscopic resonators [78]. Using a $2D^+$ MOT with 1.8×10^{10} atoms/mm^2/s [76], which has an average longitudinal velocity around 8 m/s, we estimate that with an excitation power of 3.4 photons/μs and a Q of 1.5×10^6, we can achieve on average, a 50% contrast between "ON" and "OFF" states and a single photon routing rate around 10 kHz for each microchannel-resonator pair. The routing rate is much faster than those in the typical cold-atoms-dropping approach [79], which requires around one second to finish one cycle. If the resonator Q can be improved to 6×10^6, the contrast can be 85%, which is competitive with the cold atom systems but with much higher repetition rates due to the absence of a long dead time. The switch can be activated by the entry of a single atom into the vicinity of the resonator and by using fast electronics to detect the rise of detected photons in the first 100 ns time bin.

We have also fabricated racetrack resonators with $\sim 7 \times 10^5$ loaded Q. The quality factor is less than the ring resonator because of the extra loss from the mode propagating from the ring section to the straight section. We studied the potential use of racetrack resonators to detect thermal atomic beams generated by our microchannel-collimation of 100 °C Rb

vapor. Atomic vapors have recently been proposed for cavity quantum electrodynamics (QED) applications [51]. The advantage of our approach is the ability to place atoms with lithographic precision at a discrete location above the resonator. We designed a racetrack resonator with a R = 20 μm ring section and 30 μm straight sections and align its straight sections to our microchannels (see Figure 3.9(d) inset). In this way, the collimated thermal atoms with an average speed of 300 m/s will fly along the 30 μm straight section and strongly interact with the resonator for $\sim$ 100 ns. The transit time is thus much longer than the microring resonator and provides a detectable effect. The Master equation simulation of a thermal atom transit without adiabatic approximation is shown in Figure 3.9(d). The setup is similar to Figure Figure 3.3, and the Q of the racetrack resonator is assumed to be 1.5×10^6, with the transverse and vertical velocity set to be zero. The initial peak is the Rabi oscillation resulting from an atom entering the regime with a strong evanescent field of the racetrack and will be discussed later. If we monitor photons transmitted in 100 ns time bins and assume a 50% detection efficiency, we should find the number of photons jumping from 2.5 to $\sim$ 6, which indicates an atom transit.

3.3.3 Adiabatic approximation

This section will discuss the adiabatic approximation we used in previous simulations and compare it with the full-time-evolving method. The adiabatic approximation effectively means that we assume the internal state evolution time is much faster than the transit time, and the internal state will reach a steady state before the parameters change dramatically. For each time step dt, we update the location of the atom classically and find the corresponding $g(\vec{r})$. Then, we find a steady-state solution of the master equation with the instantaneous $g(\vec{r})$ and calculate expected observables with this quantum state. As for the full-time-evolving method, a much smaller dt is used, and each step evolves the density matrix according to Equation 3.21 and the instantaneous $g(\vec{r})$. The adiabatic approximation can save the computational time of the program and accelerate different iterations of sim-
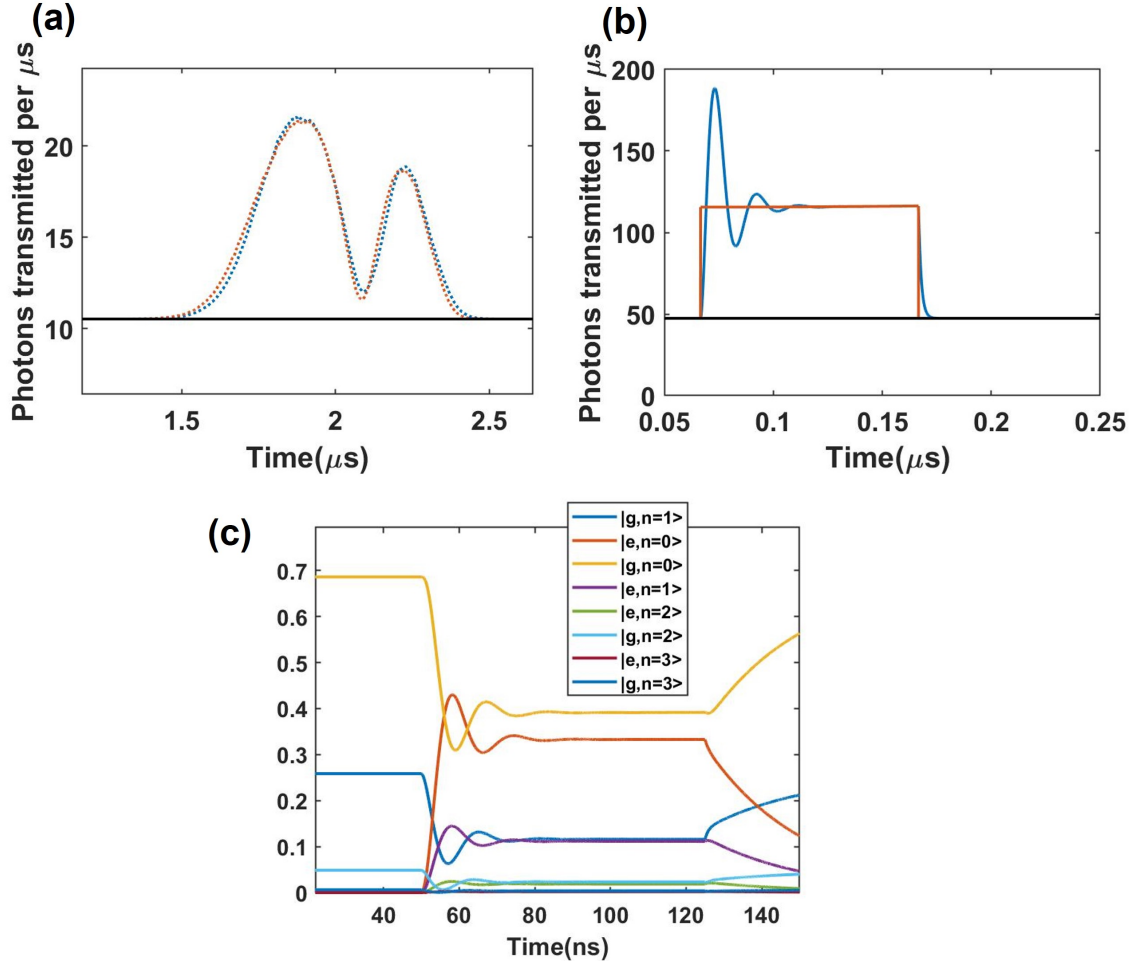
Figure 3.10: The comparison between simulations with and without approximation. (a) Simulation results for an atom transit above our ring resonator. The blue dashed line is the full-time evolving simulation result, and the red dashed line is the result with the adiabatic approximation. (b) Simulation results for an atom transit above the straight section of the racetrack resonator. The blue line is the result without approximation, and the red line is with the approximation. (c) The time evolution of each state in (b), we can see that the state reaches the steady state quickly within $\approx$30 ns.

ulations. Here, we simulated systems in the same condition with two different approaches and demonstrated the accuracy of this approximation.

Figure 3.10 shows the comparison results. In Figure 3.10(a) and (b), the blue line is the result of full-time-evolving simulation, and the red line is the simulation with the adiabatic approximation. Figure 3.10(a) simulates an atom with a velocity of 3 m/s transit through our microring resonator, and we can notice that the full-time-evolving method has a slightly slagged response to the change of $g(\vec{r(t)})$, but the difference is negligible in this time scale. Figure 3.10(b) is the comparison result for a 300 m/s atom transiting through the racetrack resonator. With a transit time of around 100 ns, the difference between the two methods is more prominent, which is the reason for using the full-time-evolving method in Figure 3.9 (c). The internal states extracted from the density matrix is shown in Figure 3.10(c). Here, g, e represents the atom in the ground state or excited state, respectively, and n means the Fock state with n photons. When the atom enters the evanescent field of the resonator, it interacts with the field and is driven toward the excited state. Thus, all the states with g decrease, and states with e increase. After a short oscillation period, the states converge to a steady-state solution. The full-time-evolving result shows some lagging and over-shooting features compared with adiabatic approximation. However, the average change of transmitted photons remains roughly the same.

3.3.4　Microing resonators with cold atoms

Besides the single photon single atom interaction regime, the microresonator can also be used to interact with a group of atoms. Our system has the potential to build miniaturized devices like atom interferometers and inertial sensors within this regime. This section will summarize our simulation efforts in utilizing our high Q microring resonator to detect periodical transits of cold atoms.

Our collaborator in the Air Force Research Laboratory (Dr. Spencer E. Olson, Dr. Matthew B. Squires, et al.) has put wires on the back of their chip outside of the vacuum chamber to create strong magnetic traps. Bose-Einstein condensate (BEC) was achieved with these magnetic traps combined with a 2D MOT [80, 81]. The cold atomic cloud is trapped on the chip surface by the magnetic trap, and its transit above our micro-ring resonator will have a huge detectable effect, which could be used for building precise accelerometers. Figure 3.11 shows the concept of the experiment. The cold atomic cloud is controlled by two external magnetic traps— A vertical magnetic trap in the Z direction with a frequency of 2 kHz and a transverse magnetic trap in the X direction. The vertical magnetic trap prevents atoms from crashing into the chip, and the transverse trap makes the atomic cloud periodically transit the microring resonator. The cross-section of the chip and the resonator is shown in Figure 3.11. Only the left section of the resonator is used to interact with the atoms. The green dashed line is the center of that waveguide and is also the center of the transverse magnetic trap. The atoms are initially placed around 20 μm left of the green dashed line in the X direction. We have learned that the Casimir force will be dominant when the distance between atoms and the dielectric surface is very small. Thus, the silicon dioxide layer should be etched 1000 nm down to reduce the atoms lost per transit.

The resonator we used in the simulation has a radius of 16 μ m, and a width of 1.1 μm. The resonator is still critically coupled with an extinction ratio of 13dB. But here, we utilized the TM mode electric field pattern of the resonator. The reason for using TM
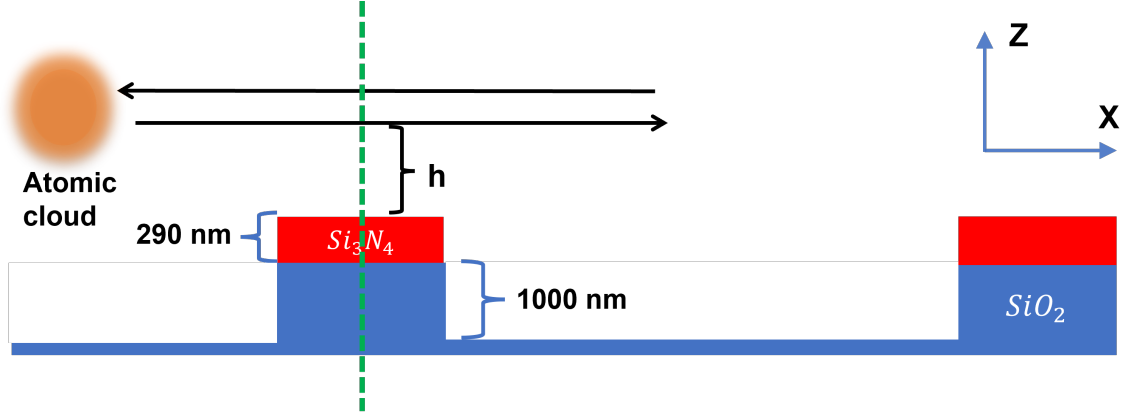
Figure 3.11: The schematic figure for detecting multi-transits of the atomic cloud with microring resonator. The cold atomic cloud is controlled by a vertical magnetic trap and a horizontal trap.

mode as an improvement over TE mode is that the electric field of TM mode extends more into the air. In TM mode, the dominant electric field is perpendicular to the resonator top surface, and the continuous condition is $E_{air} = \epsilon_r E_r$. However, for the TE model, the dominant electric field is parallel to the resonator top surface, and thus $E_{air} = E_r$. As shown in Figure 3.12(a), the electric field increases its magnitude after crossing the upper boundary between the resonator and the air. From Equation 3.9 we know that

$$g(\vec{r}) = g_0 \frac{\sqrt{\epsilon_r}|E(\vec{r})|}{\max(\sqrt{\epsilon_r}E(\vec{r}))}$$

A higher electric field will provide a higher g factor. Figure 3.12 (b) shows the calculated g factor of the TM mode in a vertical line at R=15.5 μm, $g/2\pi = 200$ MHz at H=0.4 μm. As a comparison, we also simulated the TE mode of the same resonator and the calculated $g/2\pi = 115.8$ MHz at H=0.4 μm. Thus, the TM model of the microresonator is more suitable for interacting with atoms, providing a stronger interaction strength. With the same g factor, the TM mode can allow the cold atomic cloud to stay further away from the resonator to reduce atoms lost due to the Casimir force, which is crucial for achieving multiple transits. On the other hand, the TM mode of the resonator has a lower quality factor compared with the TE mode because it is more affected by surface roughness. As a
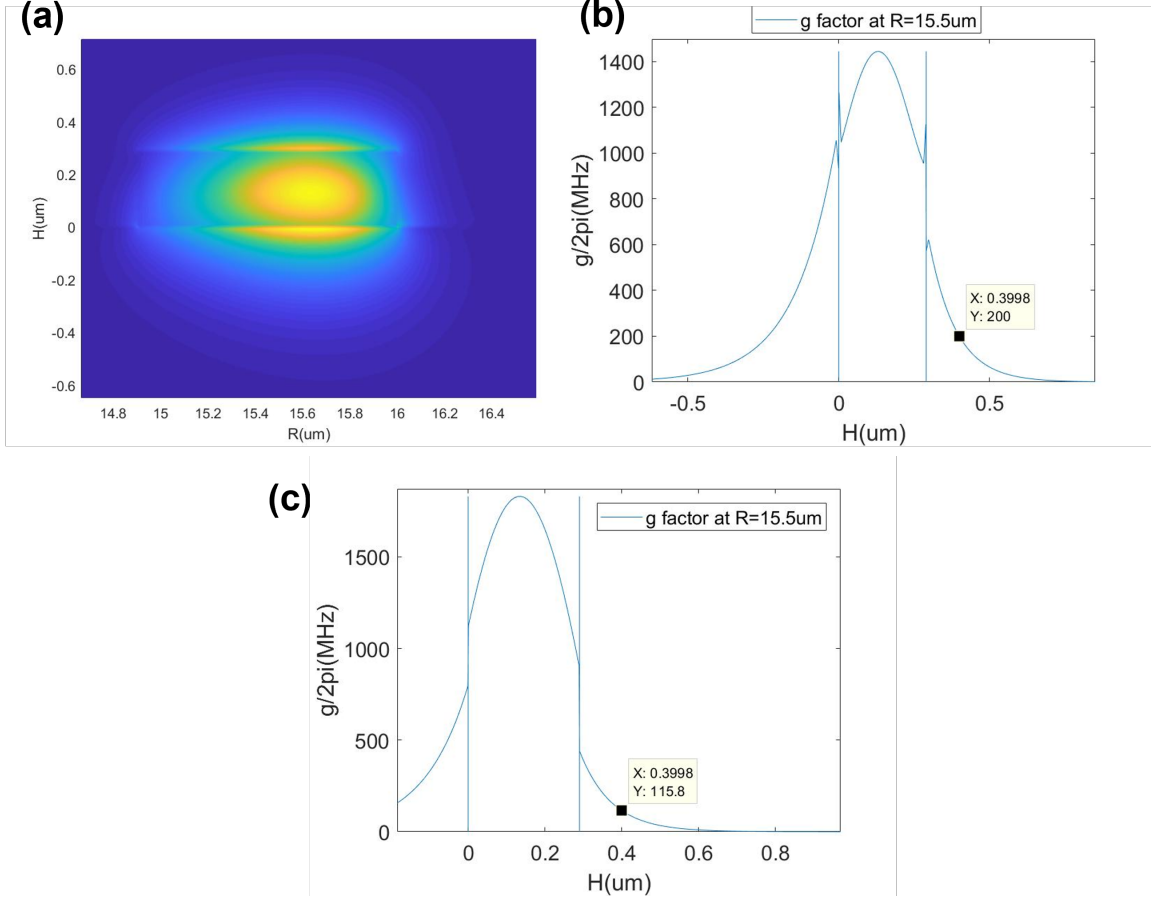
Figure 3.12: (a) The TM mode electric field distribution of a microing resonator with a radius of 16 μm. The width of the resonator is 1.1 μm (from R=14.9 to 16 μm), and the height is 0.29 μm (from H=0 to 0.29 μm). (b) The g factor at different H at R=15.5μm for the TM mode in (a). At H=0.4 μm, $g/2\pi = 200$ MHz (c) The g factor at different H at R=15.5μm for the TE mode in the same resonator of (a). At H=0.4 μm, $g/2\pi = 115.8$ MHz

result, we assume that the resonator has a quality factor of 0.5 million with the TM mode.

For the interaction between a cloud of atoms and the resonator, we can still use Equation 3.20 and Equation 3.21 to simulate the system. The single atom g factor needs to be replaced by an effective g' factor for the collective mode of the atoms. The effective g' factor can be calculated by [27]:

$$g' = \sqrt{\sum_i g_i(\vec{r_i})^2} \tag{3.26}$$

Where the summation is over all atoms within the cloud.

In the simulation, the cloud temperature is set to 150 nK. One thousand atoms are generated with initial velocities v_i and initial position r_i, which are defined by:

$$v_i = v_{center} + v_{thermal}(i)$$

$$r_i = r_{center} + r_{thermal}(i)$$

(3.27)

Where the thermal velocity $v_{thermal}(i)$ and thermal position $r_{thermal}(i)$ is randomly chosen from a Maxwell-Bolzmman distribution with a temperature of 150 nK. v_{center} and r_{center} are the mean velocity and mean position of the atomic cloud, respectively. The initial v_{center} is set to have a zero vertical velocity while the transverse velocity is set to 16 times the recoil velocity ($16\hbar k/m \approx 16 \times 5.9$ mm/s). Since the effective g' factor is much larger than the single atom case, the height of the atomic cloud to the resonator surface is increased to 800 nm to reduce atoms lost. The center of the vertical magnetic trap has the same height as the initial atomic cloud. The cloud center is placed at 20 μm left of the green dashed line. Atoms that crashed on the chip are counted and removed from the calculation. To save the simulation load, the horizontal grid size for the electric field is increased to 16 nm, and the vertical grid size is increased to 6 nm.

The simulation result with a horizontal trap frequency of 500 Hz is shown in Figure 3.13. Figure 3.13 (a) shows the transmission versus time for the first six transits. 35% of the atoms are lost after six transits. The first transit created a great transmission peak, but the sequential transits had less and less effect on the resonator. To find the reason, we also plotted the time-evolving vertical position and the horizontal position of the atomic cloud. The size of the atomic cloud is also calculated based on the standard deviation of the atoms' distances to the center. Figure 3.13(b) shows that the vertical position of the atomic cloud is perturbed every time the cloud transit the resonator. The Casimir force keeps enhancing the oscillation amplitude every time the cloud is above the resonator surface, causing a bigger and bigger oscillation of the cloud. The interaction between the atoms and the resonator is

Figure 3.13: The simulation result with 500 Hz horizontal magnetic trap and 2 kHz vertical magnetic trap. The input power is 5 pW. (a) The transmission versus time for the atomic clouds. The transit time is around 50 μs for each peak. (b) The vertical position of the atomic cloud versus time. (c) The cloud radius (calculated by the standard deviation) versus time. (d) The horizontal position of the atomic cloud versus time.

thus compromised, and the transmission peaks are reduced.

From Figure 3.13(c) and (d), we can see that the atomic cloud is harmonically oscillating in the horizontal direction with the transverse trap. The size of the cloud oscillates twice the frequency of the transverse trap, and the atomic cloud is the largest when the cloud passes the center of the transverse trap and has the largest transverse velocity. The simulation in Figure 3.13 has the trap frequency $f_{vertical} = 4 \times f_{horizontal}$. We know that it needs a quarter of the period for the cloud to move from the side to the resonator. When the vertical frequency is an even multiple of the horizontal frequency, every time the cloud is over the resonator, its vertical location is at the center of the vertical magnetic trap, and it has the largest vertical speed and cloud size. This leads to more variance in the Casimir

Figure 3.14: The simulation result with 400 Hz horizontal magnetic trap and 2 kHz vertical magnetic trap. The input power is 5 pW. (a) The transmission versus time for the atomic clouds. The transit time is around 50 μs for each peak. (b) The vertical position of the atomic cloud versus time. (c) The cloud radius (calculated by the standard deviation) versus time. (d) The horizontal position of the atomic cloud versus time.

force each atom experiences and creates more fluctuations in each transit. Suppose we change the horizontal trap frequency so that the vertical trap frequency is an odd multiple of the horizontal frequency. In that case, the cloud should have the minimum vertical speed and cloud size when interacting with the resonator. Figure 3.14 shows the simulation result with $f_{horizontal} = 400$ Hz. Figure 3.14 (a) shows the transmission versus time for the first five transits. The transmission peaks are much stronger after the first transit compared with Figure 3.13. Figure 3.14 (b) also reveals that the vertical position of the atomic cloud has a much more stable oscillation. This demonstrated that tuning the horizontal magnetic trap frequency can greatly improve the multi-transit signal. 36% of the atoms are still lost
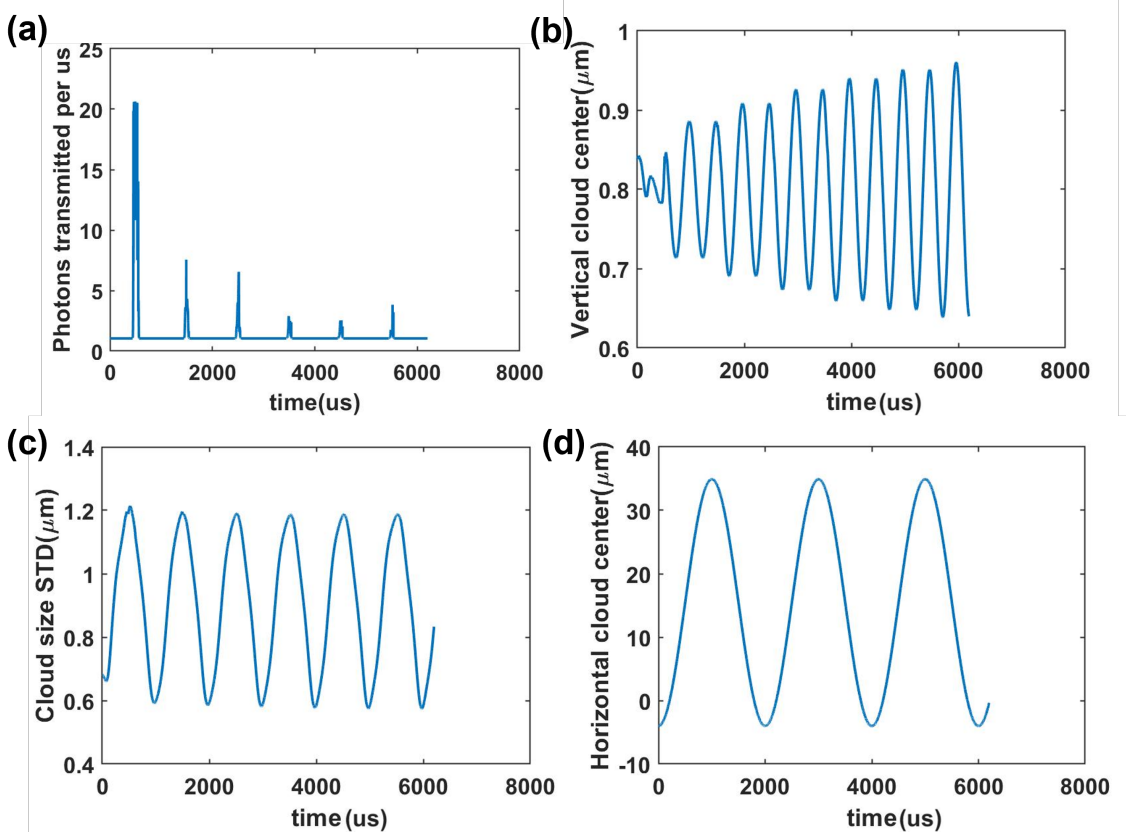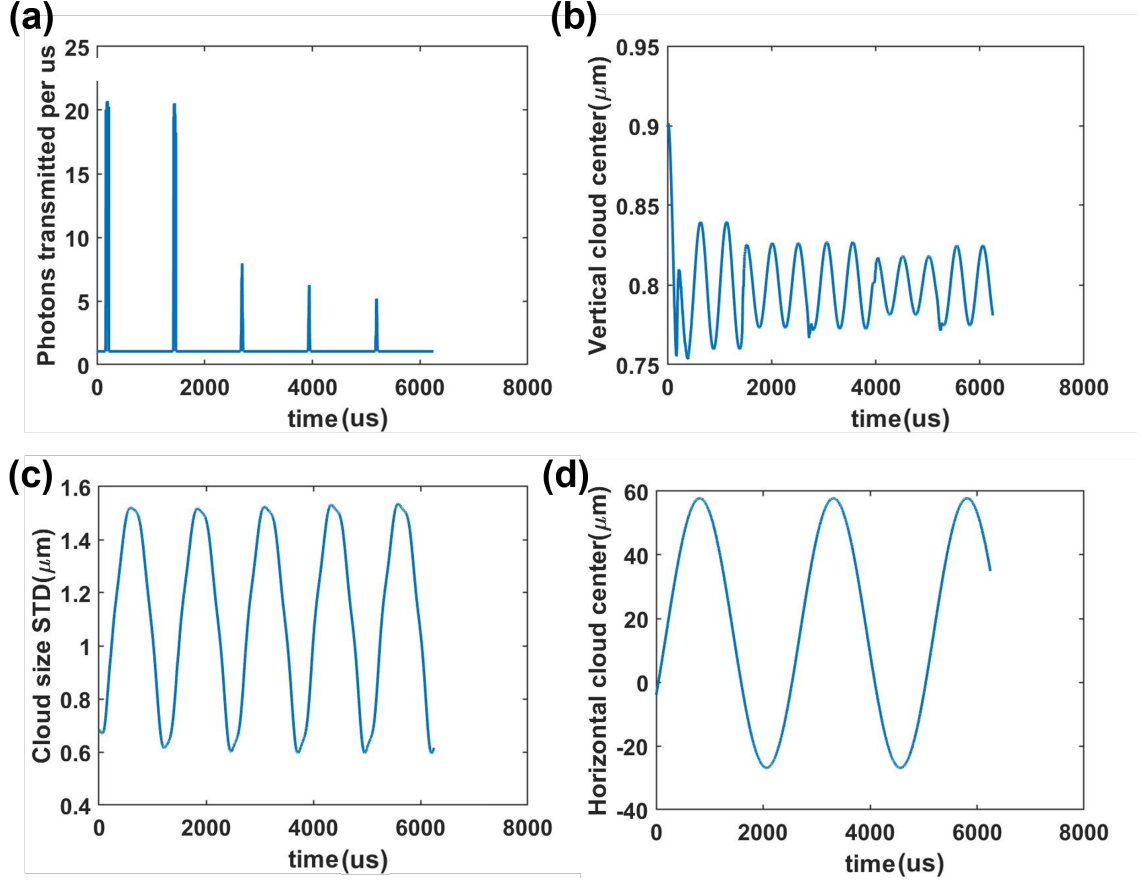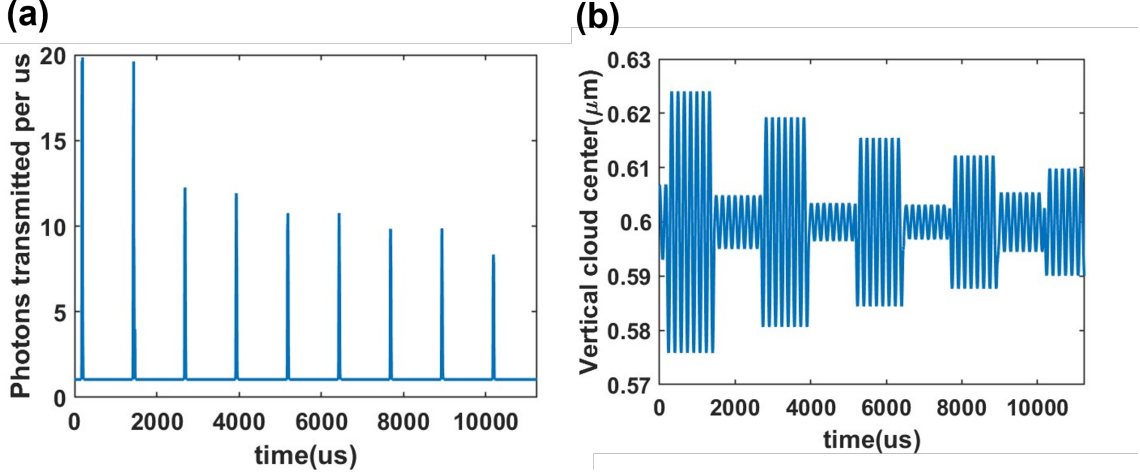
Figure 3.15: The simulation result with 400 Hz horizontal magnetic trap and 6 kHz vertical magnetic trap. The input power is 5 pW. (a) The transmission versus time for the atomic clouds. The transit time is around 50 μs for each peak. (b) The vertical position of the atomic cloud versus time.

after five transits, which is limited by the vertical trap potential. The Casimir force is much stronger than the magnetic force for the atoms near the resonator surface.

The 2 kHz vertical trap frequency is not the maximum frequency that can be achieved on-chip [80, 10]. Since our resonator chip is only 500 μm thick and can be even thinner if needed, a stronger magnetic trap is feasible. We simulated the scenario where the vertical magnetic frequency is increased to 6 kHz, and the horizontal frequency is kept at 400 Hz. Then, with a stronger vertical trap potential, we lower the atomic cloud height to 600 nm above the resonator to increase the interaction strength.

The simulation results are shown in Figure 3.15. The transmission peaks remain strong after nine transits of the atomic cloud. As shown in Figure 3.15 (b), the vertical position of the cloud also oscillates very stably in a finite range. At the end of the simulation, only 4% of the atoms are lost, demonstrating that a robust multi-transit of a cold atomic cloud with our resonator is feasible. These simulations provide important insights into the interaction between cold atomic clouds and chip-scale microring resonators, paving the way for using nanophotonic resonators to make chip-scale devices in the field of inertial sensing and quantum information.

3.4 Efficient edge coupling

The resonators we used in section 3.3 are coupled with a waveguide, and the waveguide is coupled with two gratings on each end (see Figure 3.4). The light from a fiber tip can be coupled to the grating and eventually to the resonator. There are several advantages of using grating couplers. First, it is a mature and commonly utilized approach, and the gratings are relatively easy to design and fabricate. Second, the coupling is achieved with the fiber tips in the vertical direction perpendicular to the chip, providing great flexibility in designing the devices. Especially in the early stage of fabrication, many devices need to be fabricated and tested to explore the parameter space. With grating couplers, tens or even hundreds of devices can be fabricated on the same chip and individually coupled and characterized. Third, the grating coupler is polarization selective [82]. Combined with polarization control of the input light, this property can be used to couple light into a specific mode of the resonator.

However, the coupling efficiency of grating couplers is usually not big enough with a simple focusing grating design. Using apodized gratings or combining the grating with a bottom reflector can greatly improve the coupling efficiency [82]. But the fabrication challenges and the compatibility with the intended device make it hard to implement. On the other hand, as shown in Figure 3.5, each fiber needs a special metal tube bent to around 80°to hold the fiber tip vertically and a precise 5-axis stage to align the fiber with the grating. The whole setup is huge and bulky. For application with alkali atoms, the coupling needs to be inside a vacuum chamber. This huge setup is not compatible with most of the chambers and is against the purpose of miniaturization and scalability. As the simulation in section 3.3 shows, for thermal atoms, the transit time is very short with the microresonators. The accumulated signal difference is only a couple of photons per transit and will suffer from the Poisson noise. On the other hand, the requirement of high vacuum compatibility and size limit puts extra constraints on the coupling strategy. Thus, a crucial part of our
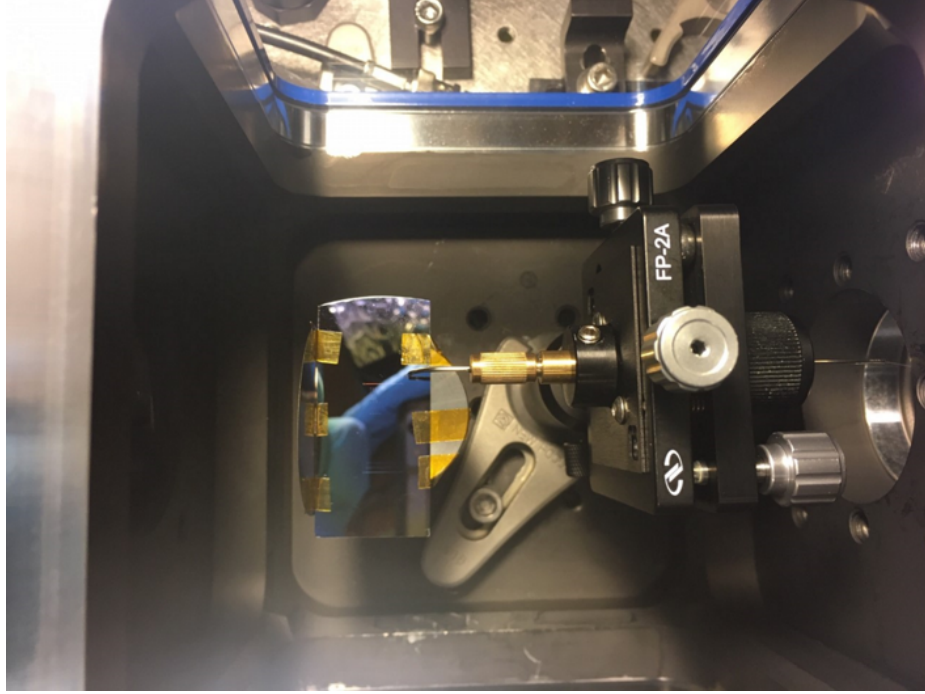
Figure 3.16: Our compact setup to couple light between the fiber and the grating inside the vacuum chamber.

cavity QED platform is connecting it with the outside world with high enough efficiency in a compact approach. Efforts must be committed to finding a flexible, highly efficient, and vacuum-compatible approach for coupling light in and out of the microresonators.

Figure 3.16 shows a compact setup we used to couple light between the fiber and the grating inside the vacuum. A small 5-axis stage is used together with a special holder for a metal tube. A customized Teflon fiber feedthrough mounted on a Swagelok fitting is used to deliver the bare fiber into the vacuum chamber [83]. The fiber is fixed with the metal tube to keep it vertical to the chip. The vacuum chamber we used is a six inches cubic vacuum chamber from Ideal Vacuum. As we can see, the chamber can only accommodate one fiber coupler to the grating. The other grating has to be coupled from free space outside of the chamber. This setup has a low coupling efficiency and is hard to operate. With this setup, an experiment was conducted where we tried to utilize a focusing grating to collect fluorescence from rubidium atomic vapors. However, the signal collected out of the fiber was only around 100 photons/s, which is too weak for more meaningful measurements.

Thus, the details of this experiment are not included in this thesis.

Edge coupling, on the other hand, is a major approach to couple light into the waveguide with high efficiency and high power limit [84, 85]. Many groups in the atomic optics field have etched v-grooves on-chip to hold fibers close to tapered waveguides, achieving highly efficient and compact edge coupling in the vacuum [86, 87]. Another novel approach is that instead of bringing the fiber on the chip, the free-space laser beam is focused by a long working distance (LWD) objective outside of the chamber into the end of the waveguide [88]. It can achieve high coupling efficiency and allows us to switch easily between different devices. This strategy does not require any extra mounts to be put in the chamber nor use epoxy to glue the fibers on the chip. All the optics are outside the vacuum chamber, and the free space laser beam can be easily tailored and manipulated without breaking the vacuum. As a result, we decided to adopt this approach to our system, and this chapter describes our efforts in realizing this novel approach.

3.4.1 Design and Characterization

Prof Ali Adibi's group designed and fabricated the edge coupling chip. The chip has the same fabrication process as we discussed in section 3.3. The chip layout is shown in Figure 3.17. There are six waveguides in a Z shape configuration; three are also connected to a resonator for testing. The waveguide is tapered from a width of 600 nm to 80 nm gradually over a 1.6 mm distance toward to edge of the chip (shown in the red circle in Figure 3.17). The waveguide mode is slowly converted into an expanding mode and eventually emitted out of the edge of the chip. Since below the 300 nm thick waveguide is the silicon dioxide layer and above the waveguide is air. An extra layer of SU8 photoresist (shown as blue in Figure 3.17) is deposited on top of the waveguide at the tapering region to make sure the mode expands more symmetrically with the tapering process. The SU8 has a refractive index of ≈ 1.56 at 780 nm, which is pretty close to the silicon dioxide (≈ 1.45 at 780 nm). The cross-section of the SU8 has a size of 4.5 μm times 4.5μm to accommodate the expanded
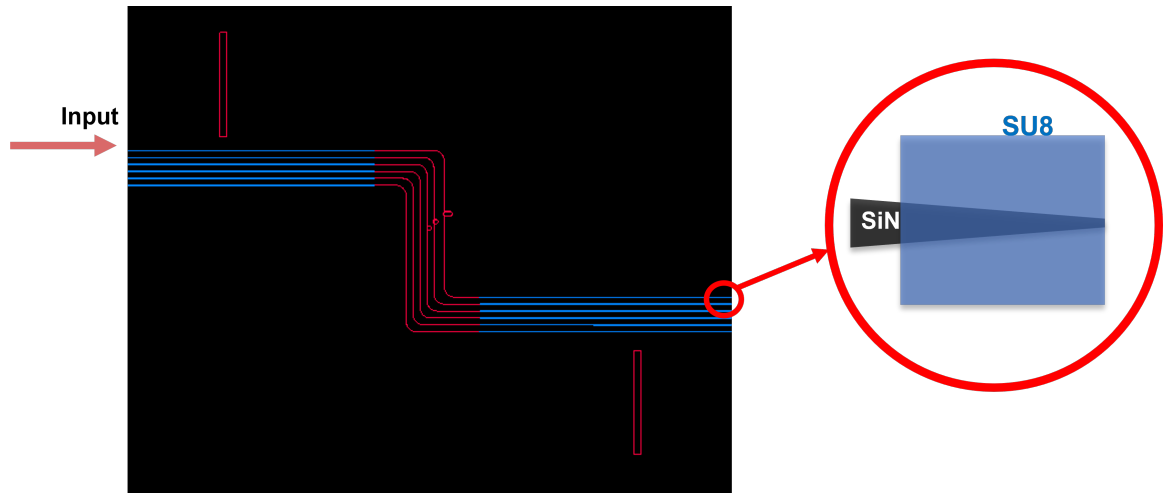
Figure 3.17: The chip designed for edge coupling with a free space laser beam. Six waveguides are shown, and three of them are coupled to resonators. As shown in the red circle, the end of the waveguide is tapered to let the mode expand. The tapering region is covered with SU8 photoresist (blue color) to let the mode expand symmetrically. The chip is cleaved properly to expose the end of the waveguide and let the mode expand into free space.

mode. SU8 is not the best candidate since the refractive index does not match perfectly, and the transmission is only around 75% at 780 nm [89]. Nevertheless, using it does not require designing and testing an extra fabrication procedure.

To characterize the edge coupling chip, we first need to measure the mode divergence of the light emitted from the end of the waveguide. Then, we can focus our laser beam to match that divergence to achieve a good coupling efficiency. As shown in Figure 3.18 (a), a cleaved fiber tip is used to couple light into the waveguide from the end of the chip. The coupling efficiency of fiber to the waveguide is not important as our purpose is to measure the output beam divergence. The output from the other side of the waveguide is collected by a lens set and a camera. One measured beam profile of the emitted light from the other side of the waveguide is shown in Figure 3.18 (b). The beam profile is very close to a slightly elliptical Gaussian beam. To measure the divergence of the output beam, the imaging system, which is mounted on a translational stage, is moved along the beam propagation direction to measure the beam size versus distance. The data is shown in Figure 3.18 (c). The x-axis is the position labeled on the translational stage; thus, only
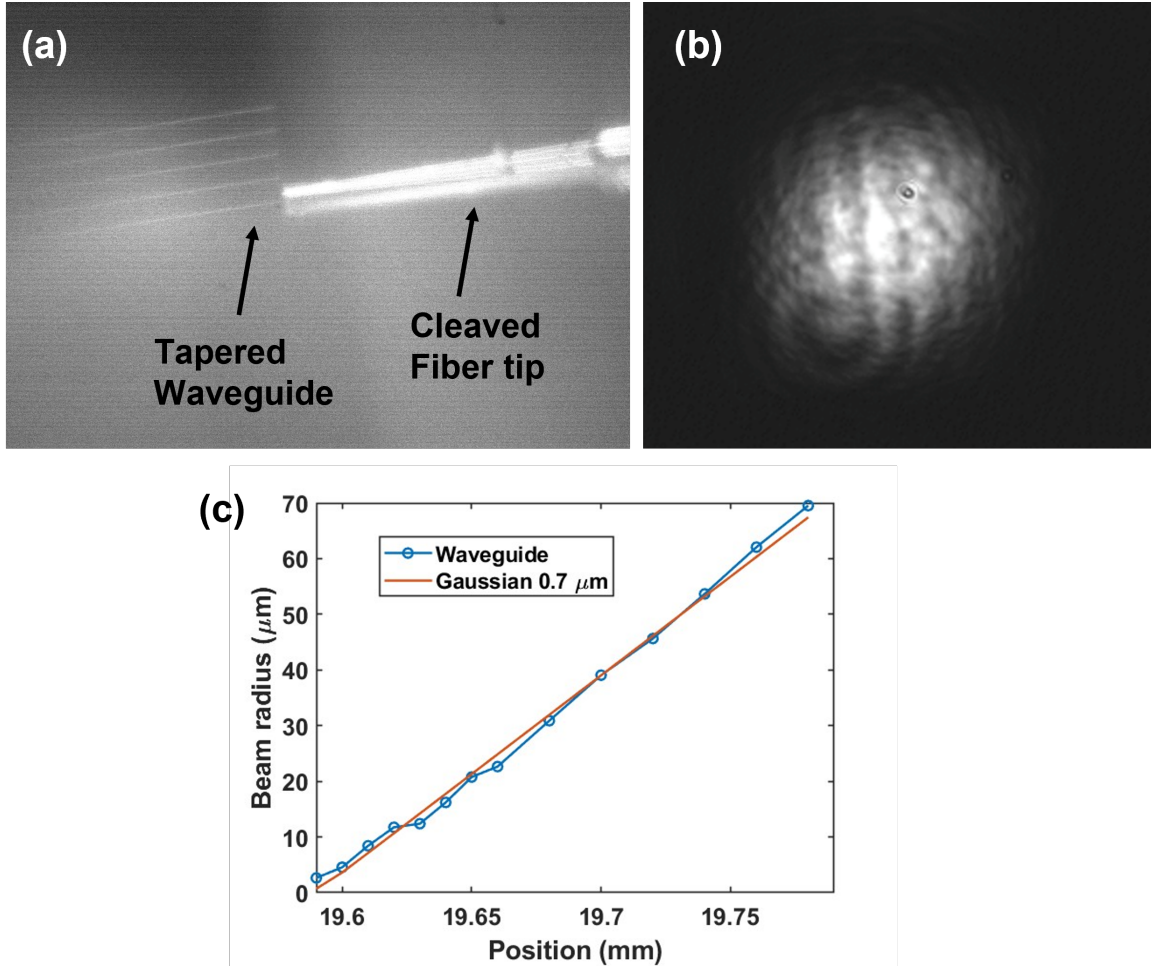
Figure 3.18: Matching the mode of the edge coupling chip. (a) An optical image of the fiber coupling approach. A cleaved fiber tip is held by a 3D stage to couple light into the waveguide. The SU8 is visible in the image. (b) The measured beam profile of the emitted light out of the waveguide. (c) The measured emitted beam size at different distances. The a-axis is the position labeled in the translational stage. The blue dots line is the measured data, and the red line is the theoretical beam divergence of a Gaussian beam with a radius of 0.7 μm.

the change in its value is meaningful. For a Gaussian beam, the beam radius w follows a hyperbolic relation:

$$w(z) = w_0 \sqrt{1 + (\frac{z}{z_R})^2} \qquad (3.28)$$

Where z is the axial distance from the beam's focus, z_R is the Rayleigh range $z_R = \pi w_0^2 / \lambda$. We found that a Gaussian beam with a waist radius w_0 =0.7 μm fits the divergence of the waveguide beam very well (Figure 3.18(c)). The corresponding numerical aperture (NA) is around 0.32.

With the beam divergence information, we can now use free space optics to match this beam mode. The setup is shown in Figure 3.19. First, the output laser from a polarization-maintaining fiber patch cable is collimated using an aspheric lens with a 6.24 mm focus length (Thorlabs C110TMD-B). Then, a long working distance (LWD) objective with 50X magnification (Mitutoyo Infinity Corrected) is used to focus the laser beam to around 0.7 μm waist radius to match the waveguide mode. The output on the other end of the waveguide is collected by another 50X LWD objective, then imaged on a camera or photodetector.

To accurately align the laser beam with the end of the waveguide, the input objective is first removed, and the laser beam is roughly aligned to hit the edge of the chip where our six waveguides locate. Another imaging system not shown in Figure 3.19 is placed perpendicular to the chip to look at the chip surface and monitor the scattering light. When the rough alignment is finished, a bright scattering spot can be seen covering all six waveguides. Then, the input objective is added back. Two mirrors and a miniature 2D translational mount (Thorlabs LM1XY) are carefully tuned to align the laser spot to one of the waveguides. During this process, the focused laser should create a tiny bright laser scattering spot on the edge of the chip, which is used as a location indicator. Finally, the distance between the objective and the waveguide is changed, together with other degrees of freedom, to move the focus of the laser beam onto the waveguide, matching the waveguide mode and achieving the highest coupling efficiency. Figure 3.20 shows an image of the chip after
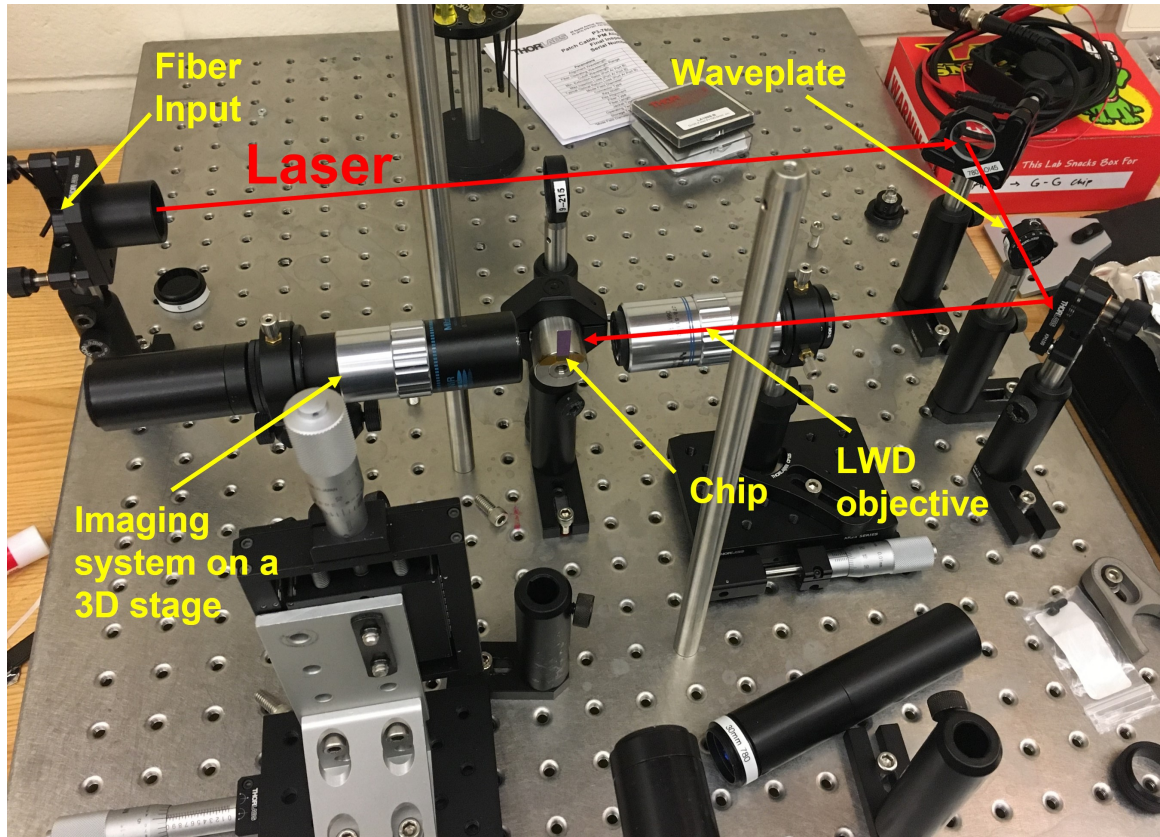
Figure 3.19: Free space setup to characterize the edge coupling chip. The laser emitted from a polarization-maintaining fiber is collimated and directed to the LWD objective. A $\lambda/2$ waveplate is used to control the polarization of the laser. A miniature 2D translational mount and a 1D translational stage are used to manipulate the input objective. The imaging system is composed of an objective plus a plano-convex lens mounted on a 3D translational stage.

all the alignments. Because of the surface roughness, all waveguides and resonators will create scattering light into the environment, which can be seen in the image. The laser is tuned to the resonance frequency of the microring resonator. Thus a bright ring can be seen on the left side of Figure 3.20. In the middle of the image, the end of the SU8 layer is also quite bright, indicating a high-loss section. The SU8 layer has a fixed width of 4.5 μm and a fixed height of 4.5 μm, covering the whole 1.6 mm region where the waveguide is gradually tapered. When coupling the free space light into the waveguide, some of the modes in SU8 are not fully coupled and create a big scattering at the beginning wall of the SU8 layer. This loss could be reduced by creating a tapering region of the SU8 near the
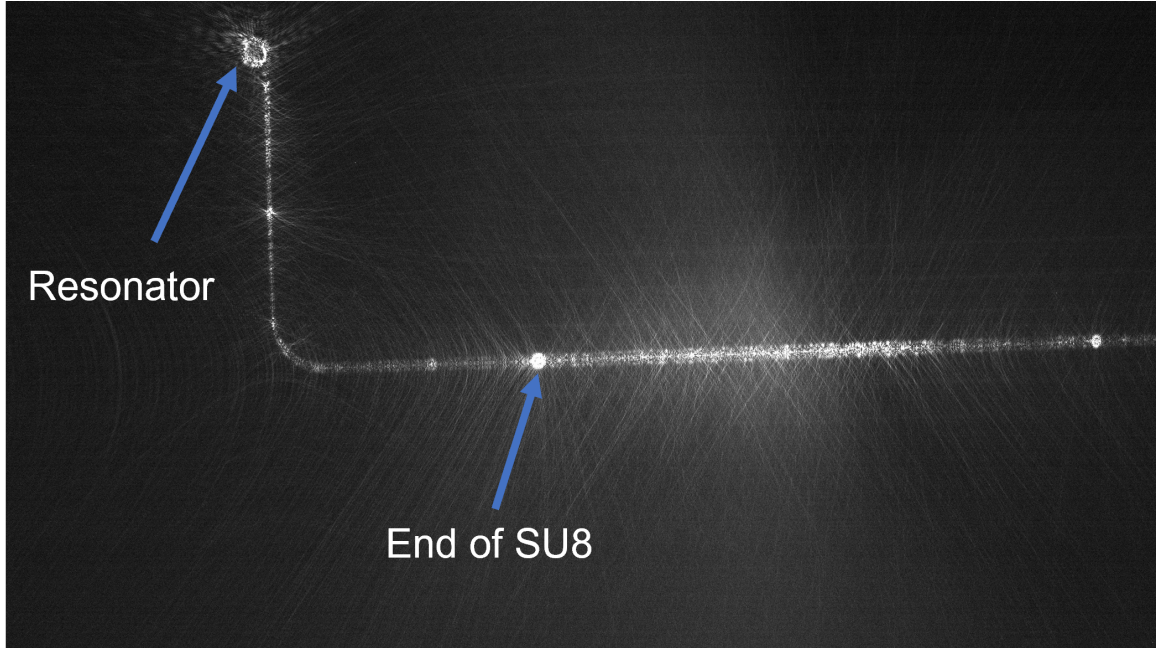
Figure 3.20: Image of the edge coupling chip when the alignment is finished. The laser is tuned to resonator resonance, and the microring resonator can be clearly seen with the scattering light. The bright spot in the middle is the end of the SU8 layer, where input light gets scattered. The end of the waveguide is not shown.

beginning to let the mode better convert into the waveguide.

To measure the coupling efficiency of this novel edge coupling strategy, we first characterized the waveguides without resonators to eliminate the effect of resonator-waveguide coupling. By measuring the input power and output power, we calculated the coupling efficiency of three waveguides. The end-to-end (two facets) efficiencies corrected for the input lens transmission (70%) and output lens transmission (75%) are:

Waveguide A: 10.2% (9.9 dB)

Waveguide B: 32.6% (4.9 dB)

Waveguide C: 26.3% (5.8 dB)

The LWD objective on the collecting side has a NA of 0.42, which is higher than the waveguide output NA of 0.32. Thus, the losses should mainly be the chip losses (facet reflection, SU8 transmission, etc.) and the coupling loss. For waveguide A, we noticed a strong scattering around the output SU8. It results from small cracks created during the cleaving
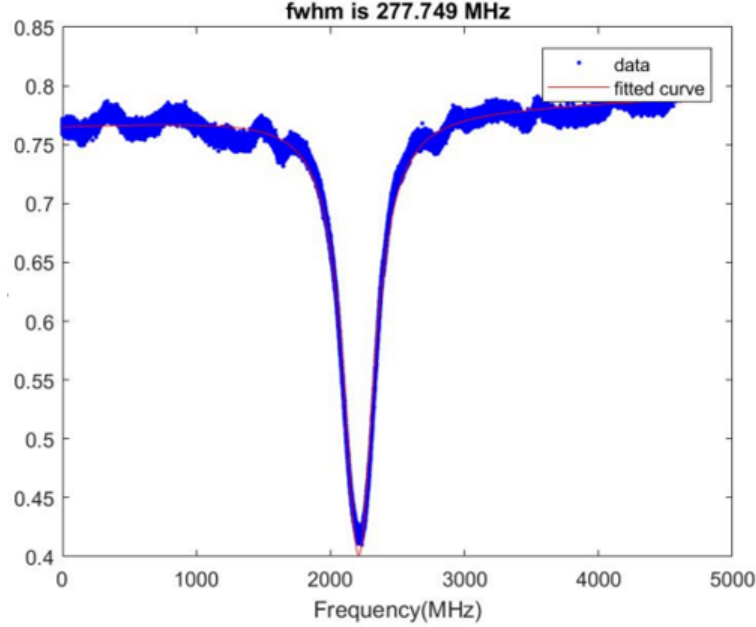
Figure 3.21: Measured resonance peaks of the resonator on edge coupling chip. The x-axis is the frequency change in MHz, and the y-axis is the voltage on the oscilloscope. The resonance peak has a FWHM of around 277 MHz, which corresponds to a quality factor of 1.38 million.

process, leading to lower efficiency. If we assume the input coupling facet has the same loss as the output facet, our non-defective waveguides (B and C) achieved more than 50% coupling efficiency for each facet. This coupling efficiency is much higher than normal grating couplers and is even slightly higher than the edge coupling with lensed fibers on U-grooves [86].

The waveguides with resonators are also characterized. A distributed Bragg reflector laser (DBR) is used to measure the quality factor of the resonators. DBR laser has a tiny cavity whose length can be easily tuned by temperature, which allows us to tune the frequency over 500GHz. One measured resonance peak is shown in Figure 3.21. A Lorentzian function is fitted to the data, and a FWHM of around 278 MHz is extracted. The calculated quality factor is around 1.38 million. This shows that our resonator is not severely affected by adapting the edge coupling approach.
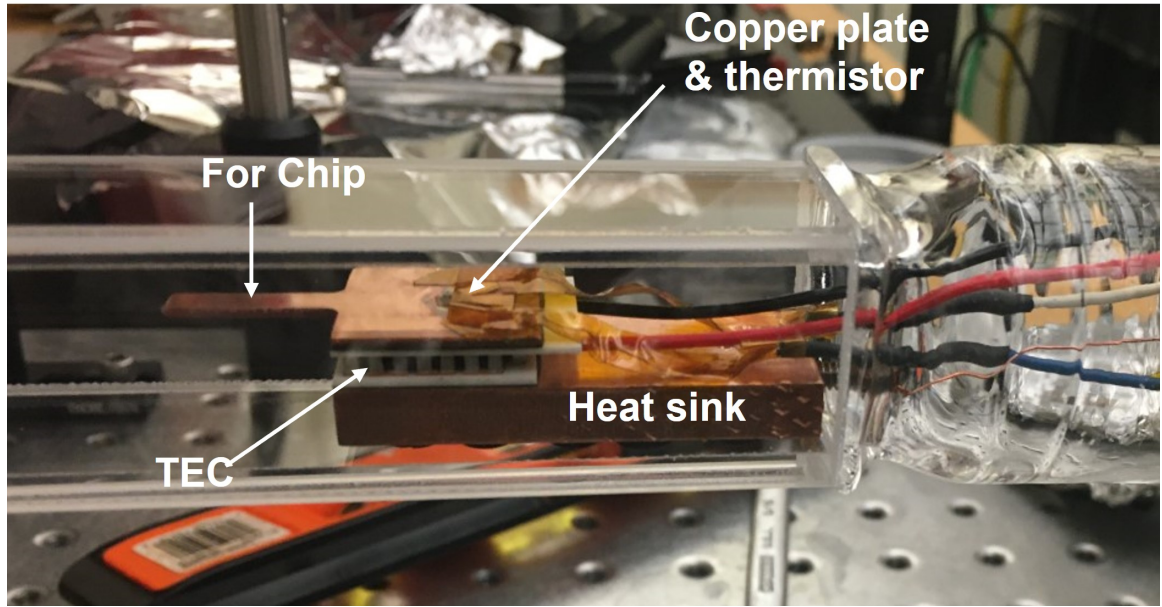
Figure 3.22: The vacuum setup to accommodate the edge coupling chip.

3.4.2 Integration in a glass vacuum chamber

We have demonstrated a highly efficient edge coupling strategy that can couple a free-space laser beam into the waveguide. The next step is putting the chip inside the vacuum and preparing it for further interaction with alkali atoms. The working distance of our LWD objective is 20mm. Thus, to focus our laser beam on the chip from the outside, the vacuum chamber we use needs to have optical access on the sides of the chip and within a distance of 20 mm. Our setup is shown in Figure 3.22. A cuboid glass vacuum chamber with an inner width of 1 inch is used. The distance from the chip to the outer chamber wall is less than 10 mm, allowing our edge coupling strategy. A cuboid copper heat sink is combined with a thermoelectric cooler (TEC) to control the temperature of the chip in order to thermally tune the resonance of the resonator to the transition line of rubidium. To ensure a good thermal conductivity between different components, a layer of sticky carbon conductive film (PELCO) is used between different components. Above the TEC, a customized thin copper plate is attached with the carbon film to transfer heat evenly into the chip. The extruded rectangular platform in the copper plate (see Figure 3.22) will hold

our edge coupling chip. The platform has a narrower width than the chip to expose the waveguide at the edge of the chip fully. A 10K thermistor is glued on this plate to monitor the temperature.

Our coupling strategy was successfully repeated with the chip inside the chamber, which proved its flexibility and high efficiency. Furthermore, thermal tuning of the resonance peak of the resonator to rubidium transition is also achieved by Linzhao Zhuo in our lab. Thus, we have demonstrated a versatile and highly efficient apparatus for the integration of nanophotonics and alkali atoms.

3.5 Slot resonator for thermal atoms

As we mentioned in the introduction, single atom cooperativity, the figure of merit for cavity QED system, is determined by:

$$C \propto \frac{Q}{V} \left| \frac{\epsilon_r E(\vec{r})}{\max(\epsilon_r E(\vec{r}))} \right|^2$$

To achieve large cooperativity, we need to maximize Q/V and direct the atoms toward the maximum electric field. In section 3.3, we have discussed the microring resonator and its interaction with atoms. A big limit for the microring resonator is that the maximum electric field is inside the SiN, and the atoms can only interact with the exponentially decaying evanescent field. This section will discuss a new slot resonator we designed that exposed the atoms to the maximum electric field. The goal is to combine our chip-scale thermal atomic beams with the slot resonator to achieve unprecedented cooperativity in an integrated nanophotonic platform.

The schematics for this novel slot resonator and its integration with our atomic channels are shown in Figure 3.23. The atomic channels are the silicon microchannels we have discussed in chapter two. The slot resonator is fabricated by using a double-layer SiN platform with a thin SiO$_2$ layer(see Figure 3.23(c)). The disk has a radius of 30μm, consisting of
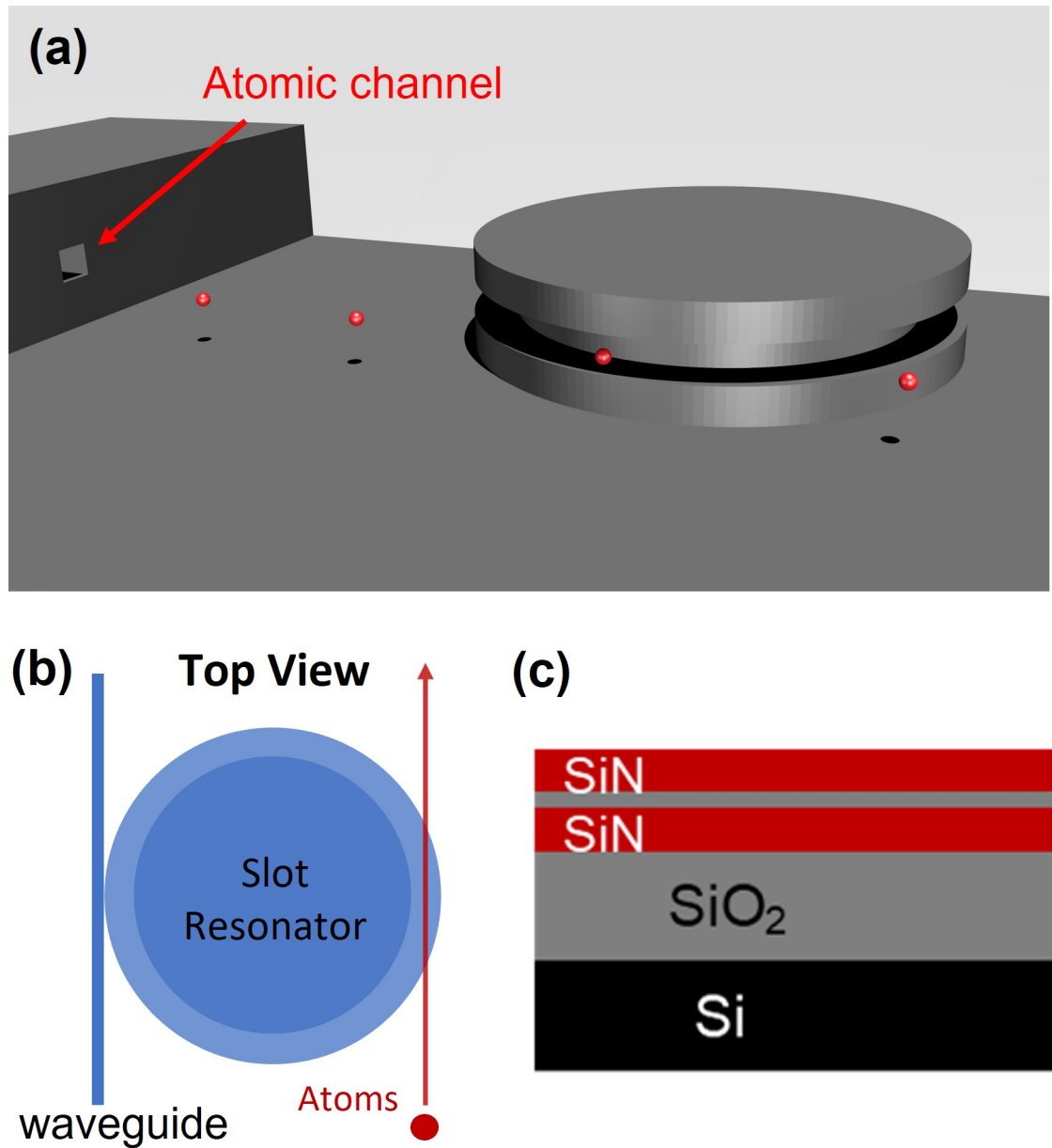
Figure 3.23: The schematics for novel slot resonator interacting with thermal atomic beams. (a) A rendered image of the 3D model of the slot resonator integrated with our atomic channels on the same chip. The red balls represent the atoms.(b) The top view schematic. The slot resonator is coupled with a waveguide, and the atoms transit through the air gap. (c) Schematic of the double-layer SiN platform to fabricate the slot resonator. The thin silicon dioxide layer between the two SiN layers will be partially undercut to create an air gap.

two SiN layers and a SiO$_2$ layer in between. The thickness of the SiN layer is 180 nm, and the thickness of the SiO$_2$ layer between them is 100 nm. The edge of the thin SiO$_2$ layer is partially etched 2.5 μm to create a 100 nm air gap for the atoms to transit. As shown in Figure 3.23(b), a waveguide is used to couple light into the slot resonator under the critical coupling condition, and the thermal atoms from our microchannels fly through the 100 nm air gaps of the resonator.

As we discussed in subsection 3.3.4, the TM mode expands more into the air compared with the TE mode, offering a stronger interaction strength. The TM mode profile of our slot resonator is shown in Figure 3.24 (a). Only the edge of our resonator (R =27 to 30 μm) is shown. The bottom of the resonator is set at $H = 0$, and the top is at $H = 460$ nm. A 2.5 μm thick SiO$_2$ layer occupies the area with $H < 0$. We can see that with our design, most of the electric field is concentrated in the air gap instead of the SiN layer, creating a smaller mode volume and also a higher g factor with the atoms. The calculated g factor at R =29.5 μm is shown in Figure 3.24 (b). Some sharp changes occur when crossing the interface between SiN and air, and between SiN and SiO$_2$, which result from the limited resolution (mesh size) used in making the plot. As expected, the highest g factor is now in the air gap with $g/2\pi = 371.5$ MHz at the center of the gap, providing a huge advantage over interactions reply on evanescent fields. The expected cooperativity with different quality factors is plotted in Figure 3.24 (c). Experimentally, our collaborator (Prof. Ali Adibi's group) has fabricated slot resonators with quality factors higher than 500 K, indicating a cooperativity value higher than 100. With these promising calculations, the next question is whether the atoms can successfully make transits through the 100 nm air gap. As we mentioned in the previous sections, the Casimir force dominates when atoms are very close to the dielectric surface (Equation 3.25). As a result, the effect of Casimir force must be carefully studied. Figure 3.25(a) shows the schematic side view of the experiment. Since the thickness of the bottom SiN layer is only 180 nm. First, the SiO$_2$ substrate between the resonator and the atomic channel (d') needs to be etched away ($\sim 1\mu m$), and only a
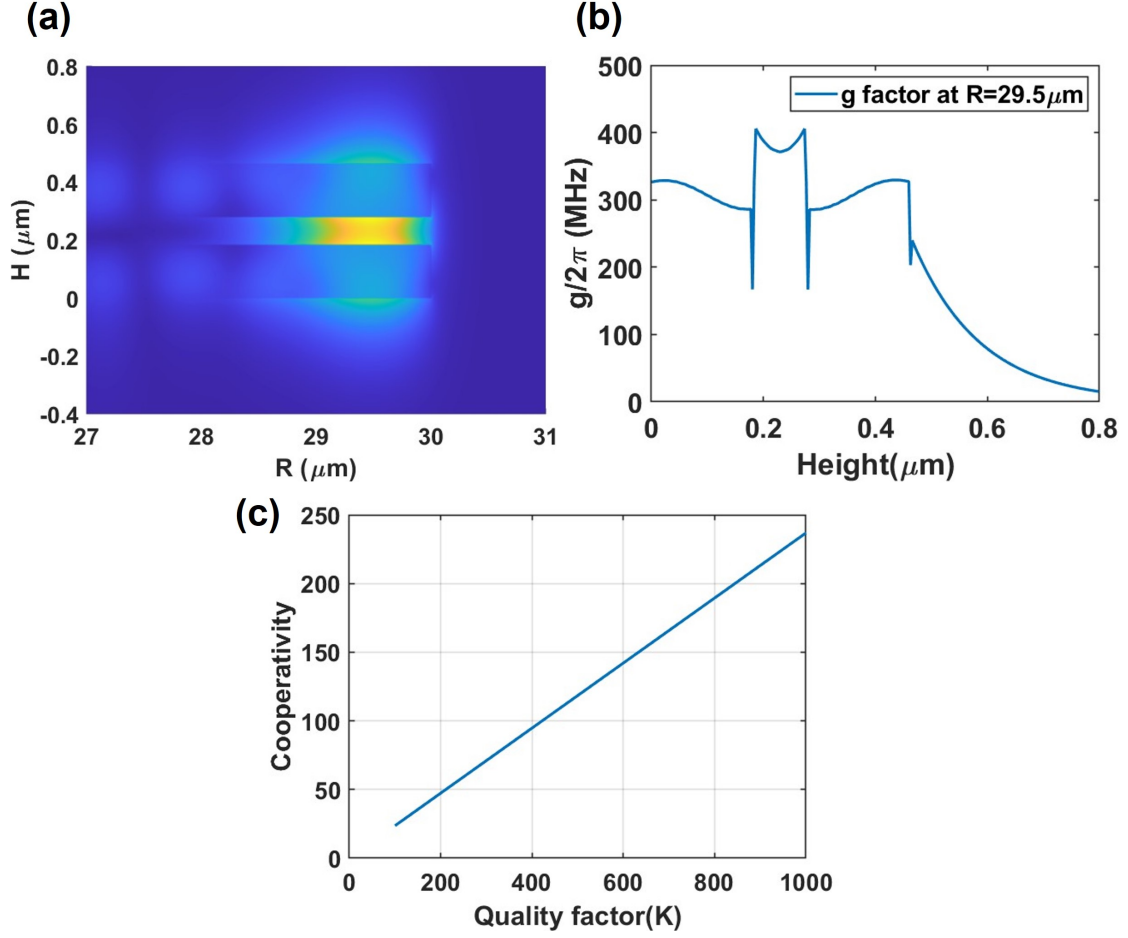
Figure 3.24: (a) The TM mode profile of our slot resonator with a radius of 30μm. The first SiN layer occupies $0 < H < 180$ nm, 180nm $< H < 280$ nm is the air gap with a width of 2.5 μm, and the top SiN layer occupies 280nm $< H < 460$ nm. (b) The calculated distribution of g factor at $R =29.5$ μm. The spikes result from the limited resolution across the boundary of SiN and air and have no further effect on our simulation. We can see that the highest g factor is inside the air gap and can be accessed by the atoms. (c) The expected single atom cooperativity with different quality factors.

small distance d remains. Otherwise, the atoms will be attracted to the chip surface before reaching the air gap. Second, when atoms are within the air gap, the Casimir forces from the top surface and bottom surface are in opposite directions, which helps the survival of the atoms. Figure 3.25(b) shows the atoms' trajectory with a distance of 30 to 70 nm from the surface of the bottom SiN layer. The atoms are initiated with a longitudinal speed of 300 m/s (the most probable speed of the thermal beam), and the vertical speed is randomly chosen to have a divergence angle of 0.4 mrad. Around 15% of the atoms hit the wall,
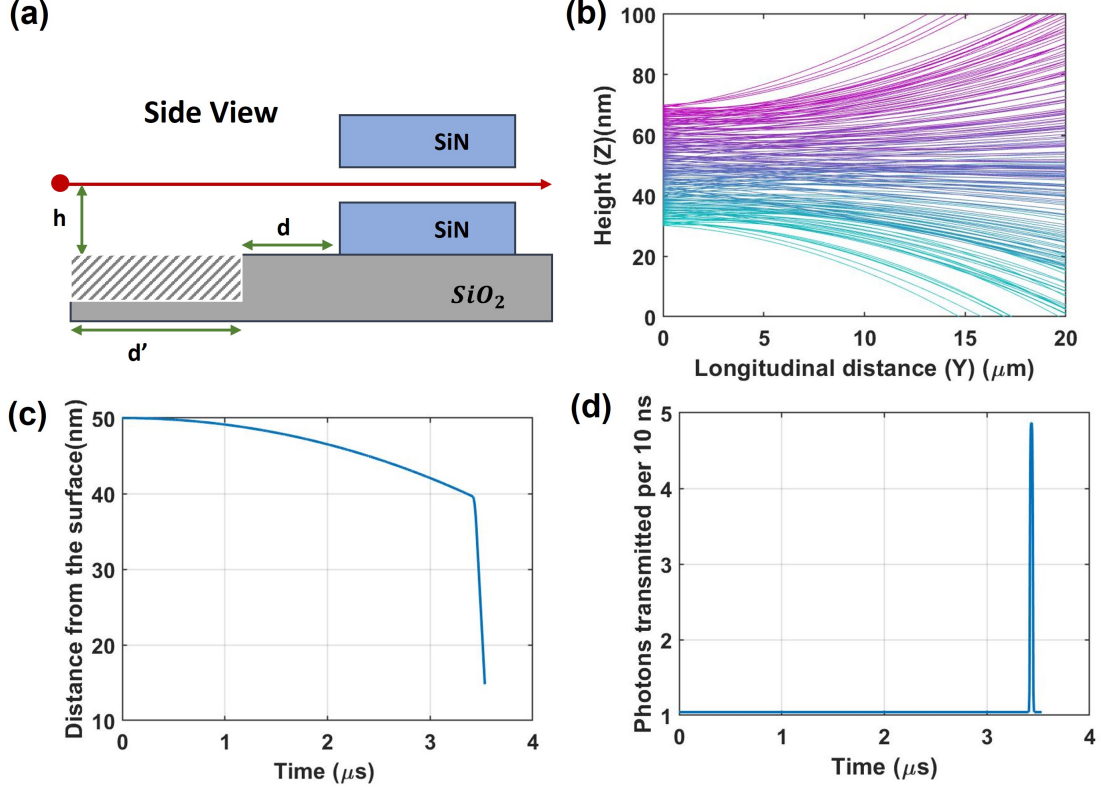
Figure 3.25: (a) The side view schematic of the experiment. The SiO_2 substrate between the resonator and the atomic channel (d') needs to be etched away to reduce the atom loss. The distance d is set to be smaller than 1 mm. (b) The trajectories of atoms inside the 100 nm air gap. The y-axis is the distance to the bottom SiN layer. The atoms have a longitudinal velocity of 300 m/s with a divergence angle of 0.4 mrad. (c) and (d) The simulated atom trajectory and transmission signal for $d = 1$ mm, quality factor 100 K, and input light power 500 pW. The y-axis in (c) is the height from the bottom SiN layer. The resonator is critically coupled with a 13dB extinction ratio.

demonstrating the feasibility of thermal atoms transiting the air gap. Figure 3.25(c) shows

the atom's trajectory when the remain distance $d = 1$ mm and Figure 3.25(d) shows the

simulated transmission signal. The methods for conducting the simulation are the same

as in the previous sections. The atom started with a longitudinal speed of 300 m/s and

zero vertical speed, with an initial height of 50 nm to the surface of the bottom SiN layer. It

reached the resonator at time 3.3 μs and was dragged downwards by the suddenly increased

Casimir force. The cavity's transmission was affected by the atom and showed a huge peak

in Figure 3.25(d).
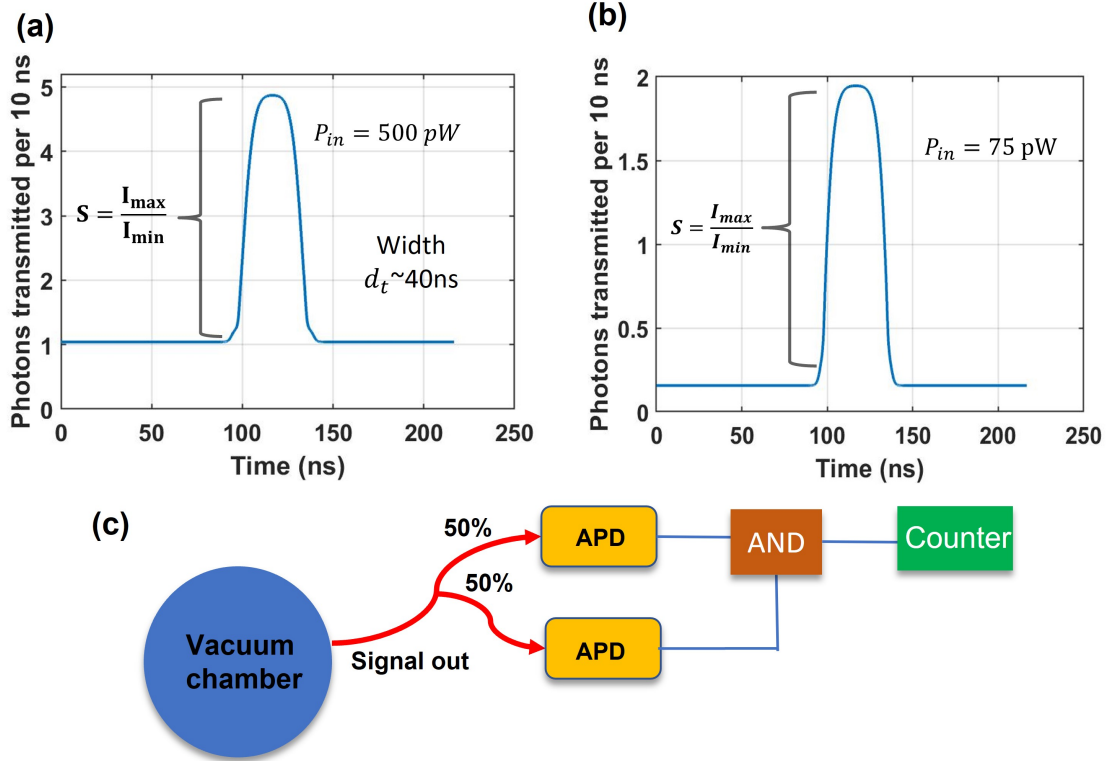
Figure 3.26: The transmission signal of atoms' transit with Q=100 K for the resonator. The resonator is critically coupled with a 13dB extinction ratio. (a) The atom transit signal with $P_{in} = 500$ pW. The signal-to-noise ratio (SNR) is around 5. (b) The atom transit signal with $P_{in} = 75$ pW. The SNR is increased to 12. (c) Coincidences detection setup. The transmission signal is split equally into two and directed into two single-photon avalanche photodiodes (APD). The output TTL signal of the APDs is combined into an AND logic gate to convert to coincident pulses, which are counted by a counter.

3.5.1   Signal detection and analysis

The high speed of thermal atoms combined with the small size of our microresonator makes the transit signal very hard to detect. Besides the theoretical expectation, the cooperativity needs to be measured experimentally and extracted from the experimental signal. As a result, the detection and analysis of the signal are crucial to this project.

A simulated transit signal is shown in Figure 3.26(a). The transit time d_t is only around 40 ns. With an input laser power $P_{in} = 500$ pW, the number of photons per transit is $\sim$20. With a 10% collecting efficiency, the number of collected photons per transit is only 2. In this case, the signal-to-noise ratio (SNR) is 5 but detecting a single transit is very hard. The

SNR is determined by the input laser power P_{in} and the quality factor (Q) of the resonator. A higher P_{in} or a lower Q will have a lower SNR. If we can have higher Q and collecting efficiency, we could use a higher P_{in} to have more photons per transit while maintaining the same SNR.

Single photon avalanche photodiodes (APD) have a dead time of 15 to 30 ns, making them unsuitable for detecting our signal, which consists of tens of photons in a 40 ns pulse. Silicon photomultiplier (SiPM) is a solid-state photodetector made of an array of thousands of integrated single-photon avalanche diodes on one common silicon substrate [90, 91]. For Q=1 million and an improved collecting efficiency of 40%, we can have 40 photons per transit with the same SNR of 5. SiPM is able to detect the single-transit signal, and its small size makes it easy to integrate with our nanophotonic platform. However, for the initial stage, where we have relatively low Q and low collecting efficiency, detecting the single transit is very challenging.

On the other hand, instead of trying to detect single transit, we can detect an average difference between the signal with and without atoms. In this regime, we can lower P_{in} to increase the SNR. As shown in Figure 3.26 (b), the SNR is increased from 5 to 12 when P_{in} is lowered from 500 pW to 75 pW. The ultimate SNR is limited by the extinction ratio of the critical coupling condition. A 13dB extinction ratio means 5% of the input light transmitting without an atom, resulting in a maximum SNR of 20. If we denote the averaged transit time to be d_t and the number of transits per second to be T, then the ratio between the averaged photon rate (R_{with}) with atom and the averaged signal without atoms $R_{without}$ is

$$\frac{R_{with}}{R_{without}} = 1 + (S - 1) \cdot d_t T \tag{3.29}$$

In which S is the SNR.

Based on an atomic source with a brightness of 1.9×10^{15} atoms/s/sr/mm^2 and assuming atoms pass through the region defined in Figure 3.25(b), we expect to have $T \approx 10^4$. With the maximum $S = 20$ and averaged d_t=40 ns, we can calculate the ratio to be 1.0076. The

ratio is so close to one that it is very hard to detect.

Instead, we came up with a novel coincidence detection method to enlarge the difference. The setup is shown in Figure 3.26(c). The transmission signal is split 50/50 into two single-photon avalanche photodiodes in Geiger mode. The output TTL signal is sent into a logic AND gate and a counter to count the coincidences with zero time delay. For a stream of photons following Poisson distribution, the two-photon coincidence rate equals

$$C = R^2\tau \tag{3.30}$$

Where τ is the size of the time bin to determine coincidences. The two-photon coincidence rate is proportional to the square of photon rates. Thus the difference between the signals with and without atoms can be amplified.

When there is no atom, the coincidences rate is $R^2_{with}\tau$. The coincidences rate with atoms at zero time delay is $R^2_{with}\tau + (S^2 - 1)R^2\tau \cdot d_t T$. Thus, we can get the coincidence rate ratio N_c:

$$N_c = 1 + (S^2 - 1)d_t T \tag{3.31}$$

For S=20, we can have N_c=1.16, which is very feasible to detect.

After detecting a difference in signal with/without atoms, the next step is to find a way to extract the cooperativity from the data. We could, in principle, extract cooperativity from N_c. However, N_c can be easily affected by the average transit time and the number of transits per second. These two values are hard to estimate independently when the single transit can not be measured. However, the simulations we did are under the condition that cavity resonance frequency, atom resonance frequency, and the input laser frequency are the same. We could scan the input laser's frequency and measure a spectrum to gain more information from the system. Figure 3.27 shows the calculated cavity transmission, SNR, and N_c with different input laser frequency. The cavity resonance and the atom resonance are kept at the same frequency, and the input laser frequency is detuned away by f. The
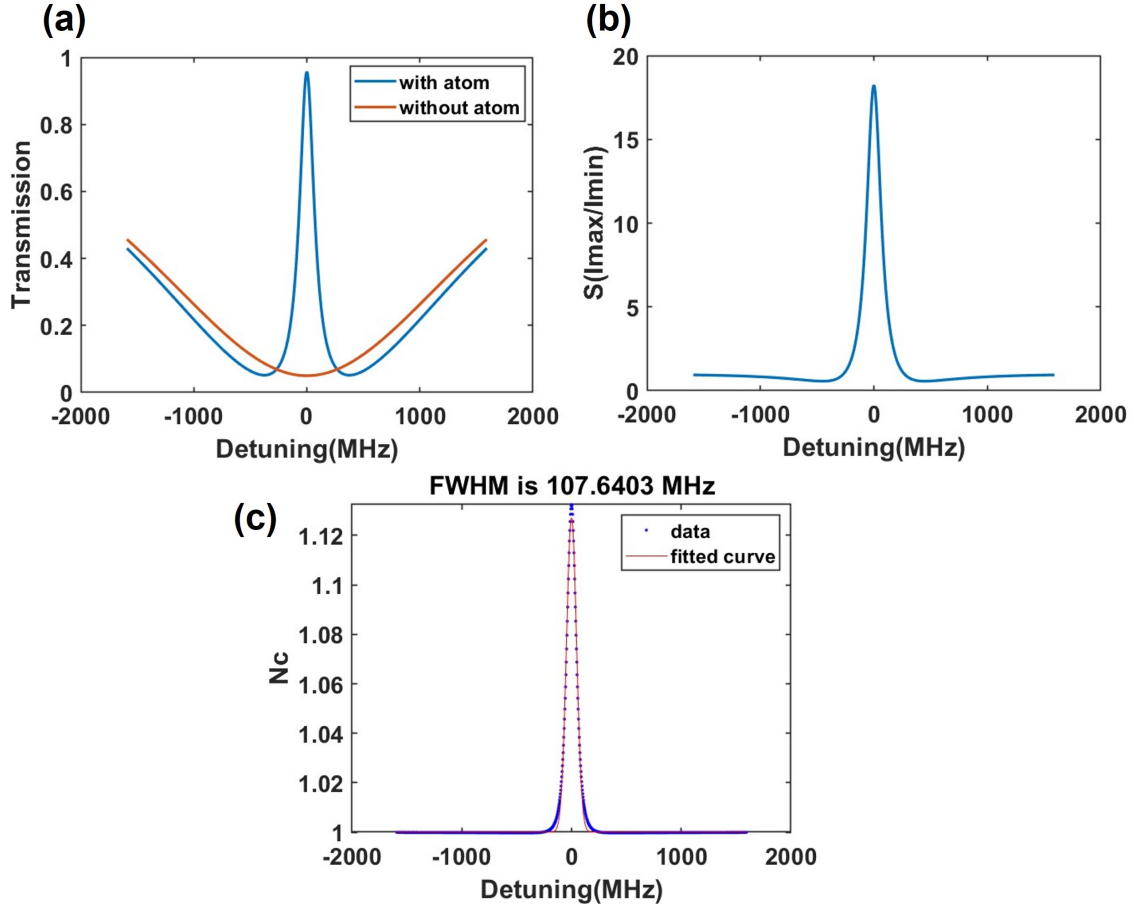
Figure 3.27: The proposed coincidences method to measure the cooperativity experimentally. Resonator Q=100 K, input laser power P_{in}=7.5 pW. The resonator is critically coupled with a 13dB extinction ratio. (a) The transmission spectrum with different detuning of the input laser relative to the cavity resonance. The blue line is the spectrum with an atom, and the red line is without an atom. (b) The SNR with different detuning of the input laser. (c) The calculated coincidence ratio N_c with different detuning of the input laser. The FWHM is extracted by fitting the curve with a Gaussian function.

slot resonator has a Q=100 K, and the input laser power P_{in}=7.5 pW. We can calculate the $SNR(f)$ from the resonator transmission in Figure 3.27(a). Then, by using Equation 3.31, we can calculated $N_c(f)$. Figure 3.27(c) shows our calculated $N_c(f)$, which is fitted by a Gaussian function to extract the FWHM. The FWHM is more robust and will not be affected by the height of the peak. In fact, after confirming with simulations, the FWHM is only a function of the resonator quality factor Q, g factor, and the input laser power P_{in}

$$\text{FWHM}(g, Q, P_{in}) \tag{3.32}$$

The quality factor of the resonator and the input laser power can be measured independently and accurately. The FWHM is an increasing function of g. As a result, we can determine the g factor after measuring $N_c(f)$ and its FWHM. Then, Equation 3.22 can be used to get an experimental cooperativity value.

This section demonstrated our study in utilizing a novel slot resonator to achieve unprecedented cooperativity on a chip-scale platform. Many crucial aspects of the project are considered, including Casimir force, detection methods, and cooperativity extraction. Prof. Ali Adibi's group has made impressive progress in making slot resonators with great quality factors (>500 K) and on-chip filters to reduce the rubidium contamination on resonators. More efforts are being devoted to experimentally observing significantly high cooperativity.

CHAPTER 4

SINGLE ATOMS IN MINIATURE ATOMIC BEAMS

Isolating, manipulating, and observing a single quantum system is the foundation for numerous quantum applications and fundamental research. In recent years there has been a surge of interest in room-temperature atomic vapors for applications in quantum information science. Photon pairs generated using four-wave mixing [92, 93, 94], quantum memories [95, 96] and single photon source [97] have been achieved with thermal atoms in vapor cells. In contrast to laser-cooled samples, thermal vapors are straightforward to generate, highly scalable, and can be operated continuously. The latter is especially important for achieving high data rates in quantum communications and state transfer. One can define two broad thrusts to this research. One approach is "top-down" and seeks to engineer collective quantum behavior in one or a few modes of interest within the vapor while ignoring the discrete nature of the constituent particles (atoms). This approach is typical of four-wave mixing experiments [92, 94, 98, 95]. An analogy is the collective excitation spectrum of quantum degenerate gases where phonons and magnons replace individual atoms as the relevant degrees of freedom [99, 100, 101]. In a second, "bottom-up" approach, one constructs a complex quantum system using individual atoms as building blocks. This approach has been followed for laser-cooled atoms in optical tweezer arrays [102, 8], and trapped ion systems [103, 104]. For thermal atomic vapors, this bottom-up approach has thus far been quite undeveloped due in part to the rapid and random thermal motion of the atoms that makes it difficult to track them. If one could utilize single atoms in the thermal vapor, the possibilities are clearly enormous–a typical rubidium vapor cell at $100\,^{\circ}C$ contains $O(10^9)$ completely indistinguishable quantum systems within a $1\,\mathrm{mm}^3$ volume. Even a small fraction of such a large ensemble constitutes a huge and readily available resource for quantum information if it can be harnessed.

In an atomic beam, the arrival of the atoms follows the Poisson distribution. By tuning the vapor pressure, we can make the probability of having one atom in the field of view much larger than having more than one atom. In this way, we can make sure that the single-atom effect dominates. Another advantage of atomic beams is that atoms move in a well-defined direction. Thus, we can also interact with the atom upstream, selecting the slow atoms and manipulating their quantum states. As a result, we utilized the chip-scale atomic beams to demonstrate the feasibility of such a "bottom-up" approach to quantum information science with near-room-temperature thermal vapors.

This chapter will first discuss the photon time tagging system we built and tested, which is the foundation for many quantum optics applications. Then, we experimentally isolated a sub-ensemble of atoms whose three-dimensional velocity vector is 20 times smaller in magnitude than the mean. The transit time through a field of view of size 25 μm has been extended by a similar factor to 1 μs. Moreover, the direction of motion is the same for all atoms in the sub-ensemble. We use this feature to demonstrate tracking of single atoms across two detecting regions, with no obvious limit to the tracking ability. While the approach is highly selective, we nonetheless still observe a sizeable number of such atoms and suppress the large, unwanted background consisting of fast-moving atoms. As a first step to constructing bottom-up thermal quantum systems, we observed quantum-mechanical antibunching and the correlated photons from a single atom for as long as 1 μs, thus demonstrating that the coherence time is limited by the transit time. We also observed large values of the second order coherence $g^{(2)}(\tau)$ and third-order coherence $g^{(3)}(\tau_1, \tau_2)$. This indicates its potential to be a simple source of photon pairs or triplets for quantum applications.

4.1 Photon time-tagging system

This section will discuss in detail how we built the photon detection and time-tagging system from scratch. We hope the information provided can be helpful for researchers who

are interested in building their own system.

The first element of a photon detection system is the detector. We used the single photon counting modules (SPCM) from Excelitas Technologies. We have one free space module (SPCM-AQRH-15) and a fiber-coupled module (SPCM-AQRH-15-FC), allowing us to do coincidences measurements. The SPCMs we used are silicon avalanche photodiodes operated in Geiger mode. The absorption of the photon on the active area of the SPCM triggers an avalanche process, after which a TTL level pulse (~ 2.2 V) will be generated. Figure 4.1 (c) shows the characteristics of the generated TTL signal. The output pulse has a width of around 15 ns. The dead time of the device is around 30 ns, which leads to a maximum count rate of around 30 million/s. The quantum efficiency of the detector is around 65% at 780 nm. The timing resolution is 350 ps, which is sufficient for our applications. The free space SPCM is mounted on a 1D translational stage, and the light from the fiber is focused by an aspheric lens and aligned to the SPCM's active area. The translational stage and the mount for the aspheric lens can be tuned to optimize the collecting efficiency.

With the detectors, the next step is to count and time-tag the photons. Counting the photons can provide intensity information about the signal, making the SPCM a very sensitive intensity detector. However, the temporal information about the photons is also very valuable and sometimes crucial in quantum optics and other fields involving temporal dynamics. For our application in measuring the dynamics of rubidium atoms, an accuracy of at least 1 ns level is needed. As we have shown about the characteristics of our SPCM, the photon pulses are short (15 ns) and can have high count rates (30 M/s), making accurate time-tagging a challenging task. Commercial time-tagging devices for doing photon correlations are extremely expensive. For example, a two-channel time tagging device quoted $12500 from Becker-Hickl and $12000 from PicoQuant in 2019.

To save our hard-earned research funding, we first tried building a time-tagging device with microcontrollers. The capabilities of a very fast microcontroller board called Teensy were tested. We bought a Teensy 4.0, which has a 600 MHz processor (ARM Cortex-
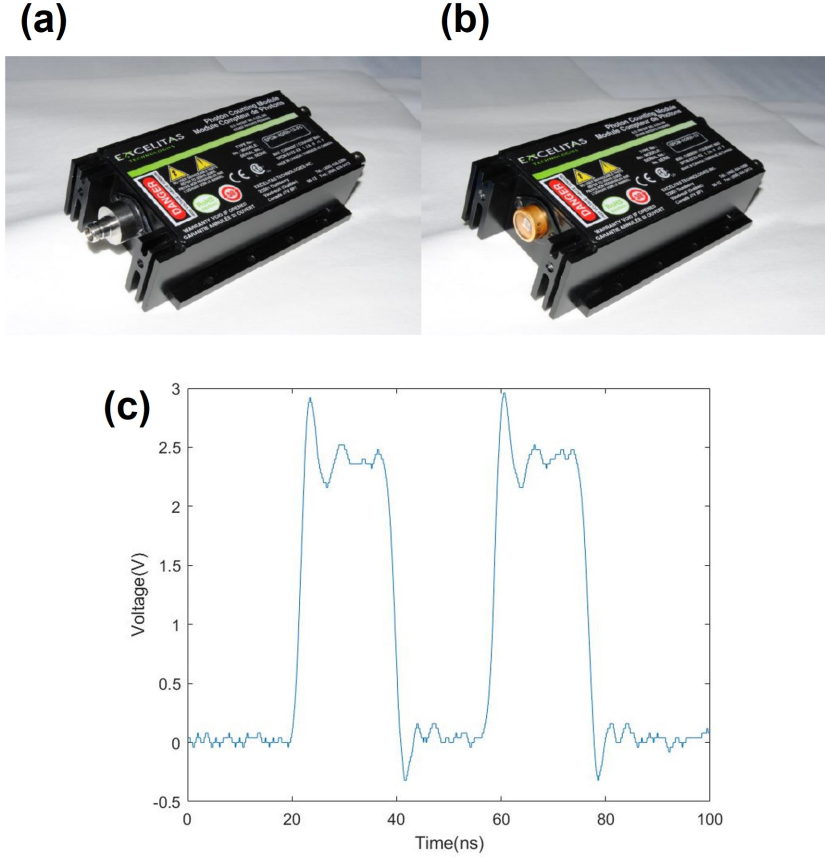
Figure 4.1: (a) and (b) are pictures of the fiber-coupled SPCM and free space SPCM, respectively. (c) The TTL signal from our SPCM, measured by a 200 MHz bandwidth oscilloscope. The width of each pulse is around 15 ns.

M7) and only cost $25. The output of a function generator (Keysight 33220A) is used to create short TTL pulses to test the device's pulse counting and time tagging accuracy. The teensy card was tested to be able to count accurately up to 20 MHz, which makes it a good low-cost counter. As for the time tagging, we wrote codes to access the CPU clock. By counting the number of CPU oscillations between each TTL signal, we can calculate the time interval between photons. The maximum frequency the Teensy can time tag is found to be $\sim$3 MHz. Figure 4.2 shows a histogram of the time intervals with a 2 MHz pulse input. We can see that many of the time intervals are $\pm$10 ns away from the expected 500 ns value, showing that it does not meet our accuracy requirement. However, this Teensy microcontroller can be used as a good counter and a time-tagging device for experiments
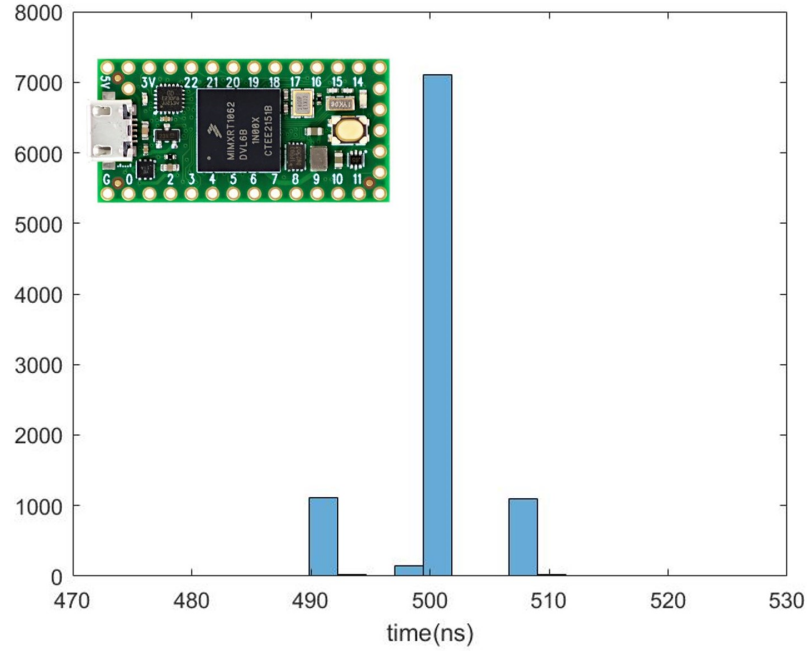
Figure 4.2: The histogram of pulse intervals from the Teensy. The input is 2 MHz pulses from the function generator. The inset is a picture of the Teensy microcontroller. The maximum frequency the Teensy can time tag is 3 MHz.

that have dynamics in the microsecond time scale.

We then tested a demo unit from PicoQuant (PicoHarp 300). PicoHarp 300 is a standalone Time-Correlated Single Photon Counting (TCSPC) system that can be connected to a PC through a USB interface. The time tagging accuracy is tested with 4 MHz TTL pulses generated by the same function generator. The histogram of time intervals is shown in Figure 4.3. The function generator we used (Keysight 33220A) has a time error of around 10 ps with the 4 MHz frequency, which is sufficient for this test. We can see that this commercial device has an accuracy of ± 1 ns. In Figure 4.3, 4 million time tags are generated, and 27 intervals with a time of 500 ns are not shown in the figure. The 500 ns interval indicated that the device has a small probability of missing one pulse, causing a double-size interval. During the testing of this commercial device, we found that most of the price we paid might result from the fancy user interface and other integrated functions designed for life science and lifetime fluorescence measurements. Actually, all the functions can be calculated once

90

Figure 4.3: The histogram of pulse intervals from the PicoHarp 300. The input is 4 MHz pulses from the function generator. There are 4 million time tags in total. The inset is a picture of the PicoHarp 300. The maximum frequency the PicoHarp 300 can time tag is around 4.5 MHz.

we have the accurate time tags of the input pulses. We found a Time Interval Analyzer (Guidetech GT668) with two independent channels that should satisfy our requirements. The GT668 is an electronic card with a PCIe interface for desktops. It is a less expensive (~\$5000) and more basic level instrument, which only provides a python library to allow customized coding. We wrote python codes to do time tagging and save the data to the hard disk continuously. The testing result with the same function generator is shown in Figure 4.4. The accuracy of the card is ± 50 ps, which is much better than the \$20000 PicoHarp 300. Furthermore, unlike the PicoHarp, no pulses are missed during the tests. To test whether the two channels are independent and time-synchronized, we connected the output of the function generator parallel with the two channels of the card with BNC cables of the same length. Thus, for each pulse, they should register the same time tag. Among 2 million pulses, the maximum time difference between channel 1 and channel 2 for the same pulse is 0.3 ns, and the minimum is 0.23 ns. The slight offset from the 0 ns might
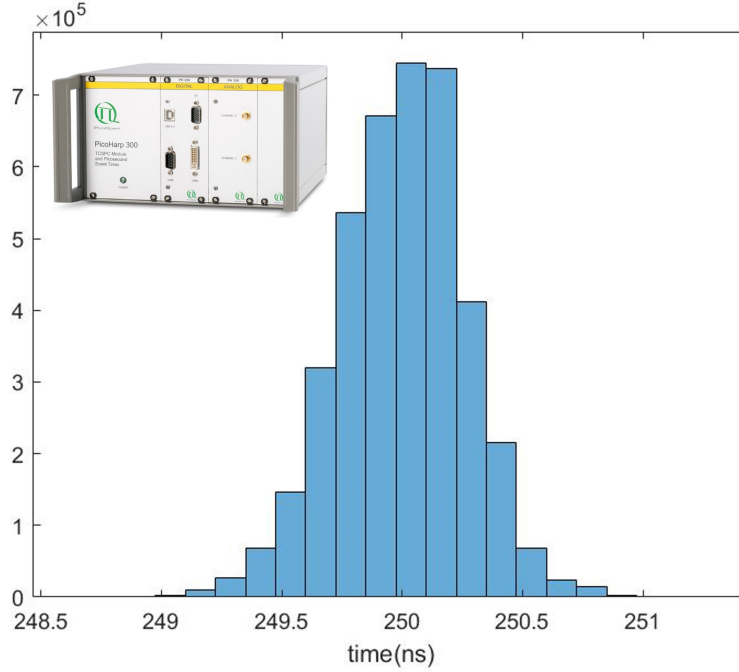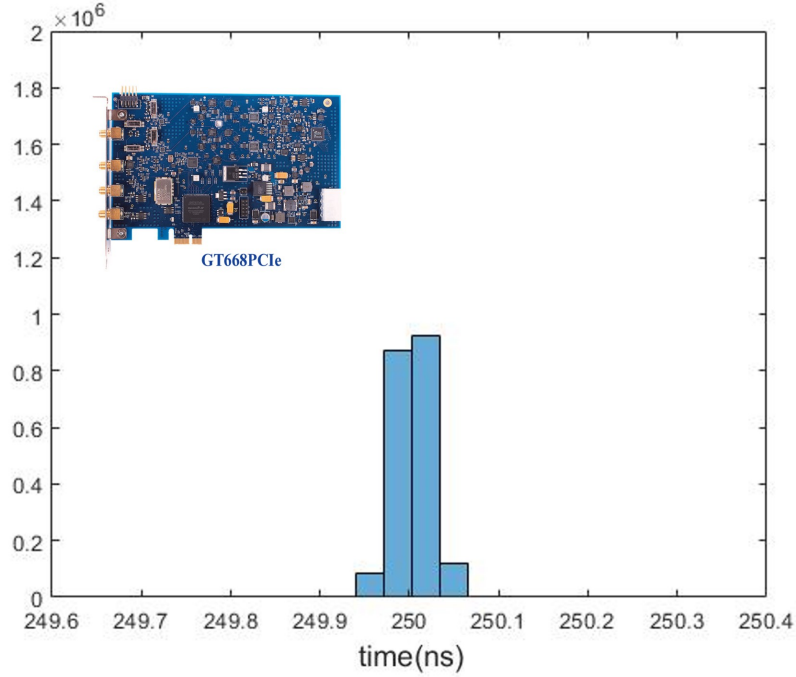
Figure 4.4: The histogram of pulse intervals from the Guidetech GT668. The input is 4 MHz pulses from the function generator. There are 2 million time tags in total. The inset is a picture of the GT668. The GT668 can make measurements up to 4 million times per second.

result from the non-perfect BNC cable matching or the delays within the card. However, even if all the errors are attributed to the card, the accuracy across the two channels is sufficient for our application (we need ± 1 ns). The code was optimized to allow basically unlimited data taking. The card has been used to take 100 million time tags and over 10 hours continuously in an experiment. Later, we purchased and tested another time interval analyzer (Carmel instrument NK732). This card has a PXIe interface, which is required to be installed on a PXIe chassis and connected to a PC with a Thunderbolt port. The price of the card is also around $5000, but it can make 20 million measurements per second, 4 times higher than GT668. The accuracy and continuous data-taking capability are similar to the GT668. However, the coding part is harder because of the C# language it uses and the lack of documentation.

In summary, we have explored different approaches to achieve photon time tagging. A cost-efficient and extremely accurate approach using the time interval analyzer cards is

demonstrated. Since we control the cards with basic codes, we have the flexibility to add as many functions as we want. For example, the photon count rates of two channels can be printed to the monitor every second for alignment and fine-tuning.

4.2 Second-order correlation function

With our amazing two-channel photon time-tagging system, we have the ability to conduct research in many fields of quantum optics. One of the examples is the measurement of the second-order correlation function.

The normalized first-order coherence $g^{(1)}(\tau) = \frac{\langle E^*(t)E(t+\tau)\rangle}{\langle E*(t)E(t)\rangle}$ is useful for quantifying the coherence between two electric fields, as measured in a Michelson or other linear optical interferometer. The second-order coherence measures the intensity correlation instead and is naturally suited to study photon statistics. The degree of second-order coherence, also called the second-order correlation function, is the normalized form of the intensity correlation. It is defined as

$$g^{(2)}(\tau) = \frac{\langle E^*(t)E^*(t+\tau)E(t+\tau)E(t)\rangle}{\langle E^*(t)E(t)\rangle^2} \tag{4.1}$$

Since the intensity is proportional to the number of photons, this $g^{(2)}(\tau)$ describes how photons are correlated in time.

A good reference is that for photons following Poisson distribution, $g^{(2)}(\tau) = 1$. With a Poisson distribution (process), photons are independent of each other and will randomly arrive at Δt with a fixed probability. With this reference, $g^{(2)}(\tau) > 1$ means photons are more likely to be together (bunching), and $g^{(2)}(\tau) < 1$ means photons are less likely to be together (antibunching). For the laser light, photons follow Poisson distribution, and $g^{(2)}(\tau) = 1$. For classical light, by using the Cauchy–Schwarz inequality, we can get the following conditions: $g^{(2)}(0) \geq 1$ and $g^{(2)}(0) \geq g^{(2)}(\tau)$ [43]. Violating these two conditions indicates a unique quantum photon source. The second-order correlation
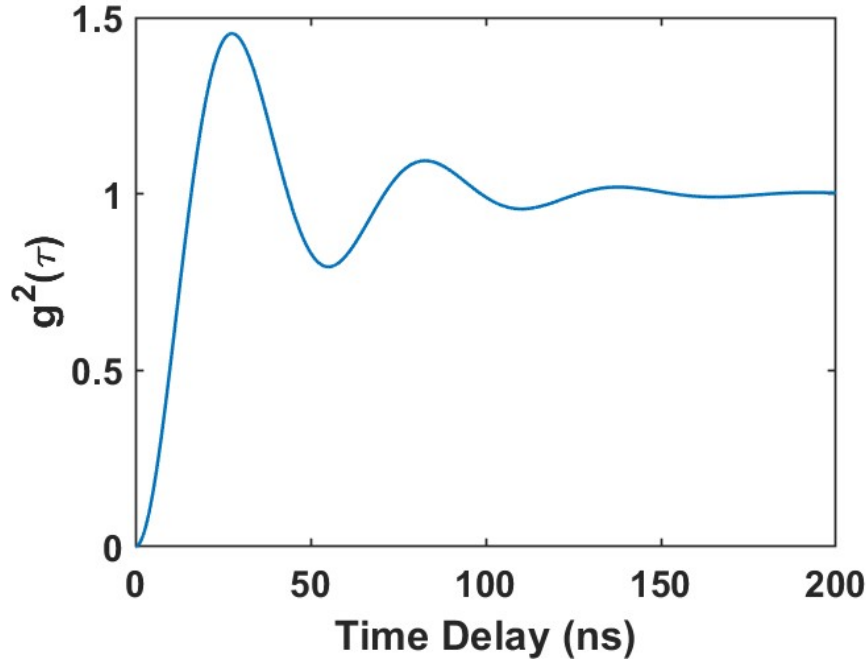
Figure 4.5: The second-order coherence function of a single rubidium atom with Rabi frequency equals 3Γ. Γ=6.06 MHz.

function for a single rubidium atom is plotted in Figure 4.5. In Figure 4.5, the dip near $t = 0$ is called antibunching, which happens when we only have one quantum emitter. Because for a single emitter like an atom, after emitting a photon, it needs time to be re-excited and release another photon. Thus, the probability of having two photons with zero time delay is zero. $g^{(2)}(\tau) \to 1$ when the time delay is larger means the temporal correlation between photons is quickly lost [43].

All single-photon detectors have dead time, and the dead time for our SPCM is ∼30 ns. In order to overcome the dead time limit and measure the full range of $g^{(2)}(\tau)$ versus time, two SPCMs are set up in Hanbury-Brown–Twiss configuration (see Figure 4.6 (a)). The signal in a multimode fiber is split 50/50 by a 1×2 multimode fiber coupler (TM105R5F1B), and each end is connected to a SPCM. The outputs of two SPCMs are connected to our card for time tagging. With this configuration, there is no dead time between channels, and two photons with zero time delay can be detected with a 50% chance. One thing that needs to be taken care of is the afterglow or breakdown flash effect of the silicon avalanche

photodiodes [105]. As we mentioned before, our SPCM is a silicon avalanche photodiode (APD) in Geiger mode. The avalanche event of charge carriers in silicon is accompanied by broadband photon emission [106]. The spectrum of the breakdown flash is shown in Figure 4.6 (c). Each signal photon can create a breakdown flash event which consists of tens of photons. Under the Hanbury-Brown–Twiss configuration, these artificial photons can cause cross-talk between two SPCMs and create fake correlation coincidences. We found that using two fiber-coupled SPCMs will have these fake correlations, which will undermine the accuracy of $g^{(2)}$ measurements (especially for very weak signals). Our solution is to use one free-space SPCM and one fiber-coupled SPCM. Then, a high-performance laser line Filter (Edmund #64-256) is added in front of the free-space SPCM to filter out most of the breakdown flash photons. As shown in Figure 4.6 (b), the filter is added between the mount for the aspheric lens and SPCM. Since the photons in breakdown flash are broadband and scattered in all directions, this solution is proven to work well (see Figure 4.7).

In the Hanbury-Brown–Twiss configuration, the second-order correlation function can be written as the intensity correlation of two detectors:

$$g^{(2)}(\tau) = \frac{\langle I_A(t) I_B(t+\tau) \rangle}{\langle I_A(t) \rangle \langle I_B(t+\tau) \rangle} \tag{4.2}$$

To experimentally calculate this value, we need to express $g^{(2)}(\tau)$ in terms of the photons measured by SPCM A and SPCM B. We can utilize the following relations:

$$
\begin{aligned}
I_A(t) &\propto \frac{n_A(t, \Delta t)}{\Delta t} \\
\langle I_A(t) \rangle &= \frac{\int_0^T I_A(t) \Delta t}{T}
\end{aligned}
\tag{4.3}
$$

Where Δt is the size of the time bin, $n_A(t, \Delta t)$ is the number of photons in the time bin at
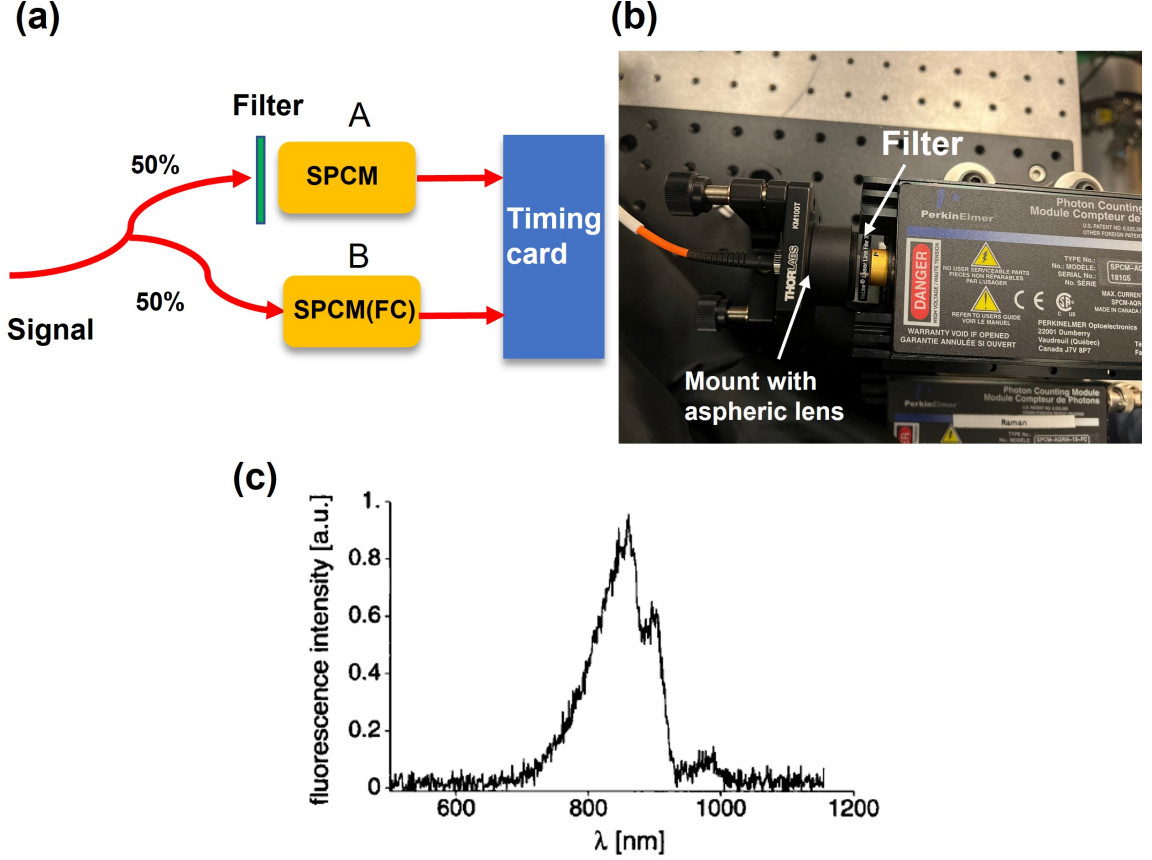
Figure 4.6: (a) The schematic for our Hanbury-Brown–Twiss set up for measuring the $g^{(2)}$ function. One free space SPCM and a fiber-coupled SPCM are used with a 50/50 fiber splitter. A narrow bandwidth filter is added in front of the fee space SPCM to remove the breakdown flash photons. (b) A picture of the free space SPCM setup. The signal from the input fiber is focused on the active area of the SPCM by an aspheric lens. The filter is fixed on a post with double-sided tape and inserted between the mount and the SPCM. (c) Normalized breakdown flash spectrum of the silicon avalanche photodiode from Ref [105].

t, and T is the duration of the experiment. Then we have

$$
\langle I_A(t) I_B(t+\tau) \rangle = \frac{\int_0^{T-\tau} \frac{n_A(t,\Delta t)}{\Delta t} \cdot \frac{n_B(t,\Delta t)}{\Delta t} \Delta t}{T-\tau}
$$

$$
= \frac{\int_0^{T-\tau} n_A(t, \Delta t) n_B(t+\tau, \Delta t)}{(T-\tau)\Delta t} \tag{4.4}
$$

Putting Equation 4.3 and Equation 4.4 into Equation 4.2, we get

$$
g^{(2)}(\tau) = \frac{n_{AB}(\tau) \cdot (T-\tau)}{n_A(t < T-\tau) n_B(t > \tau) \cdot \Delta t} \tag{4.5}
$$

96
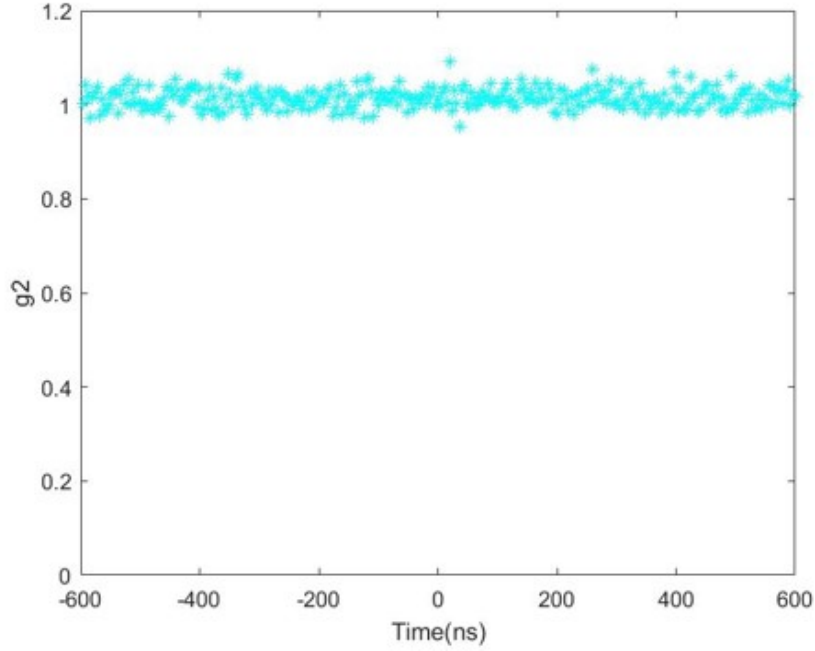
Figure 4.7: The calculated $g^{(2)}(\tau)$ with measured photons from laser scattering light. The data agree with the expectation that $g^{(2)}(\tau) = 1$.

Where $n_{AB}(\tau) = \int_0^{T-\tau} n_A(t, \Delta t) n_B(t + \tau, \Delta t)$ is the coincidences with time delay τ cumulated over the experiment duration T, n_A, n_B is the total number of photons from SPCM A and SPCM B. Usually $T \gg \tau$, and we can write

$$g^{(2)}(\tau) = \frac{n_{AB}(\tau)/T}{n_A/T \cdot n_B/T \cdot \Delta t} \tag{4.6}$$

In this equation, the numerator is the coincidence rate with different time delays, the denominator is the coincidence rate generated by random Poisson distributions (which is sometimes called accidental coincidence rate). Thus, the physical meaning of $g^{(2)}(\tau)$ is the coincidence rate $n_{AB}(\tau)/T$ normalized by the accidental coincidence rate. While these two coincidence rates depend on the losses of the measuring systems, the value of $g^{(2)}(\tau)$ is independent of system losses, allowing us to robustly measure the temporal coherence of photons. To calculate $n_{AB}(\tau)$, we need to iterate through time tags in one channel and find the number of corresponding coincidences in the other channel. A naive algorithm

97

of iterating each pair of photons has a time complexity of $O(n_A n_B)$, which is too slow for millions of photons. A time-efficient algorithm inspired by Ref [107] is implemented in Matlab to calculate $n_{AB}(\tau)$. It utilized the property that the time tags are naturally in ascending order within each channel and only need $O(n_A M)$ time to finish, where M is the number of needed time bins ($\sim$100). With $n_{AB}(\tau)$, $g^{(2)}(\tau)$ can easily be calculated by using Equation 4.5. To test the algorithm and our setup, we measured the scattering photons from a laser beam. Figure 4.7 shows the calculated $g^{(2)}(\tau)$. We can notice that $g^{(2)}(\tau) = 1$ for all the time delays in the plot, which agrees with the theory. The cross talks are also eliminated by the extra filter. The fluctuations in $g^{(2)}(\tau)$ will be smaller when more time tags are accumulated. This property makes the photon correlation a very powerful approach for measuring very weak signals through long-time averaging, and our experiments later will demonstrate this claim.

4.3 Vacuum setup

The 3D model of the chamber we used is shown in Figure 4.8. The main cuboid glass section is attached to vacuum flanges with bellows in between to reduce stress. The glass section is a 12 mm $\times$ 12 mm $\times$ 42 mm cuboid glass cell, offering great optical access. Both sides of the glass section are attached to vacuum flanges with bellows in between to reduce stress. The right venting port is connected to a pumping station to maintain a pressure of 10^{-7} Torr. The left port is connected to a three-way cross, in which one way is used to insert the atomic oven. The other way is also connected to the same pumping station and assists with pumping the off-axis vapor away. The details of the custom oven we used are shown in Figure 4.8(b). Part a is a Swagelok union that will be connected to a copper tube containing the rubidium ampoule. Part b is a 2.75" CF flange with electric feedthroughs and the center feedthrough for the copper tube. A thermal breaker is added between the copper tube and the flange to keep a temperature gradient. Part c is the long copper tube for delivering the rubidium vapor from the ampoule to the collimator. The
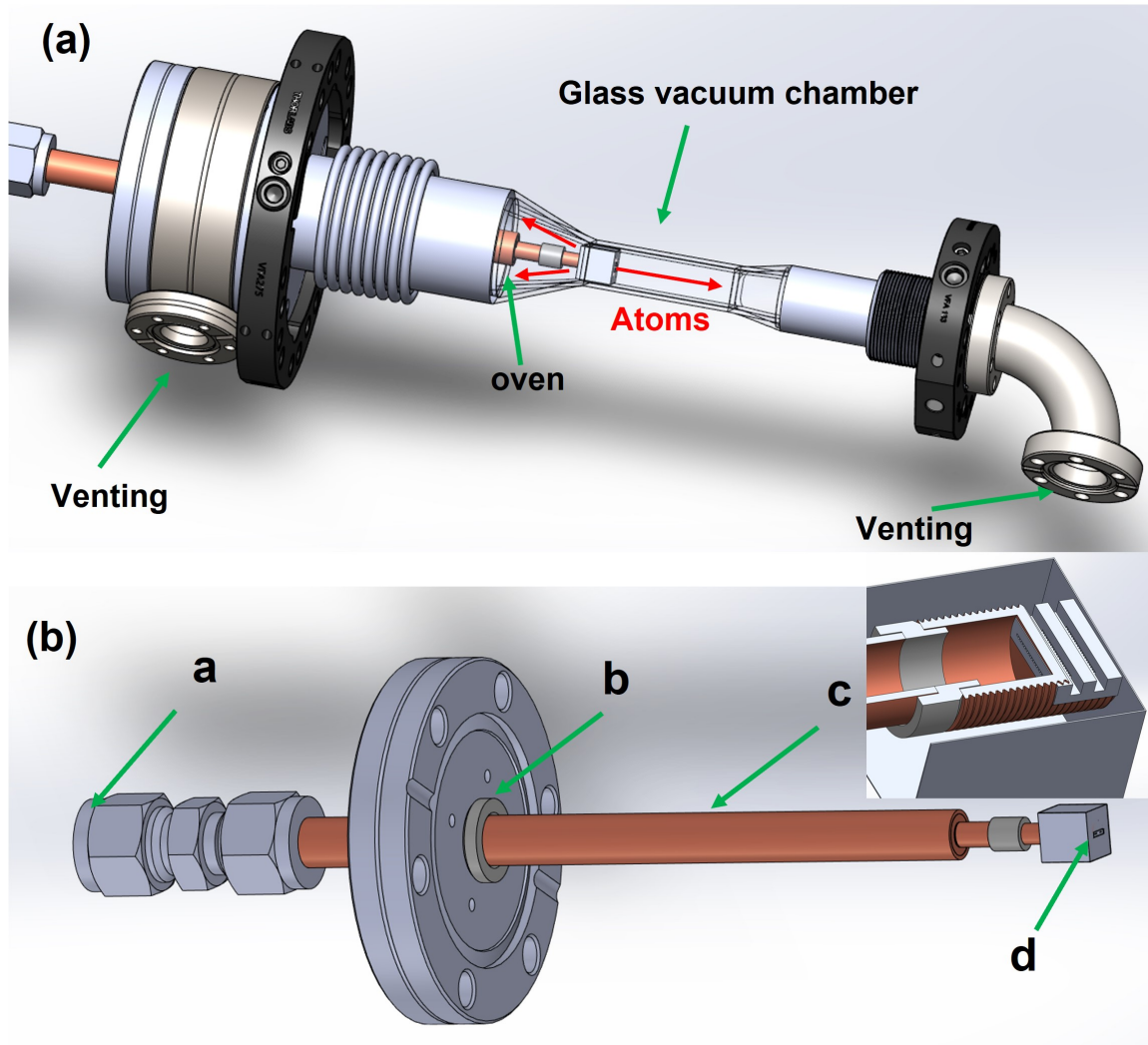
Figure 4.8: (a) A SolidWorks model of the glass vacuum chamber we used. The main cuboid glass section has great optical access and is attached to vacuum flanges with bellows in between to reduce stress. A custom-made oven is inserted from the left (details see (b)), and atomic beams can propagate through the glass section. Two venting ports on each side are connected to the same pumping station to pump away both the vapor and the beam component. (b) The custom-made atomic oven. Part a is a Swagelok union that can be connected to a copper tube containing the rubidium ampoule. Part b is a 2.75" CF flange with feedthroughs. A thermal breaker is added between the copper tube and the flange to keep a temperature gradient. Part c is a long copper tube for delivering the rubidium vapor. Its in-vacuum section is wrapped with a Kapton heating film. Part d has the adapter for our silicon cascaded collimator. The inset shows a cutaway diagram of part d with our cascaded collimator.

section inside the vacuum is wrapped with a Kapton heating film, and the section outside the vacuum is wrapped with a rope heater. Part d has the adapter to connect the copper tube to our silicon cascaded collimator we have discussed in section 2.2. A cutaway diagram is shown in the inset of Figure 4.8(b).coupling Nichrome wires are wrapped around the adapter to keep the adapter $20°$higher than the tube to prevent clogging of the channels. The off-axis vapor leaves through the gaps in the collimator while the on-axis atomic beam travels toward the right port. A small box made of thin stainless steel plates is attached around the collimator to keep the off-axis vapor away from the interaction region. The cascaded collimator consists of 20 channels, each with a cross-section of 100 μm $\times 100$ μm, resulting in a beam with a narrow divergence angle ($\theta_{1/2} = 0.013$ rad, corresponding to a transverse velocity spread of only ± 4 m/s). The excellent two-dimensional passive filtering of our device, combined with velocity selection, can isolate slow atoms with small three-dimensional velocity vectors.

4.4 Velocity selection

With our vacuum setup and the photon time tagging system, the next step is to isolate the slow atoms in our thermal atomic beams. The mean velocity for a rubidium atomic beam is around 300 m/s. For a field of view of 100 μm, the transit time is only 333 ns, which is too short for meaningful interactions and operations. Since the purpose of using thermal atoms is miniaturization and scalability, simple velocity selection is preferred compared with laser cooling.

The ^{87}Rb D_2 line transition diagram and experimental procedure are shown in Figure 4.9. To select the slow atoms, a Doppler-free pump beam first pumps all atoms into the hyperfine $F = 1$ state, while an angled repump beam then selectively pumps atoms back to $F = 2$ depending on their longitudinal velocity. For the repump beam interacting with
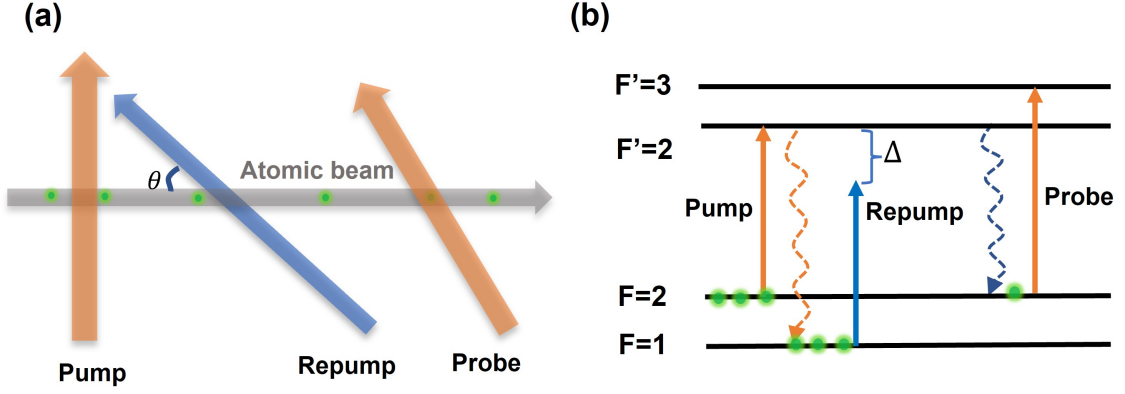
Figure 4.9: (a) The schematics for velocity selection and doppler sensitive detection. The atoms are first pumped into the F=1 dark state and then selectively pumped back to F=2. A doppler sensitive probe beam is first used to detect the selected atoms. The angle between repump and the atomic beam is $\theta = 47°$. (b) The involved energy levels for ^{87}Rb D_2 line. The repump is detuned by Δ to select a certain group of atoms.

atoms with velocity v, the scattering rate is

$$R_{sc}(v, \Delta) = \frac{\Gamma}{2} \frac{s}{1 + 4(\frac{k \cdot v \cos\theta - \Delta}{\Gamma}) + s} \tag{4.7}$$

Where Γ is the spontaneous decay rate, s is the saturation parameter, $\Delta < 0$ and k are the detuning and the wave number of the repump beam, and θ is the angle between repump and the atomic beam. The selected atoms are expected to have a velocity center at $v_c = \frac{\Delta}{k \cos\theta}$, and a FWHM of $\frac{\sqrt{1+s} \cdot \Gamma}{k \cos\theta}$. Low velocities were selected by decreasing the detuning $|\Delta|$ toward 0. We first used a doppler sensitive probe beam with an angle to the atomic beam couples the $F = 2 \rightarrow F' = 3$ transition to qualitatively detect the selected atoms with $\Delta = -80$ MHz. The spectrum data was collected by scanning the frequency of the angled probe beam. The fluorescence data is recorded with a silicon photodiode, and the photocurrent is amplified by 10^9 times with a current amplifier (Model 1211 DL Instruments). The data is shown in Figure 4.10. Similar to the methods we used in subsection 2.2.3, the voltage signal is a convolution between the scattering rate and the velocity distribution atoms $n(v)$. When the saturation parameter is small, the voltage is roughly proportional to $n(v)$. The yellow curve is the spectrum without repump beam. The bump around -500 MHz is the
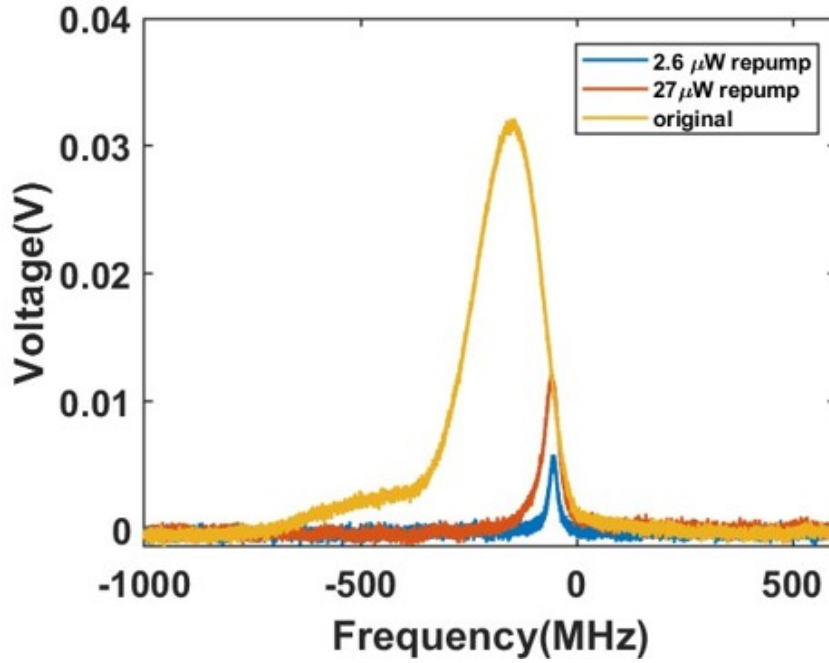
Figure 4.10: The optical spectrum data of the velocity selection with Δ=-80 MHz. The angle between the probe and the atomic beam is around 65.8°. The original spectrum without velocity selection (yellow) and the spectrum with a repump power of 2.6 μW (blue) and 27 μW (red) are shown. The saturation parameter of the probe beam is 6.

contributions from $F = 2 \rightarrow F' = 1,\ 2$. With the repump beam, it can be clearly seen that only a certain group of atoms are selected. The smaller the repump beam power, the smaller the FWHM. The expected $v_c = 92$ m/s for $\Delta = -80$ MHz, and the measured $v_c = 103$ m/s. This doppler sensitive detection method is very simple and easy to implement. However, the velocity distribution for atoms in a thermal atomic beam is

$$\rho(v) = 2\frac{v^3}{v_0^4}e^{-v^2/v_0^2} \tag{4.8}$$

Where $v_0 = \sqrt{\frac{2kT}{m}}$, k is the Boltzmann constant and m is the mass of the atom. The ratio of atoms with a velocity below 30 m/s in a thermal rubidium atomic beam is very small, only $\approx 7{\times}10^{-5}$ by calculating $\int_0^{30} \rho(v)dv / \int_0^{\infty} \rho(v)dv$. This detection method has many sources of error that are detrimental for measuring atoms with a slower velocity. First, under high amplification, electronic noise is a huge problem. The signal with $\Delta = -80$ MHz already

suffers a lot from electronic noise. Second, the angled probe beam is only sensitive to the velocity along with the optical k vector. Thus, it can't distinguish background vapor from the slow atoms in the atomic beam. Third, the fluorescence from unwanted isotope ^{85}Rb could affect the accuracy of this detection method. Thus, in the next section, we demonstrated a novel single-atom photon correlation method to measure the slow atoms accurately.

4.5 Photon coincidences measurements

4.5.1 Setup

This technique works as follows. A cylindrical plastic holder with a one-inch diameter and 8 mm thickness is machined. Three through holes with a diameter of 340 μm are drilled in the center for placing the bare fiber. Two fibers are cleaved and fixed on two adjacent holes of the holder. The images of the holder and the cleaved fiber tips are shown in Figure 4.11 (a) and (b), respectively. The distance between the two fiber tips is 450 μm. This holder is then fixed on the image plane of our imaging system and forms two detection regions separated by $d \approx 55$ μm at the objective plane. The other end of each fiber is connected to a single photon counting module (SPCM) where the detected photons are time tagged and analyzed. As shown in Figure 4.11(c), after the velocity selection, the probe beam is focused and sent perpendicular to the atomic beam to excite all the atoms. The probe beam has a beam waist of $w \approx 60$ μm that overlaps both detection regions. When a single atom passes through two detection regions, the photons collected from the two fibers will contribute to time-ordered coincidences with a delay $\tau = \frac{d}{v}$. The accidental coincidences from laser scattering, detector dark counts, etc., do not depend on time delay and can be subtracted later. The coincidences signal can be averaged for a long time to detect tiny signals. Before showing the photon correlation data, we would like to show more details about our optical setup and some procedures we utilized to minimize the uncorrelated photon counts. The optical layout to generate the pump, the repump, and the
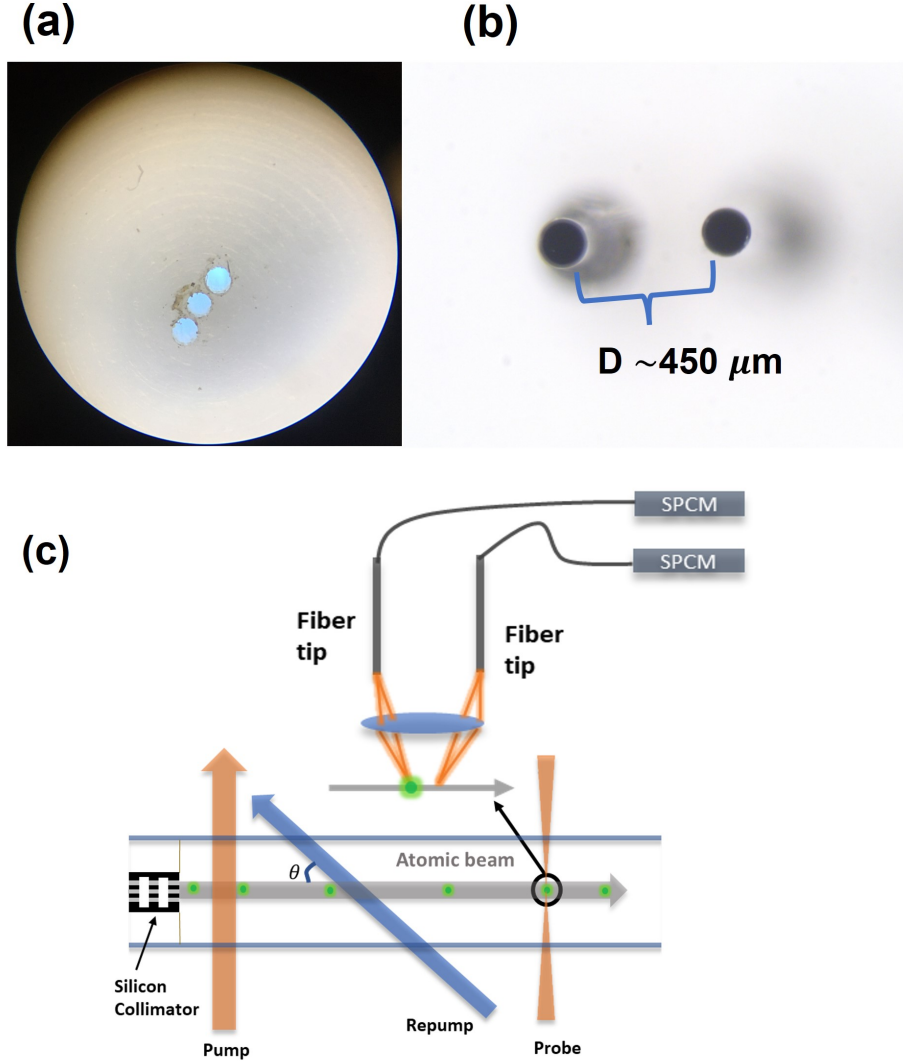
Figure 4.11: (a) The optical image of our plastic fiber holder. The distance between holes is around 500 μm. (b) An optical image of the fiber tips after two fibers are fixed on our fiber holder. The distance between two fiber tips is measured to be 450 μm. (c) The schematics of the experiment. Two fibers formed two detection regions. Atoms pass through two detection regions, emitting photons in each region, and the time delay between photons is used to determine the velocity.

probe beams is shown in Figure 4.12. In order to pump all the atoms to the F=1 dark state, the pump beam is enlarged by a telescope and placed very close to the atomic channels. A darkened razor blade is used to cut the tails of the pump beam towards the silicon collimator to reduce the scattering light. Some fast atoms still manage to escape the pump and get to the probe region. A higher pump power will reduce the number of fast escaped atoms but
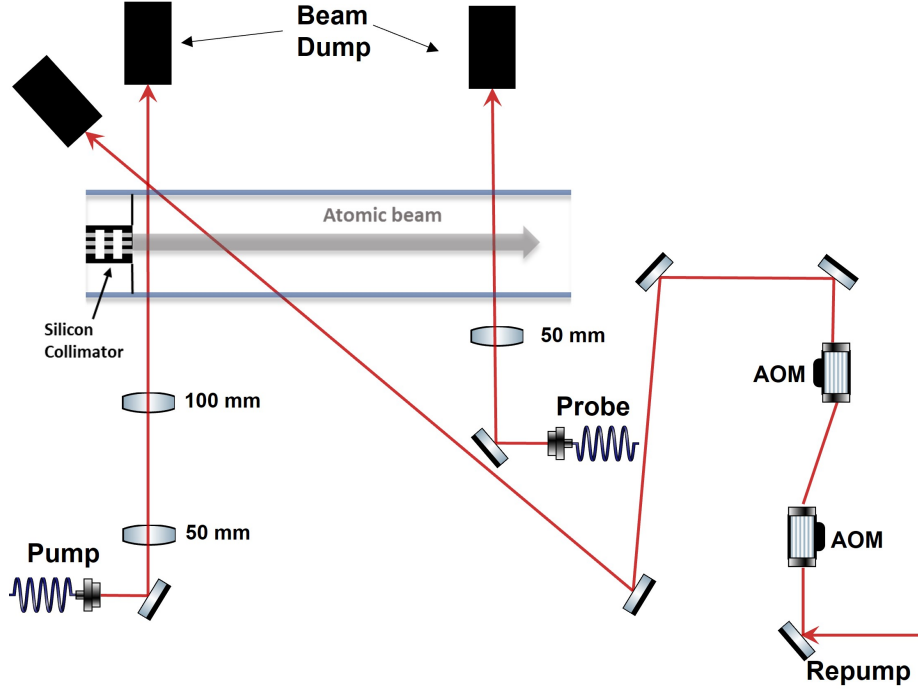
Figure 4.12: The our optical layout for the single atom photon correlation experiment. The repump beam is from a free space laser, and the space between the laser and the setup is blocked carefully to avoid scattering light. The beam dumps are long lens tubes with irises and darkened ends.

will increase the scattering light. Thus, the power of the pump beam was experimentally set to 2 mW which minimized the sum photon counts of laser scattering and unpumped fast atoms. The repump beam is sent through two AOMs with a center frequency of 80 MHz. One AOM can shift the frequency Δ_1, and the other AOM shifts the frequency $-\Delta_2$. Thus, we can achieve arbitrary frequency shift $\Delta = \Delta_1 - \Delta_2$. The repump power is set to around 4 μW to get a narrow FWHM of velocity distribution. To detect single atoms in a thermal beam, we need to make our field of view very small and the probe beam very small. A small field of view and a small probe beam will minimize the scattering light and make the detection region small enough to have an average atom number smaller than 1. The probe beam is focused by a 50 mm lens, and the focal point is centered on the atomic beam. Our imaging system consists of a 20X long working distance objective (Mitutoyo NA=0.42), and a 50 mm tube lens. The field of view is located at the center of the glass
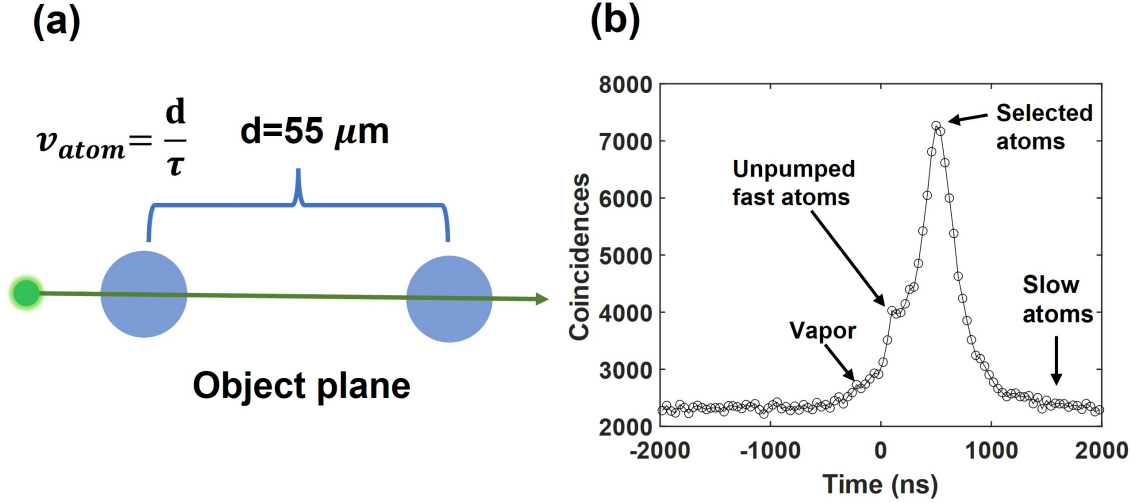
Figure 4.13: (a) The schematic for explaining the photon correlation experiment. An atom with velocity v passes through two fiber tip regions and contributes to the coincidences at the time delay $\frac{d}{v}$. (b) The raw coincidences data for $\Delta = -80$ MHz. The power of repump beam is 5 μW, and the probe beam power is 20 μW.

chamber to reduce the scattering light from the wall. The plastic holder is designed to have a one-inch diameter and sit within a lens tube coaxially with our imaging system. The fibers are taped in multiple places on the mount to create stress relief points. A camera is first used in the image plane to adjust the imaging system to have a proper image of the atomic beam. Then, the plastic holder with the fibers replaces the camera, and the imaging system is fine-tuned to maximize the count rate from the fibers. All laser beams are terminated with carefully designed beam dumps to reduce scattering light. Thorlabs blackout fabric, high-performance black masking tape, and black hardboard are used extensively to avoid any scattering light and environmental light.

4.5.2   Atom velocity distribution measurement

Figure 4.13 (b) shows the raw coincidence data for $\Delta = -80$ MHz. The peak around +500 ns is the contribution from velocity-selected atoms with a center velocity $v = \frac{d}{\tau} \approx 100$ m/s. The extra coincidences at time delays larger than 1000 ns are the slow atoms that we are interested in. Some fast atoms in the atomic beam escape the pumping process and

contribute to the small bump at around +100 ns. During the data acquisition time, a small rubidium vapor gradually builds up and contributes to coincidences with both positive and negative time delays around zero. This vapor could be removed in future experiments for greater selectivity, for example, by adding a small amount of graphite to the vacuum cell. The imperfection in imaging can cause a small probability of detecting photons from atoms between two fiber tips, creating spurious coincidences very close to zero time delay. Thus, the accuracy for fast atoms is not great. But the accuracy for slow atoms is very high, which is what we care about.

We can analyze the second-order temporal coherence between SPCM A and SPCM B:

$$g_{AB}^{(2)}(\tau) = \frac{\langle I_A(t)I_B(t+\tau)\rangle}{\langle I_A(t)\rangle\langle I_B(t+\tau)\rangle} \tag{4.9}$$

From Equation 4.6, we know that $g_{AB}^{(2)}(\tau)$ measures the distribution of coincidences with time delay τ and $g_{AB}^{(2)}(\infty) \to 1$ represents accidental coincidences. The correlated part $g_{AB}^{(2)}(\tau) - g_{AB}^{(2)}(\infty)$, after normalization, is the coincidence probability density in the time domain $n_{AB}(\tau)$. Given $n_{AB}(\tau)d\tau = n_{AB}(v)dv$ and $\tau = \frac{d}{v}$, we can derive $n_{AB}(v)$, which is the number density of coincidences contributed by atoms whose velocity is v. The coincidences generated by each atom are proportional to the square of transit time through a single fiber's detection region, whose diameter is d_f. Then the atom probability density $\rho(v)$ is derived from coincidence data by using $n_{AB}(v) \propto \rho(v) \cdot \frac{d_f^2}{v^2}$. We will show the details of theoretical derivations in the next section.

For $\Delta = -80$ MHz and oven temperature $100\,^{\circ}$C, the data for $n_{AB}(v)$ is shown in Figure 4.14(a). It shows the photon coincidences contributed by atoms with velocities ranging from 0 to 250 m/s. Figure 4.14(b) is the calculated atom probability density distribution $\rho(v)$. Compared with the original thermal atomic beam velocity distribution (Figure 4.14(b) inset), the selected atoms have a much lower velocity–the peak is at 106 m/s, which agrees reasonably well with the theoretical expectation of 92 m/s.
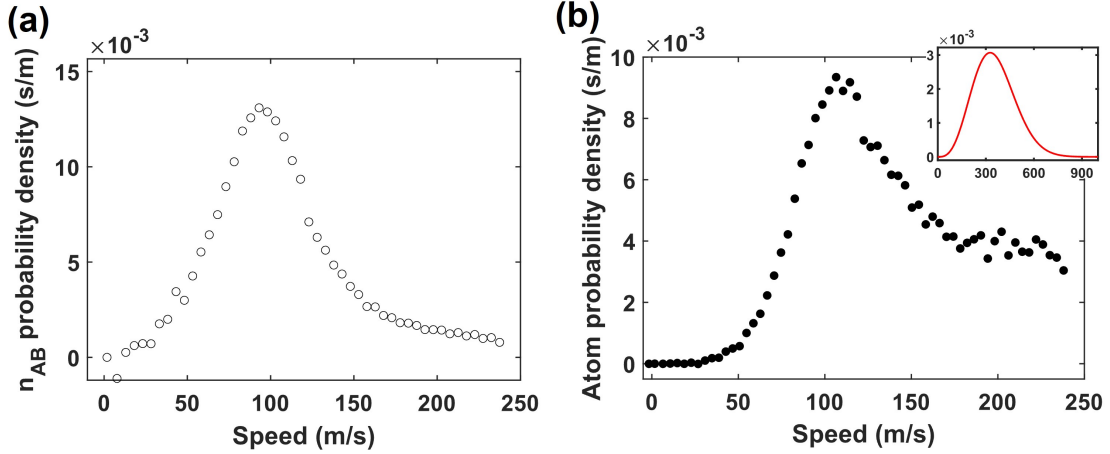
Figure 4.14: (a) The coincidences distribution in velocity domain with detuning $\Delta = -80$ MHz. The peak velocity is 93 m/s. (b) The calculated atom probability density distribution for $\Delta = -80$ MHz. The peak velocity is 106 m/s. The inset shows the original thermal distribution at 100 °C.

When calculating the $g_{AB}^{(2)}(\tau)$ for this two-fiber correlation data, a special data analysis technique is used to improve the signal quality. From Equation 4.5, we know that $g_{AB}^{(2)}(\tau)$ normally uses constant time bin size Δt for all time delays. However, we are looking at the velocity distribution of atoms which is in the velocity domain. We know that $d\tau = \frac{d}{v^2}dv$, a constant time bin size will create very sparse data points in the high-velocity range and super dense data points in the low-velocity range. Since the time bin size determines the averaging effect, super dense data points in the low-velocity range have weaker averaging effects and will have unwanted noise. Thus, we created the time bins to be larger at longer time delays and smaller at short time delays such that the data points are uniform in the velocity domain as shown in Figure 4.14.

To select even slower atoms, we used $\Delta = -20$ and -10 MHz, whose data for $n_{AB}(v)$ are shown in Figure 4.15(a) and (c). We can clearly see the coincidences have shifted to lower velocities, with the peak occurring at 30 m/s and 20 m/s, respectively. To calculate the $\rho(v)$ of our selected atoms, a background measurement with no repump beam is also conducted (with pump and probe). The contributions from background vapor and un-pumped fast atoms are approximately subtracted. The corresponding $\rho(v)$ are shown in Fig

108
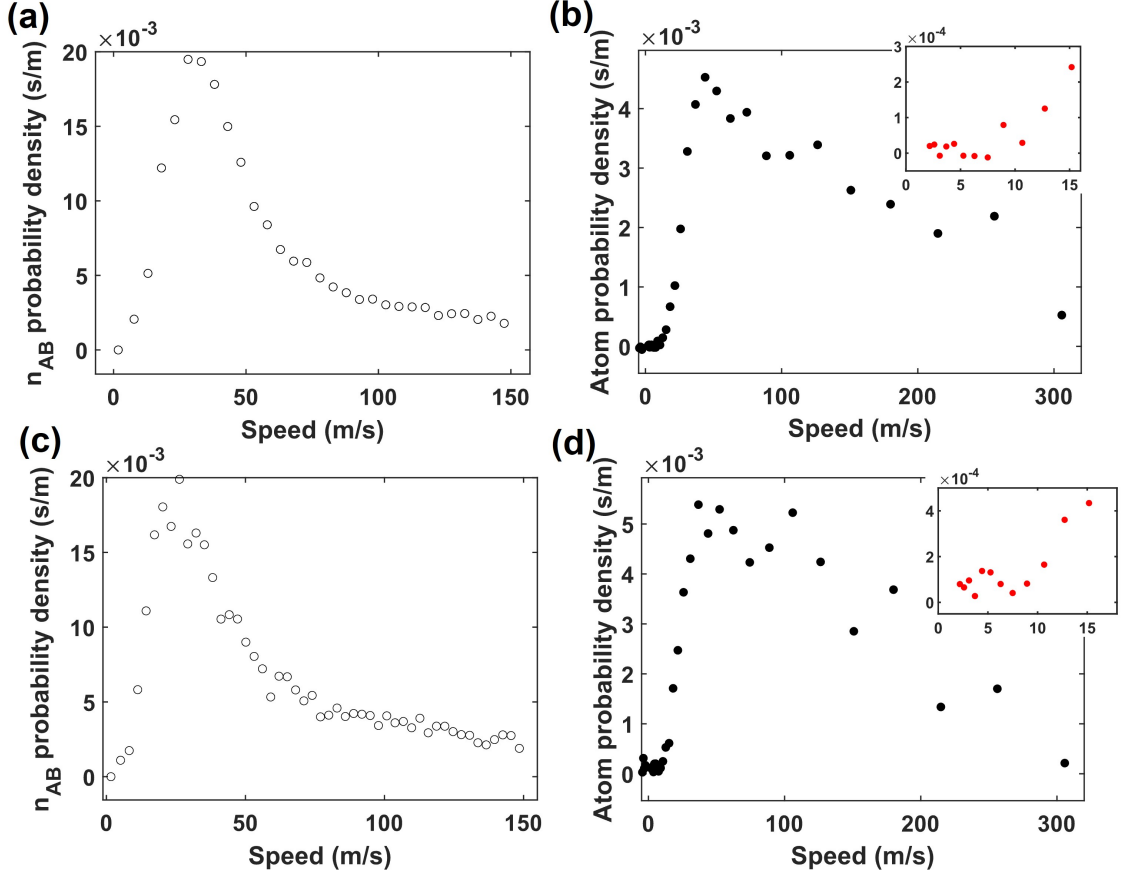
Figure 4.15: (a) and (c) The coincidences distribution in velocity domain with detuning $\Delta = -20$ MHz and -10 MHz. The peak velocity is at 30 m/s and 20 m/s, respectively. (b) and (d): The calculated atom probability density distribution for $\Delta = -20$ MHz and -10 MHz. With the effect of fast atoms and vapors, the peak velocities are all at ≈ 50 m/s. The insets are the zoomed-in plot into the slow velocity. Atoms with velocities around 15m/s can be clearly distinguished.

Figure 4.15 (b) and (d). Here, the size of time bins is chosen to be larger than the case with $\Delta = -80$ MHz in the high-velocity range to have a more average effect. Compared with the coincidence $n_{AB}(v)$, the atom probability density distribution is broader and has bigger tails in high velocities. The reason is that slower atoms contribute more coincidences. Thus, the peak locations for $n_{AB}(v)$ are closer to 0, and the peaks are narrower. The expected peak of atom probability density is at 23 m/s and 12 m/s for Figure 4.15 (b) and (d), while the actual peak locations are both at around 50 m/s.

Several nonidealities limited the velocity selection purity. First, the imperfection in

imaging can cause a small probability of detecting photons from atoms between two fiber tips, creating spurious coincidences similar to ultra-fast atoms. Some fast atoms managed to avoid being optically pumped through the pump beam, and the background rubidium vapor within the small glass chamber increased with time during the experiment. The background subtraction helps to reduce the effects of vapor and unpumped fast atoms. But the background vapor pressure change with time and is not subtracted completely. The photon counts from selected atoms are around 300 counts/s when $\Delta = -20$ MHz and only 200 counts/s for $\Delta = -10$ MHz. As a comparison, the laser scattering rate plus the fast unpumped atoms contribute around 1100 counts/s. The vapor contributions started from almost zero and can increase to 1000 counts/s depending on the time of the experiment. These effects together contributed around 10 times greater background photon count rates compared with the signal from the velocity-selected atoms at $\Delta = -10$ MHz. After averaging for several hours, the correlation method we used could distinguish the small correlated signals, but some faster atoms inevitably shifted the peak location and caused the long tail in Figure 4.15 (b) and (d). As for detunings Δ closer to 0, the signal from selected atoms is even smaller. We measured $\Delta = -5$ MHz, in which the vapor and unpumped fast atoms dominate $\rho(v)$, and the data is thus not shown. The vapor component could be removed in future experiments for greater selectivity, for example, by adding a small amount of graphite to the vacuum cell.

Atoms with velocities between 10 and 15 m/s are clearly observed, as shown in the inset of Fig Figure 4.15 (b) and (d). The atoms with a velocity below 15 m/s only constitute 10^{-6} of the thermal atomic beams. In summary, we demonstrated a novel and powerful approach based on correlated photons from single atoms to characterize atoms' velocity distribution. This also demonstrates that we can isolate and directly observe slow atoms with a velocity $< \overline{v}/20$, where $\overline{v}$ is the mean velocity of the unselected atomic beam.
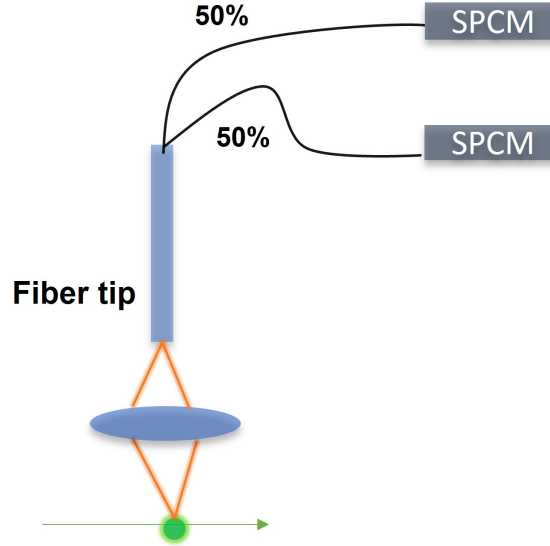
Figure 4.16: The single fiber setup with Hanbury-Brown and Twiss configuration to measure the atoms' second order correlation function.

4.5.3 Photon pairs and triplets from single atoms in atomic beams

In this section, we will show the result of our experimental measurements on single atoms in an atomic beam, demonstrating their utility in a "bottom-up" approach to quantum system preparation using thermal vapors.

A key signature of single atoms is the photon antibunching effect [31]. In order to measure the second-order correlation function $g^{(2)}(\tau)$, the collector with two fiber tips in the previous section is replaced by a single fiber tip that is connected to a 50:50 fiber splitter and two SPCMs to achieve a Hanbury-Brown and Twiss configuration (see Figure 4.16). The field of view of has a diameter $d_f \approx 25\mu$m.

We first measured the $g^{(2)}(\tau)$ of an unfiltered thermal atomic beam by removing the pump and repump beams and reducing the oven temperature to 78 °C to achieve $\langle N \rangle < 1$ in the field of view. The data are shown in Figure 4.17 (a). For classical light the condition $g_2(\tau) \leq g_2(0)$ must be met [108], and therefore the observed dip around $\tau = 0$ is the evidence for the quantum-mechanical antibunching effect from single atoms [31, 109]. After an emission event, an atom needs time to be re-excited to emit a second photon, and

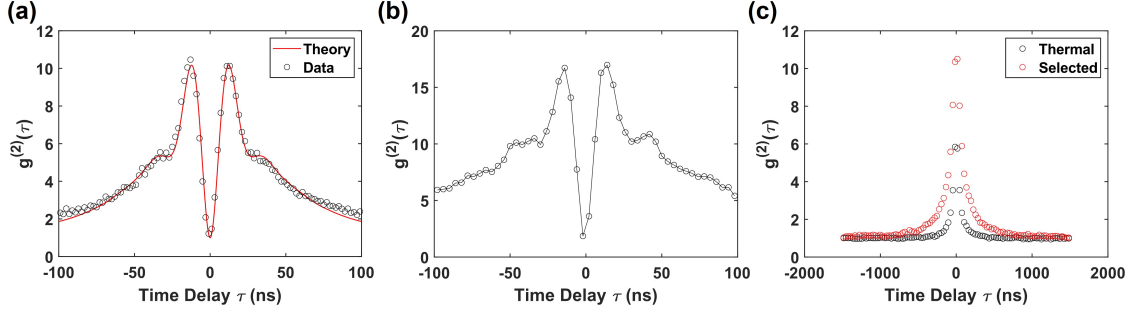Figure 4.17: (a) $g^{(2)}(\tau)$ with thermal atomic beam at 78 °C. The time bin size is 2 ns. The red line is the theory curve with $\langle N \rangle = 0.138$, $L = 25$ μm. Check the theory section (section 4.6) for details. (b) $g^{(2)}(\tau)$ with selected atoms. The peak value is higher because the average atom number is smaller compared with the thermal atomic beam. The selected atoms are more confined in space and suffer less intensity variance in the probe beam. Thus the second Rabi peak is more visible. The time bin size is 4 ns. (c) Both $g^{(2)}(\tau)$ for thermal and selected atoms are plotted in the long time delay range.

therefore the maximum of $g^{(2)}(\tau)$ occurs around the first half Rabi cycle. At zero time delay, $g^{(2)}(0) = 1$ rather than 0 because the atomic beam follows the Poisson distribution and the single emitter condition is not always satisfied.

In comparison with trapped atom systems [110, 111, 112], the peak value of $g^{(2)}(\tau)$ observed was much larger, as high as 10. Such a large value for the photon pair correlation is comparable to what has been observed for correlated photon pairs using four-wave mixing [92, 113]. The photon pairs generated here are sequentially emitted photons by single atoms. This is because the accidental coincidences scale with $\langle N \rangle^2$, while the correlated coincidences scale with $\langle N \rangle$. Thus in an atomic beam where $\langle N \rangle \ll 1$, the ratio of correlated coincidences is much higher. With the Poisson process averaging and transit time correction, the $g^{(2)}(\tau)$ for a thermal atomic beam can be written as (see the theory section—section 4.6 for derivation):

$$g^{(2)}(\tau) = \frac{\int_{v=0}^{v=L/\tau}(1 - \frac{v\tau}{L})\frac{\rho(v)}{v}}{\int_v \frac{\rho(v)}{v}dv} \cdot \frac{g^2_{single}(\tau)}{\langle N \rangle} + 1 \tag{4.10}$$

Where L is the length of the field of view in the atomic beam direction, $\rho(v)$ here is the atomic beam Maxwell-Boltzmann velocity distribution, and $g^{(2)}_{single}(\tau)$ is the second-

112

order coherence function of a single stationary atom. From this equation, we can see that $g^{(2)}(\tau) - 1$ is inversely proportional to the average atom number $\langle N \rangle$ and the high $g^{(2)}(\tau)$ value only appears when $\langle N \rangle < 1$. The theoretical curve fits well with the data (Figure 4.17 (a)).

To confirm and compare this effect, the velocity selection scheme was used to measure the $g^{(2)}(\tau)$ for slow atoms at a repump detuning $\Delta = -20$ MHz, with the data shown in Figure 4.17 (b). The $g^{(2)}(\tau)$ peak is even higher, reaching 17, due to the smaller averaged atom number for this data. Since the transit time for slow atoms is much longer, $g^{(2)}(\tau)$ also decays more slowly at long τ. Figure 4.17 (c) shows the comparison between the $g^{(2)}(\tau)$ of thermal atoms and selected atoms. The correlated photons can be seen for $\tau > 1000$ ns, coming from atoms with $v < 25$ m/s. This shows that by using simple velocity selection with thermal beams, we can observe a single atom for longer than 1 μs.

The extraordinarily high $g^{(2)}(\tau)$ value means a high probability of detecting a second photon at τ time delay given the first photon. The extraordinarily high $g^2(\tau)$ value occurs because atoms only enter our field of view infrequently (the average atom number is $\langle N \rangle \approx 0.1$), and therefore photons will be bunched around these events. High photon correlation has been observed in Mollow triplet [114]. But we are not looking at the Mollow triplet since our light intensity is small (9 I_s), our $g^{(2)}(\tau)$ is much larger [115], and only one nice fluorescence peak is observed. Our condition of smaller than one atom in the field of view is also not preferable for Mollow triplet [114].

The beautiful thing here is that this process naturally happens in thermal atoms, and it is robust against the broad speed distribution. Because the photon separation in the bundles is only determined by spontaneous emission rate and Rabi frequency, the time delay between the photon pairs can be tuned by the probe laser intensity. With the thermal beam at 78 °C and a probe laser power of 7 μW, the collected photon pairs have a rate of 0.16 pairs per second per fiber. However, the simplicity and small size of the source should not be overlooked. To achieve a practical output flux, one can readily multiplex the output
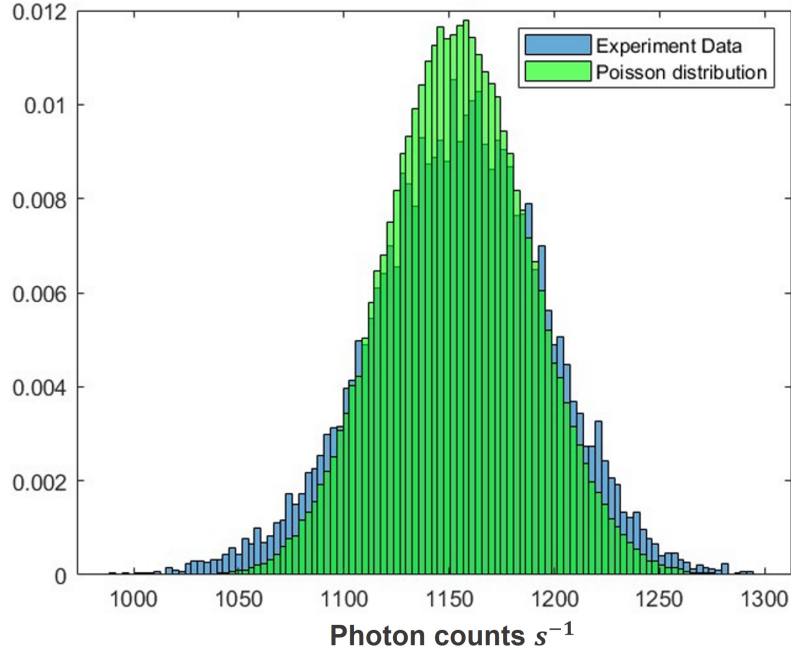
Figure 4.18: The histogram of photon counts in one second. The x-axis is the number of photon counts in one second, and the y-axis is the probability density. The histogram of our experimental photon tags and an ideal Poisson distribution with the same mean are plotted. The blue experimental data is from selected atoms with $\Delta = -20$ MHz, and it is clearly wider than the Poisson distribution, showing the super-Poissonian statistics.

of several regions, for example, by adding more fibers. Each fiber can be treated as an independent photon pair source. We can also try to improve the collection efficiency, as the pair rate scales quadratically with the efficiency. Moreover, unlike spontaneous parametric-down-conversion sources [116, 117], this system requires no wavelength filtering and is ideally suited for interaction with rubidium atoms.

Super-Poissonian distribution

The photon number statistics are also calculated with our photon tags data. Figure 4.18 shows the histogram of photon counts in one second for our experimental data and an ideal Poisson distribution. In a Poisson distribution of photons, the variance equals the mean. However, if our photons are bunched, as shown in the $g^{(2)}(\tau)$, the photon statistics should be super-Poissonian, which means the variance is bigger than the mean. The reason is

that our atoms follow Poisson distribution, but each atom can create a bunch of photons, increasing the variance in the photon number statistics. In Figure 4.18, our photon counts distribution has a larger variance and is clearly wider than the Poisson distribution. This is another piece of evidence for super-Poissonian statistics and the photon bunching nature of the emitted light.

Photon triplet

Photon triplet generation has been a longstanding challenge in the quantum optics field [118, 119, 120]. We expect our system to also generate photon triplets. The third-order correlation function $g^{(3)}(\tau_1, \tau_2)$ measures the temporal correlation of three photons:

$$g^{(3)}(\tau_1, \tau_2) = \frac{\langle I_A(t) I_B(t + \tau_1) I_C(t + \tau_2) \rangle}{\langle I_A(t) \rangle \langle I_B(t + \tau_1) \rangle \langle I_C(t + \tau_2) \rangle} \tag{4.11}$$

A high $g^{(3)}(\tau_1, \tau_2)$ value means a high probability of detecting three photons with time delay τ_1 and τ_2 compared with other time delays. Similar to the derivation of Equation 4.5, we can derive the numerical formula from calculating the $g^{(3)}(\tau_1, \tau_2)$ from time tags data:

$$g^{(3)}(\tau_1, \tau_2) = \frac{n_{123}(\tau_1, \tau_2) \cdot T^2}{n_1 n_2 n_3 \Delta t^2} \tag{4.12}$$

$g^{(3)}$ was measured using two detectors in the Hanbury Brown and Twiss configuration. We recorded the arrival time of photons from SPCM A and SPCM B with an accuracy of 350 ps and a dead time $\Theta \approx 45$ ns. Then, since photons don't distinguish SPCM A and SPCM C, the time tags from SPCM A were used as the time tags for SPCM C. We removed the spurious coincidences at $\tau_2 \approx 0$ and a partial function $g^{(3)}(\tau_1, \tau_2 > \Theta)$ was measured.

Figure 4.19 (a), (b) shows the data for the thermal atomic beam and $\Delta = -20$ MHz selected atoms, respectively. The time bin size is 100 ns $\times$ 100 ns and $g^{(3)}(\tau_1, \tau_2 < \Theta)$ is left blank. The peak around zero results from the consecutive three photons emitted during the transit of single atoms. When $\tau_1 \approx \tau_2$, channels B and channel C will have
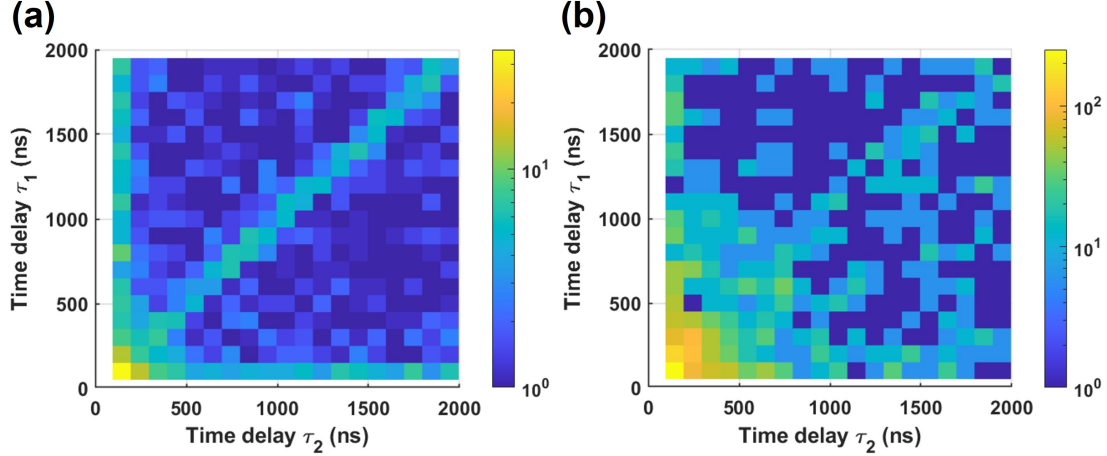
Figure 4.19: Measured $g^{(3)}(\tau_1, \tau_2 > \Theta)$. (a) Thermal atomic beam at 78 °C. The maximum $g^{(3)}$ is around 39. (b) Selected atoms by using a detuning of $\Delta = -20$ MHz. The maximum $g^{(3)}$ is around 280.

more coincidences as shown in the $g^2(\tau)$ measurements, resulting in a higher value of three-photon coincidences and a diagonal line in Figure 4.19 (a). When τ_1 or τ_2 close to zero, the same reason leads to the brighter lines close to the axis. For Figure 4.19 (b), the number of three-photon coincidences is not large enough, and this pattern is blurred by shot noise. Comparing Figure 4.19(b) to (a), stronger third-order correlations from slow atoms are detected in large time delays, showing the capability to collect photon triplets from a single atom for more than 1 μs.

The maximum values of $g^{(3)}(\tau_1, \tau_2 > \Theta)$ reach 39 and 280 for each case, showing great potential as a photon triplet source. For the thermal beam, we collected ≈ 0.166 triplets per minute. The rate of photon triplet is proportional to the cubic of collecting efficiency. Improving the collecting efficiency and adding more fibers in the imaging plane can create bright, narrow linewidth photon triplets that are compatible with Rubidium-based systems.

4.6 Theoretical calculations

This section will first discuss the theory of the second-order correlation function of single atoms in a thermal atomic beam. A comparison of our theory with Ref [109] is also con-
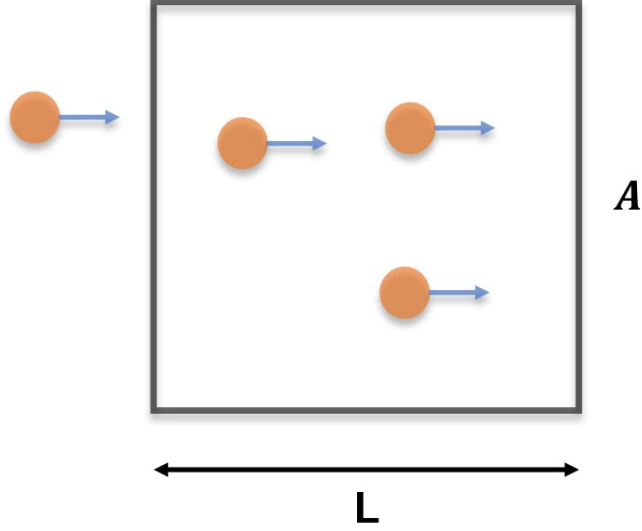
Figure 4.20: Diagram of the collection region of a single fiber showing individual atom transits.

ducted. Then, we will discuss the theory behind the two fiber coincidence measurements and how to extract the velocity distribution. The effects of extra uncorrelated noise are also analyzed. With the detailed theoretical derivation, we gained a deeper understanding of these correlation measurements and showed why they need to be done in the single-atom regime.

4.6.1 Second order correlation function for single fiber

The second-order correlation function $g^{(2)}(\tau)$ is defined to be:

$$g^{(2)}(\tau) = \frac{\langle I_A(t)I_B(t+\tau)\rangle}{\langle I_A(t)\rangle\langle I_B(t+\tau)\rangle} = \frac{\langle n_A(t)/\Delta t \cdot n_B(t+\tau)/\Delta t\rangle}{\langle n_A(t)/\Delta t\rangle\langle n_B(t+\tau)/\Delta t\rangle} \qquad (4.13)$$

Where $n_{A,B}(t)$ is the number of detected photons from detector A(B) in time bin Δt at time t and $I(t) \propto \frac{n(t)}{\Delta t}$. The effect of $g^{(1)}(\tau)$ can be negligible in our system. For our thermal atomic beam experiment, the background counts are negligible ($< 1\%$). Thus, we ignore the background counts and only consider photons from the atoms. The effects of uncorrelated background photons will be discussed in subsection 4.6.4.

For an effusive thermal atomic beam, the velocity distribution of the flux follows:

$$\rho(v) = 2\frac{v^3}{v_0^4}e^{-v^2/v_0^2} \tag{4.14}$$

Where $v_0 = \sqrt{\frac{2kT}{m}}$, k is the Boltzmann constant and m is the mass of the atom, and $\int_v \rho(v)dv = 1$. The mean number of atoms that transit our collecting region per second F_N is (see Figure 4.20):

$$F_N = \int_v n(v)\cdot vAdv = \int_v F_N\rho(v)dv \tag{4.15}$$

Where $n(v)$ is the density of atoms with a velocity between v and $v+dv$, and A is the cross-section area of the collecting region. $n(v)\cdot vA = F_N\rho(v)$. The relationship between F_N and the average atom number in the field of view $\langle N \rangle$ is:

$$\langle N \rangle = \int_v A\cdot L\cdot n(v)dv = F_N\int_v \rho(v)\cdot\frac{L}{v}dv \tag{4.16}$$

where L is the field of view length along the atomic beam direction.

For the denominator of Eqn. (Equation 4.13), the average number of photons detected is the product of mean atom number $\langle N \rangle$, scattering rate R_s, and collection efficiency C_{eff}. In terms of the velocity distribution, we can then write

$$\langle n_A(t)/\Delta t \rangle = C_{eff}R_sF_N\int_v \rho(v)\frac{L}{v}dv. \tag{4.17}$$

Moreover, since this average is time-independent, the denominator is simply

$$\langle n_A(t)/\Delta t \rangle\langle n_B(t)/\Delta t \rangle = \left(C_{eff}R_sF_N\int_v \rho(v)\frac{L}{v}dv\right)^2 \tag{4.18}$$

To calculate the numerator correctly, we must consider the fluctuating number of atoms in the volume. If $p(N_f)$ is the probability to have N_f atoms in the field of view, then

$\langle N \rangle = \sum_{N_f} p(N_f) \cdot N_f$. Thus, we can write the numerator as:

$$\sum_{N_f} p(N_f) \langle (n_{1A}(t) + n_{2A}(t) + ... n_{N_f A}(t))/\Delta t \cdot (n_{1B}(t+\tau) + n_{2B}(t+\tau) + ... n_{N_f B}(t+\tau))/\Delta t \rangle$$
(4.19)

Where $n_{iA}(t)$ represents the number of detected photons from detector A emitted by i^{th} atom in time bin Δt at time t. $n_{iA}(t) \cdot n_{iB}(t+\tau)$ are uncorrelated unless $i = j$. Therefore, we can write (Equation 4.19) as a correlated term and an uncorrelated term:

$$\sum_{N_f} p(N_f) \cdot \sum_{i=1}^{i=N_f} \langle n_{iA}(t)/\Delta t \cdot n_{iB}(t+\tau)/\Delta t \rangle + \sum_{N_f} p(N_f) \cdot \sum^{i \neq j} \langle n_{iA}(t)/\Delta t \cdot n_{jB}(t+\tau)/\Delta t \rangle$$
(4.20)

Since all atoms are equivalent, we may write $\langle n_i(t) \rangle = \langle n_j(t+\tau) \rangle$. Therefore, we may calculate everything in terms of just atom 1's emission:

$$\sum_{N_f} p(N_f) N_f \cdot \langle n_{1A}(t)/\Delta t \cdot n_{1B}(t+\tau)/\Delta t \rangle + \sum_{N_f} p(N_f) N_f (N_f - 1) \langle n_{1A}(t)/\Delta t \rangle \cdot \langle n_{1B}(t+\tau)/\Delta t \rangle$$
(4.21)

The relationship between expected $\langle n_{1A}(t)/\Delta t \rangle$ and $\langle n_A(t)/\Delta t \rangle$ can be derived:

$$\langle n_A(t)/\Delta t \rangle = \sum_{N_f} p(N_f) \langle (n_{1A}(t) + n_{2A}(t) + ... n_{N_f A}(t))/\Delta t \rangle = \sum_{N_f} p(N_f) N_f \langle n_{1A}(t)/\Delta t \rangle = \langle N \rangle \langle n_{1A}(t) \rangle$$
(4.22)

Using (Equation 4.18) and (Equation 4.22) with (Equation 4.21), the numerator can be written as:

$$\sum_{N_f} p(N_f) N_f \cdot \langle n_{1A}(t)/\Delta t \cdot n_{1B}(t+\tau)/\Delta t \rangle + \sum_{N_f} p(N_f) \frac{N_f(N_f - 1)}{\langle N \rangle^2} \left(C_{eff} R_s F_N \int_v \rho(v) \frac{L}{v} dv \right)^2$$
(4.23)

Next, we are going to solve the first correlated term, which is generated by the same atom and related to the single atom correlation. The correlated term also requires a transit time correction since the atoms are not stationary. From (Equation 4.13), we know that for a stationary single atom, $g_{single}^{(2)}(\tau) = \frac{\langle n'_A(t)/\Delta t \cdot n'_B(t+\tau)/\Delta t \rangle}{\langle n'_A(t) \rangle \langle n'_B(t+\tau)/\Delta t \rangle}$. Here $\langle n'_A \rangle = \langle n'_{BA} \rangle = C_{eff} R_s \Delta t$ is the mean number of received photons from a stationary atom without transit time correction. If we then introduce the

conditional probability $P(B(\tau)|A) \cdot \Delta t$ of detecting the second B photon within a time interval Δt at the time delay τ given that the first A photon was detected, we obtain

$$g_{single}^{(2)}(\tau) = \frac{\langle n'_A(t)/\Delta t \cdot n'_B(t+\tau)/\Delta t \rangle}{C_{eff}R_s \cdot C_{eff}R_s} = \frac{\langle n'_A(t)/\Delta t \rangle \cdot P(B(\tau)|A)}{C_{eff}R_s \cdot C_{eff}R_s} = \frac{P(B(\tau)|A)}{C_{eff}R_s} \quad (4.24)$$

For one atom transiting the field of view L with velocity v, if a coincidence with a time delay τ is to be detected, the first photon must have been emitted within a distance $L - v\tau$ to allow the second photon at τ to be detected. Thus the transit length for the first photon $\langle n_1(t)/\Delta t \rangle$ is effectively reduced to $L - v\tau$, resulting in a correction factor of $\left(\frac{L-v\tau}{L}\right)$ provided that $\tau < L/v$. No coincidences can be found from the same atom when $v > L/\tau$. Combining $g_{single}^{(2)}(\tau)$, the transit time correction factor and Eqn. (Equation 4.17), we finally obtain:

$$\langle n_{1A}(t)/\Delta t \cdot n_{1B}(t+\tau)/\Delta t \rangle = \int_{v=0}^{v=L/\tau} dv C_{eff}R_s \frac{F_N}{\langle N \rangle}\rho(v)\frac{L}{v} \cdot \frac{(L-v\tau)}{L} \cdot C_{eff}R_s \cdot g_{single}^{(2)}(\tau)$$

$$(4.25)$$

In the above, we may substitute the textbook formula for $g_{single}^{(2)}(\tau) = 1 - e^{-(3\Gamma/4)\tau} \cdot (\cos(\Omega_\Gamma\tau) + \frac{3\Gamma}{4\Omega_\Gamma}\sin(\Omega_\Gamma\tau))$ [43], where $\Omega_\Gamma = \sqrt{\Omega^2 - (\frac{\Gamma}{4})^2}$, and Ω and Γ are the Rabi frequency and spontaneous decay rate respectively.

Now we put it back into (Equation 4.23), and since the atomic beam follows the Poisson distribution, we obtain $\sum_{N_f} p(N_f)N_f = \langle N \rangle$ and $\sum_{N_f} p(N_f)N_f^2 = \langle N \rangle^2 + \langle N \rangle$. Then (Equation 4.23) becomes:

$$C_{eff}^2 R_s^2 F_N \int_{v=0}^{v=L/\tau} \rho(v)\frac{(L-v\tau)}{v}dv \cdot g_{single}^{(2)}(\tau) + C_{eff}^2 R_s^2 F_N^2 \int_v \rho(v)\frac{L}{v}dv \cdot \int_v \rho(v)\frac{L}{v}dv \quad (4.26)$$

Combining the denominator (Equation 4.18) and the numerator (Equation 4.26) we get $g^{(2)}(\tau)$:

$$g^{(2)}(\tau) = \frac{\int_{v=0}^{v=L/\tau}(1 - \frac{v\tau}{L})\frac{\rho(v)}{v}dv}{\int_v F_N\rho(v)\frac{L}{v}dv \int_v \frac{\rho(v)}{v}dv} \cdot g_{single}^{(2)}(\tau) + 1 \quad (4.27)$$

From (Equation 4.16), we can see that the first term in the denominator is actually $\langle N \rangle$. This yields
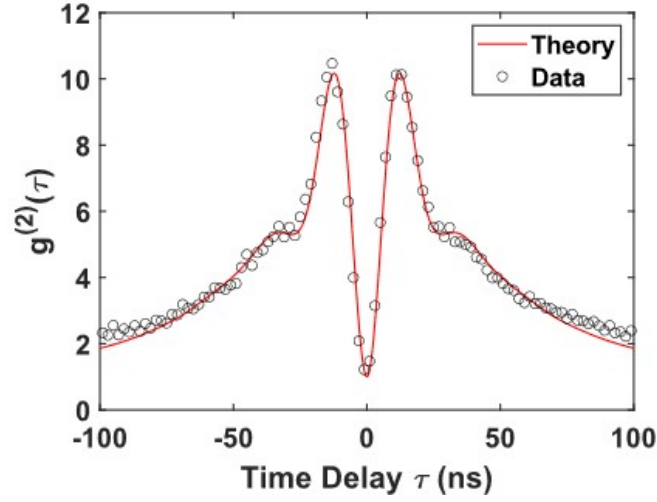
Figure 4.21: 78 °C thermal atomic beam $g^{(2)}(\tau)$ experimental data vs theory

the final expression for $g^2(\tau)$:

$$g^{(2)}(\tau) = \left(\frac{\int_{v=0}^{v=L/\tau} (1 - \frac{v\tau}{L}) \frac{\rho(v)}{v} dv}{\int_v \frac{\rho(v)}{v} dv} \right) \cdot \frac{g_{single}^{(2)}(\tau)}{\langle N \rangle} + 1 \tag{4.28}$$

The transit time correction is the term in parentheses above and includes an extra factor of $1/v$ in the integrand compared with the transit time correction derived in Ref [109]. Conceptually, it is because slower atoms contribute more photons per transit and thus have a higher weight in the $g^2(\tau)$. However, in Ref [109], the transit time correction is simply weighted by the velocity distribution of the flux $\rho(v)$.

We then fit this formula to our 78 °C thermal atomic beam data. The averaged atom number $\langle N \rangle$, the field of view L, and the Rabi frequency Ω in $g_{single}^2(\tau)$ are fitted to the data while $\rho(v)$ is the 78 °C atomic beam Maxwell-Boltzmann velocity distribution. Because of the intensity variance in the collecting region, the $g_{single}^2(\tau)$ is averaged over a Gaussian distributed Rabi frequency Ω. The fitted parameters are $\langle N \rangle = 0.138$, $L = 25 \ \mu$m and Ω is a Gaussian distribution with $\mu = 6\Gamma$, $\sigma = 1.5\Gamma$. The theory curve, together with the experimental data, is shown in Figure 4.21.

The difference between our transit correction factor and Ref [109] is shown in Figure 4.22. As we can see, the correction factor in Ref [109] drops too fast and is only half of our value at 100 ns. With the correction factor in Ref [109], a huge field of view 75 μm has to be used to roughly fit our
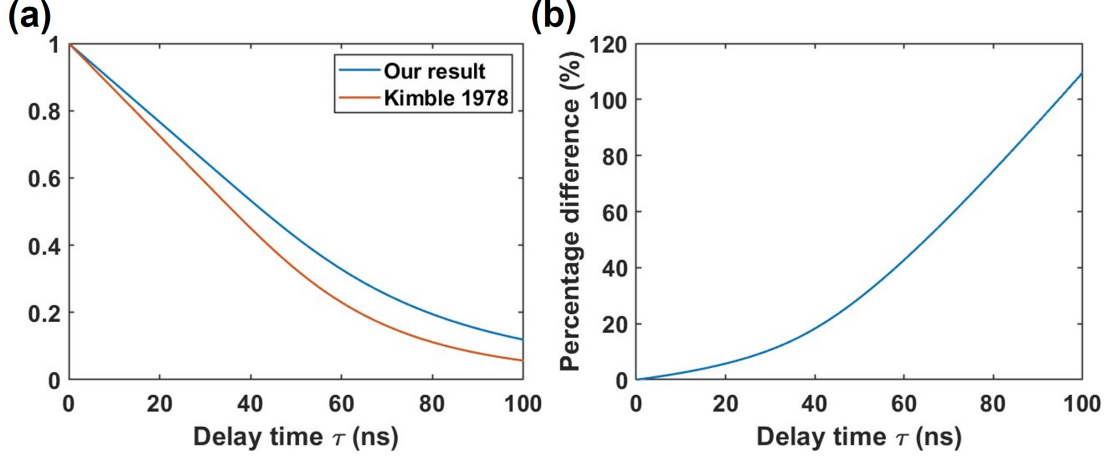
Figure 4.22: Difference between our transit time correction factor with Ref[109] for a 25 μm field of view. (a) The comparison between our transit time correction factor and Ref[109]. (b) The percentage difference, defined by the difference divided by Kimble's result, can be more than 100% at 100 ns time delay.

experimental data, which far exceeds the estimation of our field of view. Our Monte Carlo wave function simulation in the next section will provide another piece of evidence for our theory.

4.6.2 Monte Carlo wave function simulation

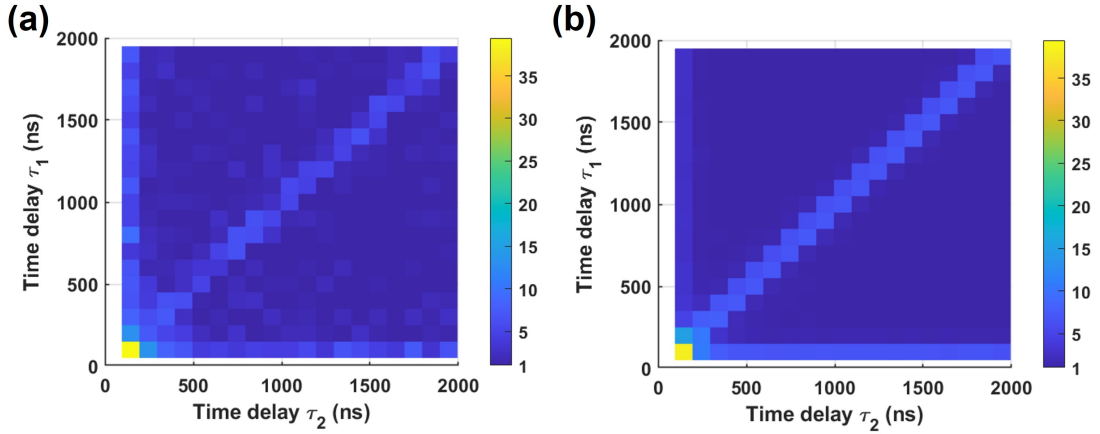Figure 4.23: (a) The experimental $g^3(\tau_1, \tau_2)$ value for 78 °C unfiltered thermal atomic beam. (b) The simulated $g^3(\tau_1, \tau_2)$

Monte Carlo wave function (MCWF) simulation is also implemented to test our theory. The Monte Carlo wave function (MCWF) simulation was designed to mimic what happened in our experimental system to calculate the photon correlation function. The atoms are generated according

to the Poisson distribution, and the velocities are chosen from the 78 °C atomic beam Maxwell Boltzmann distribution. The atoms then fly into a laser beam and interact with it. The wavefunctions are evolved according to the MCWF procedure [121]. When atoms are within the field of view of the fiber, their emitted photons' emission times are registered and stored. Then the same algorithm used to calculate experimental $g^{(3)}(\tau_1, \tau_2)$ is used on the simulation data. The result is shown in Figure 4.23. The colorbar is in the linear scale, and the simulation fits the data quite well. In the future, we can put some graphite in the system to absorb the accumulated vapor and average for a much longer time to reduce the three-photon-coincidences shot noise. Then, we can use a smaller time bin (4 ns) to see the dynamics near zero time delay.

Similar simulations are also done for the $g^{(2)}(\tau)$, and it agrees well with our theory (see Figure 4.24).
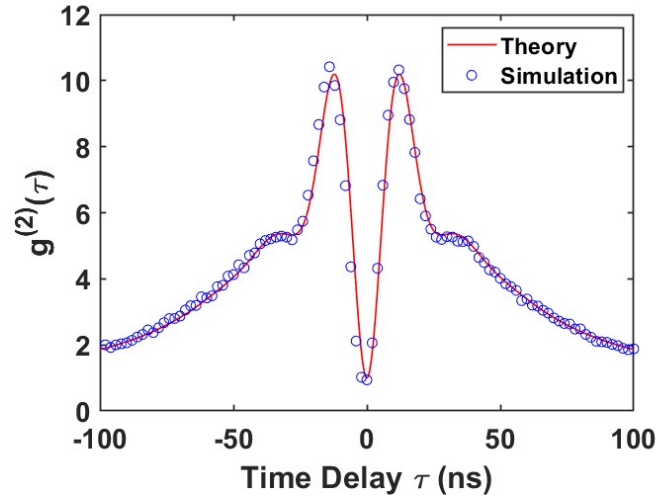
Figure 4.24: The simulated $g^{(2)}(\tau)$ with the same parameter we used to fit our experimental data, plotted together with our theoretical curve. $\langle N \rangle = 0.138$, $L = 25$ μm and Ω is a Gaussian distribution with $\mu = 6\Gamma$, $\sigma = 1.5\Gamma$.

4.6.3 Two fiber velocity detection

Similar to the single fiber second-order correlation theory, here we start with a formula for the coincidences distribution $C(\tau)d\tau$ in the time domain and convert the coincidences into the velocity domain later. As before, we ignore the background counts and only consider photons from the atomic beam. The effects of uncorrelated noise do not affect the accuracy of our method, which

will be shown in subsection 4.6.4. We set the field of view of the fiber to be d_f and the distance between two fibers in the objective plane to be d. We make the approximation that $d_f/d \ll 1$. Two components contribute to the coincidences:

$$C(\tau)d\tau = \text{uncorrelated\_term} + \text{correlated\_term} \tag{4.29}$$

The first uncorrelated term is the accidental coincidences generated by randomly having atoms at fiber A and atoms at fiber B at the same time. This term has no relationship with time delay τ and can be written as:

$$\text{uncorrelated\_term} = \int_v C_{eff} R_s F_N \rho(v) \frac{d_f}{v} dv \cdot \int_v C_{eff} R_s F_N \rho(v) \frac{d_f}{v} dv d\tau \tag{4.30}$$

Where $d\tau$ is the size of time bins for coincidences The correlated term comes from atoms with velocity $v_\tau = \frac{d \pm d_f}{\tau} \approx \frac{d}{\tau}$. We ignore d_f here since $\frac{d_f}{d}$ is small. These atoms emitted photons in fiber A and in fiber B at τ later:

$$C_{eff} R_s \frac{d_f}{v_\tau} \cdot C_{eff} R_s \frac{d_f}{v_\tau} F_N \rho(v_\tau) dv_\tau \tag{4.31}$$

Since $v_\tau = \frac{d}{\tau}$, put $dv_\tau = d\tau \cdot \frac{v_\tau^2}{d}$ into (Equation 4.31) we get:

$$\text{correlated\_term} = C_{eff}^2 R_s^2 \frac{d_f^2}{d} F_N \rho(v_\tau) d\tau \tag{4.32}$$

If we divided the uncorrelated term (Equation 4.30) on both side of (Equation 4.29), combine the definition of average atom number$\langle N \rangle$(Equation 4.16) we get:

$$C'(\tau) = 1 + \frac{\frac{d_f}{d}\rho(v_\tau)}{\langle N \rangle \int_v \frac{\rho(v)}{v} dv} \tag{4.33}$$

This formula shows that it needs to be in the single atom regime ($\langle N \rangle \ll 1$) so that the second correlated term is large enough to be detected. We can also see that when $\tau \to \infty$, $C'(\tau) \to 1$. Since $g_{AB}^{(2)}(\tau)$ is also the coincidences distribution normalized to infinity time delay, $C'(\tau)$ equals the cross-correlation $g_{AB}^{(2)}(\tau)$. Next, as we mentioned in the paper, that value $g_{AB}^{(2)}(\tau) - g_{AB}^{(2)}(\infty)$, after
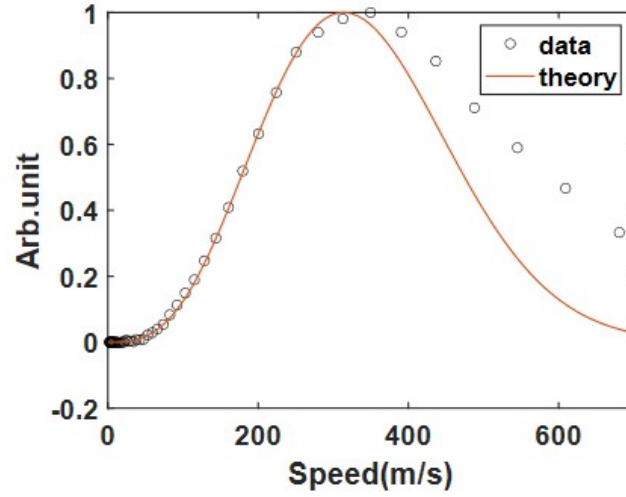
Figure 4.25: 70 °C thermal atomic beam experimental data after processing versus theory. The distance between two fibers in the objective plane d=55 μm.

normalization, is the coincidences probability density from atoms in time domain $n_{AB}(\tau)$, which is proportional to $\rho(v_\tau)$. Given $n_{AB}(\tau)d\tau = n_{AB}(v)dv$ and $\tau = \frac{d}{v}$, we can get the coincidences probability density in velocity space $n_{AB}(v) = n_{AB}(\tau) \cdot \frac{d}{v^2}$. And finally we can get $n_{AB}(v) \propto \rho(v) \cdot \frac{1}{v^2}$.

To calibrate our theory with data, we measured the unfiltered thermal atomic beam at 70 ° C with our two-fiber detector. The result is shown in Fig. Figure 4.25. The circles are the experimental data after processing, and the red curve is the theoretical curve for 70 °C atomic beam Maxwell Boltzmann distribution. The theory fits very well for velocities below 300 m/s which is the range we focused on. The error becomes larger when velocity is larger because $d_f/d \approx 0.45$ and it could have an uncertainty error around 22.5%. Also, because of the imperfect imaging, some atoms can emit photons into both fibers during the transit from fiber A to fiber B, which causes some spurious population at high velocity.

For $\Delta = -20$ MHz and $\Delta = -10$ MHz, as mentioned in the experiment section, the fast unpumped atoms and vapor are more than the selected atoms. To get the atom density of the selected atoms $\rho_s(v)$, we also measured the background $g_b^{(2)}(\tau)$ with the pump beam and probe beam only. We know the average atom number in the denominator is proportional to the photon count rate. Thus, if we assume $\int_v \frac{\rho(v)}{v}dv$ have roughly the same value with and without the repump beam, $(g^{(2)}(\tau) - 1) \cdot R$ is proportional to the atom density in both cases. As a result, the value $(g^{(2)}(\tau) -$

125

$1) \cdot R - (g_b^{(2)}(\tau) - 1) \cdot R_b$ is proportional to the density of selected atoms $\rho_s(v)$ and we can use the same logic with $n_{AB}(\tau)$ to calculate an accurate $\rho_s(v)$. By doing this, we managed to subtract most of the atoms from fast unpumped atoms and vapor. The different background vapor pressure when measuring $g_b^{(2)}(\tau)$ and $g^{(2)}(\tau)$ and the assumption of same $\int_v \frac{\rho(v)}{v} dv$ value limit the accuracy of this subtraction procedure.

4.6.4 Effects of uncorrelated noise

In the previous analysis, we all ignored the uncorrelated background photons. These photo counts can come from the laser scattering photons and the dark counts of SPCM. Here, we will analyze the effect of these background photons on the second order correlation function.

We start with the definition of $g^{(2)}(\tau)$ (Equation 4.13) and use the instantaneous photon rate $R_{A,B}(t)$ to represent $n_{A,B}(t)/\Delta t$, the averaged photon rate $R_{A,B}$ to represent $\langle n_{A,B}(t)/\Delta t\rangle$ for simplicity. We have

$$g^{(2)}(\tau) = \frac{\langle R_A(t)R_B(t+\tau)\rangle}{R_A R_B} \tag{4.34}$$

We denote $R_{sA,sB}(t)$ as the photon rate from our correlated signal (atoms), and $R_{bA,bB}(t)$ as the photon rate from the uncorrelated background (laser scattering, dark counts, etc.). The pure second order correlation function from our signal iss

$$g^{(2)}(\tau) = \frac{\langle R_{sA}(t)R_{sB}(t+\tau)\rangle}{R_{sA}R_{sB}} \tag{4.35}$$

Then, by putting $R_A(t) = R_{sA}(t) + R_{bA}(t)$, $R_B(t) = R_{sB}(t) + R_{bB}(t)$ and $R_{A,B} = R_{sA,sB} + R_{bA,bB}$ into Equation 4.34, we have the second order correlation function with both signal and background $g^{(2)}(\tau)'$:

$$\begin{aligned} g^{(2)}(\tau)' &= \frac{\langle (R_{sA}(t) + R_{bA}(t)) \cdot (R_{sB}(t+\tau) + R_{bB}(t+\tau)))\rangle}{(R_{sA} + R_{bA})(R_{sB} + R_{bB})} \\ &= \frac{\langle R_{sA}(t)R_{sB}(t+\tau)\rangle + \langle R_{sA}(t)R_{bB}(t+\tau) + R_{bA}(t)R_{sB}(t+\tau) + R_{bA}(t)R_{bB}(t+\tau)\rangle}{(R_{sA} + R_{bA})(R_{sB} + R_{bB})} \end{aligned} \tag{4.36}$$

There is no correlation between the signal and the background, we have $\langle R_{sA}(t)R_{bB}(t+\tau)\rangle =$

$R_{sA}R_{bB}$. The background photons are also not correlated, $\langle R_{bA}(t)R_{bB}(t+\tau)\rangle = R_{bA}R_{bB}$. Combined with Equation 4.35, we get :

$$g^{(2)}(\tau)' = \frac{g^{(2)}(\tau) \cdot R_{sA} \cdot R_{sB} + R_{sA}R_{bB} + R_{bA}R_{sB} + R_{bA}R_{bB}}{(R_{sA} + R_{bA})(R_{sB} + R_{bB})} \tag{4.37}$$

With the Hanbury-Brown and Twiss configuration, the signal and background photons are both split 50/50 to channel A and channel B. Assuming SPCM A and SPCM B have the same detection efficiency, we have $R_{sA} = R_{sB}$, $R_{bA} = R_{bB}$. By dividing R_{sA}^2 on both the numerator and denominator and setting the signal-to-noise ratio $k = R_{sA}/R_{bA}$, we have:

$$g^{(2)}(\tau)' = \frac{g^{(2)}(\tau) + 2/k + 1/k^2}{(1 + 1/k)^2} = 1 + \frac{g^{(2)}(\tau) - 1}{(1 + 1/k)^2} \tag{4.38}$$

We can see that when the signal-to-noise ratio is high, $g^{(2)}(\tau)' \approx g^{(2)}(\tau)$. However, when the uncorrelated background is higher, the correlated component will drop depending on the signal-to-noise ratio: $g^{(2)}(\tau)' - 1 = (g^{(2)}(\tau) - 1)/(1 + 1/k)^2$. This conclusion also applies to the cross-correlation case when two fibers have the same count rate.

We can see here why our two-fiber correlation experiment can still be precise with the laser scattering background. From subsection 4.6.3 and Equation 4.33, we know that our theory utilizes the proportionality between $g_{AB}^{(2)}(\tau) - 1$ and the atom probability density $\rho(v)$. Thus, the constant factor $1/(1 + 1/k)^2$ will not affect our calculation. Monte Carlo wave function simulation with two detection regions is conducted to test our theory. The simulation method has been described in subsection 4.6.2. One thing we added in the simulation is that after collecting all the photon time tags from atoms, random time tags (Poisson distributed) are generated and added to the data. The number of added time tags can be chosen to have different signal-to-noise ratios k. The result is shown in Figure 4.26. Figure 4.26 (a) shows the data with no background, the peak value is 7.3. Figure 4.26 (b) and (c) show the data with a signal-to-noise ratio of 1 and 1/3, the peak values are 2.6 and 1.4, respectively. The changes in peak value agree with our formula, and the shape remains the same.
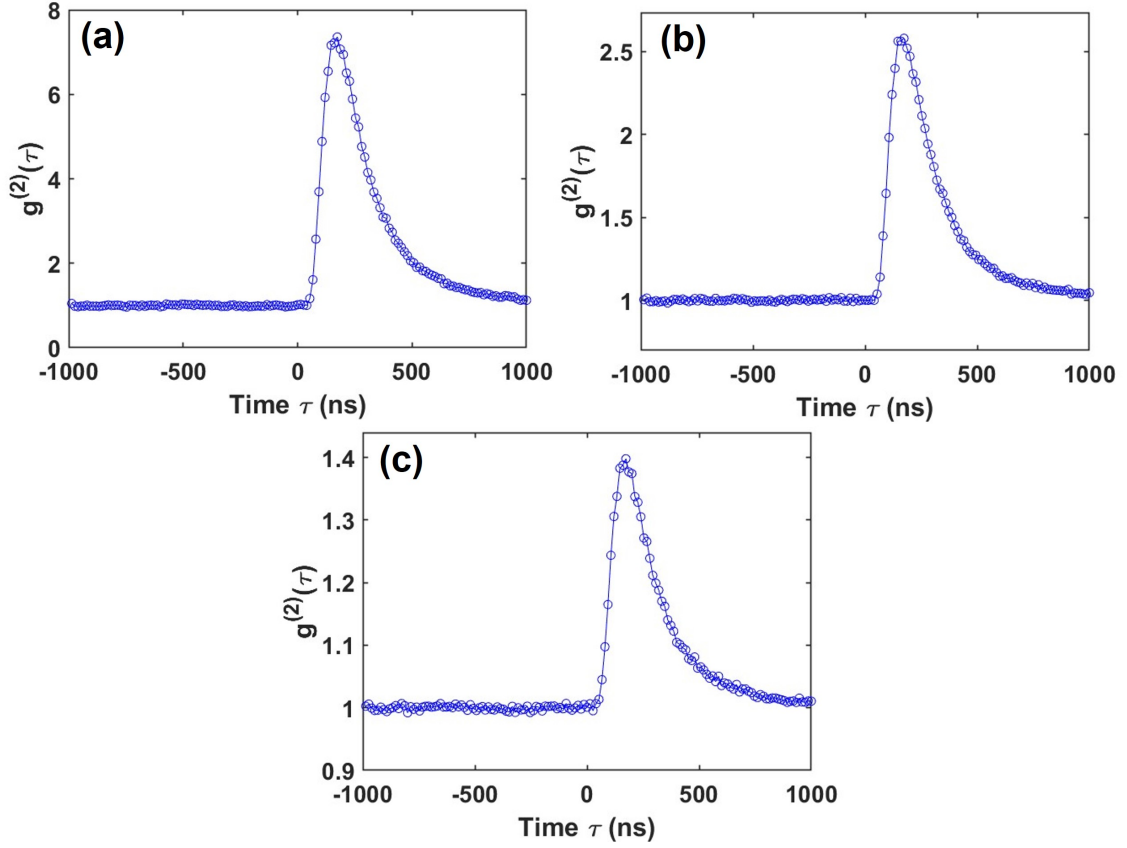
Figure 4.26: Monte Carlo wave function simulation with different signal-to-noise ratio (SNR). A 70°thermal atomic beam passes two detection regions (mimic two fiber tips) with $\langle N \rangle$=0.06. (a) $g^{(2)}(\tau)$ with no background noise. The peak value is 7.3 (b) $g^{(2)}(\tau)$ with SNR=1. The peak value is 2.6. (c) $g^{(2)}(\tau)$ with SNR=1/3. The peak value is 1.4. The changes in peak value agree with our formula.

4.7 Discussion

In summary, we demonstrated a novel approach to isolating and detecting the slow atoms within a thermal atomic beam. The single-atom nature of the system is proved by taking single-photon correlation measurements. $g^{(2)}(\tau)$ and $g^{(3)}(\tau_1, \tau_2)$ are measured, and their large values show potential to be used as photon pair and photon triplet sources. Our experiments show the possibilities of the 'bottom-up' approach to thermal quantum systems. Figure 4.27 illustrates an array of "mesoscopic" cells within a thermal vapor. The array need only be partially ordered to be useful, provided one knows the population of each cell accurately. This can be determined with a high-resolution microscope and single photon detection. Since the field of view with our fiber is 25 μm, individual
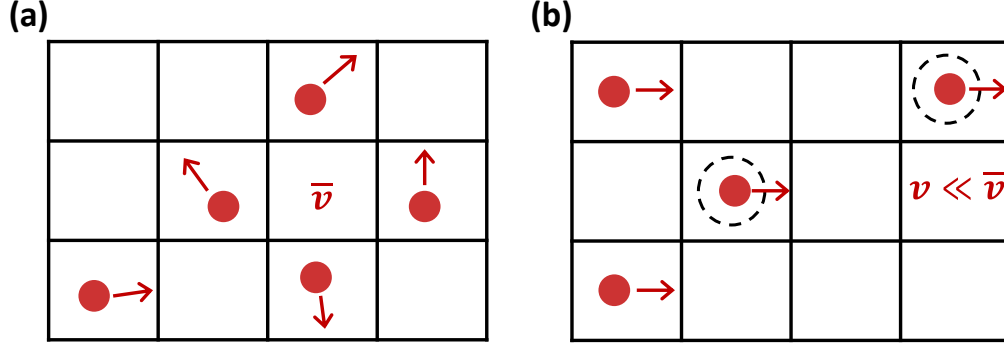
Figure 4.27: Concept of the bottom-up approach to room temperature quantum information processing with neutral atoms under a high-resolution microscope. The field of view is divided into mesoscopic cells (size $\sim 25~\mu$m), with less than one atom per cell on average, to ensure the dynamics are dominated by single emitters. Only a few cells are shown for simplicity. (a) Ordinary vapor with randomly oriented velocities of magnitude $\bar{v}$. Individual atoms cannot be tracked in this case. (b) Three-dimensional velocity selection with $v \ll \bar{v}$. Atoms move much slower, and their motion can be tracked from one cell to the next. This constitutes a new paradigm for a bottom-up approach to quantum information processing. For example, select atoms (shown in dashed circles) can be entangled with one another by a joint detection of the photons from the corresponding cells.

cells are taken to be 25 μm in size. Around 1600 cells can be constructed within a field of view $\sim 1 \times 1$ mm. However, at typical thermal velocities of 300 m/s, atoms cannot be observed for more than ~ 83 ns within one cell, which is too short for most purposes. Moreover, atoms move in random directions and cannot be tracked. We demonstrated that slow single atoms could be isolated whose three-dimensional velocity vector is 20 times smaller in magnitude than the mean, which extends the observation time to $> 1~\mu$s and simultaneously enables tracking of atoms across cells since all atoms travel in the same direction. In the future, these cells could be constructed by an array of fibers on the image plane. With the signals from the fiber array, fast electronics can be used to observe and manipulate single atoms in an atomic beam and construct a quantum system. Future work could also use a single photon camera to directly observe an entire array of slow atoms generated using the technique described in this chapter for applications in quantum imaging [122], and quantum memories [95, 96].

Appendices

This appendix will show some figures and data that are not presented in the main text in chapter 4.

The two fiber coincidences data with detuning $\Delta = -5$ MHz is shown in Figure A.1. After comparing with Figure 4.15 (a) and (c), we can notice that the peak location moved to slower velocity, but the noise around zero is a bit too much. The reason is that the signal from atoms is less than 200 photons/s, but the unwanted photons from the laser, vapor, and unpumped fast atoms can quickly reach 2000 photons/s. With a growing vapor component, an even longer experiment time cannot provide a better SNR. With better control of the vapor, the data with -5 MHz detuning could be improved.
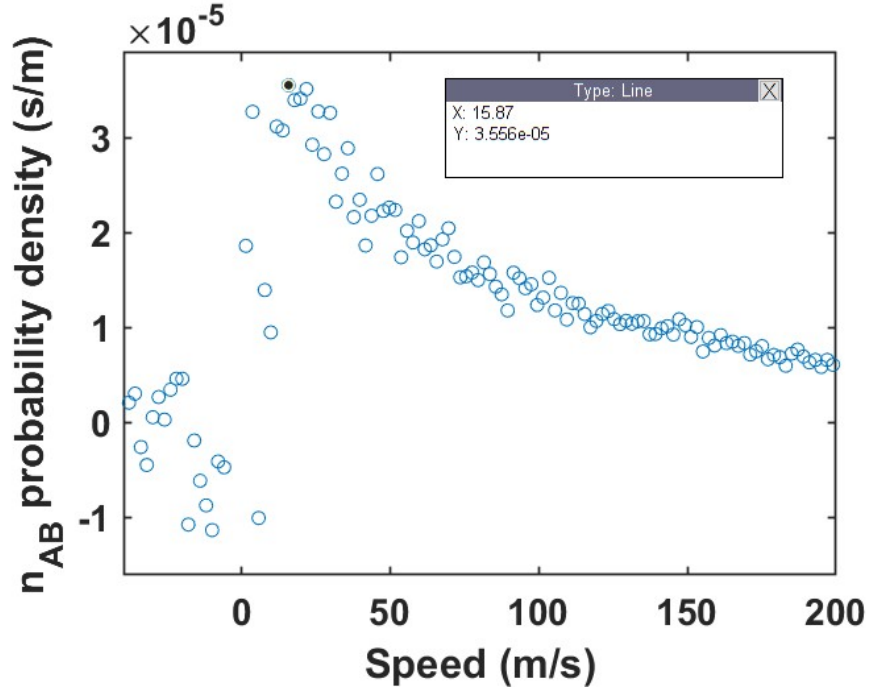
Figure A.1: Two fiber coincidences distribution in velocity domain with detuning $\Delta = -5$ MHz.

Figure A.2 shows the experimental data of the second order correlation function $g^{(2)}(\tau)$ with different laser intensities. The data was taken with thermal beams generated by our setup with an old oven at 70°C. We can see that different laser intensities caused different Rabi frequencies, which modified the photon pair's time interval. Using a strong laser and a smaller field of view, we can have photon pairs very close together in time.

Figure A.2: The measured second order correlation function $g^{(2)}(\tau)$ with different laser intensity and 70 degree atomic beams. (a) Probe power equals 0.12 I_{sat}. (b) Probe power equals 4.2 I_{sat}. I_{sat} is the saturation intensity.

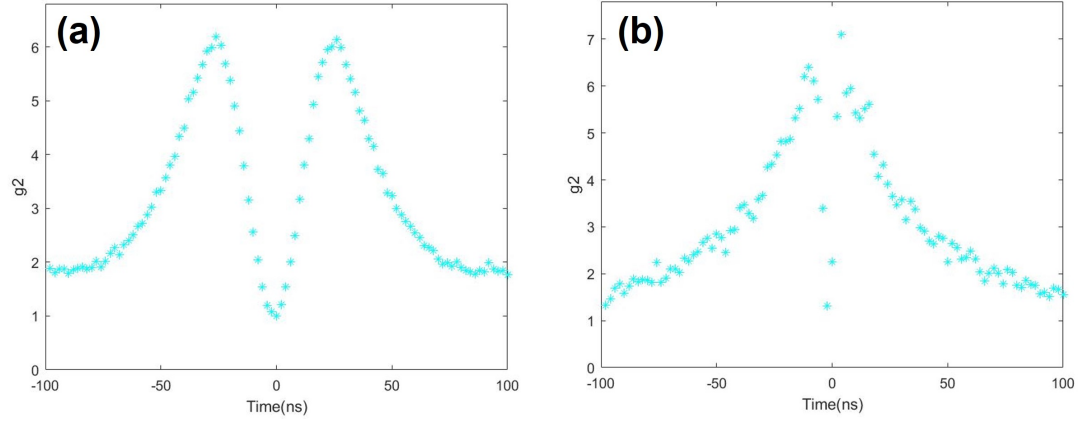The theory and our observations about second order correlation function are not limited to a specific transition. Here, we switched the probe beam to couple to the transition F=1 to F'=0 in ^{87}Rb D2 line. The excited state of this transition only has one hyperfine level (F'=0, m=0), and the ground state only has three hyperfine levels (F=1, m=-1,0,+1). Thus, this transition could be used to create polarization-entangled photon pairs or entangle two different atoms by a joint detection [123]. Figure A.3 shows the experimental data. The excitation probe beam is linearly polarized with an intensity of $0.55I_{sat}$. $g^{(2)}(\tau)$ value drops much faster than other cases because F=1 to F'=0 transition have dark state (m=1,m=-1) for linearly polarized light, and multiphoton are less likely to be generated. Thus, this transition created another unique photon statistics.
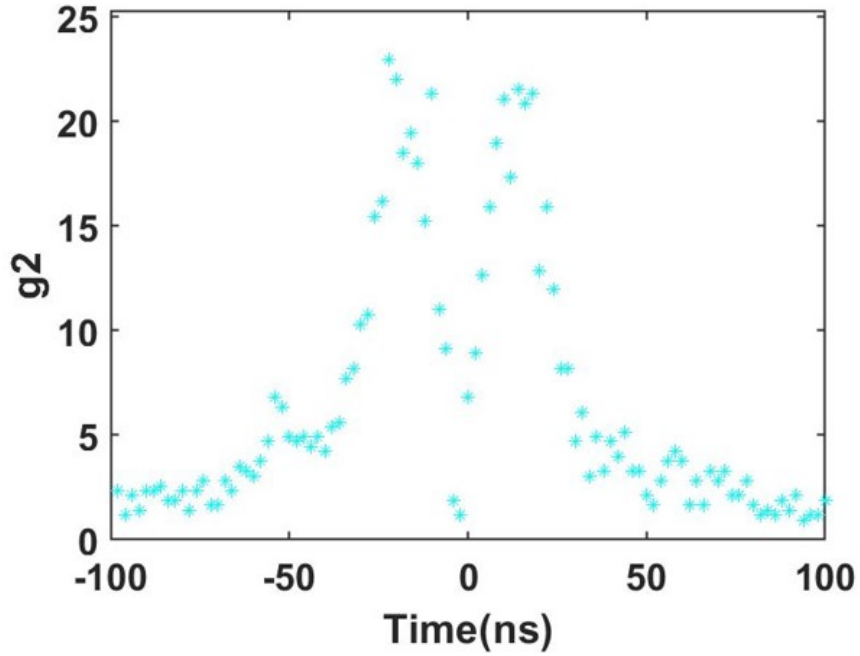

Figure A.3: The measured second order correlation function $g^{(2)}(\tau)$ from F=1 to F'=0. The probe beam is linearly polarized with an intensity of 0.55 I_{sat}.

The third order correlation function $g^{(3)}(\tau_1, \tau_2)$ that was shown in Figure 4.19 (a) used a large time bin size of 100 ns × 100 ns to have more averaging and reduce the shot noise. However, the resolution of $g^{(3)}(\tau_1, \tau_2)$ is severely compromised because of the large time bin size. Figure A.4 shows $g^{(3)}(\tau_1, \tau_2)$ calculated from the same photon tags but with smaller time bins and smaller time ranges. We can see that the value of $g^{(3)}(\tau_1, \tau_2)$ is even higher because of the improved resolution. The maximum $g^{(3)}(\tau_1, \tau_2)$ is around 90 for a 30 ns × 30 ns time bin.
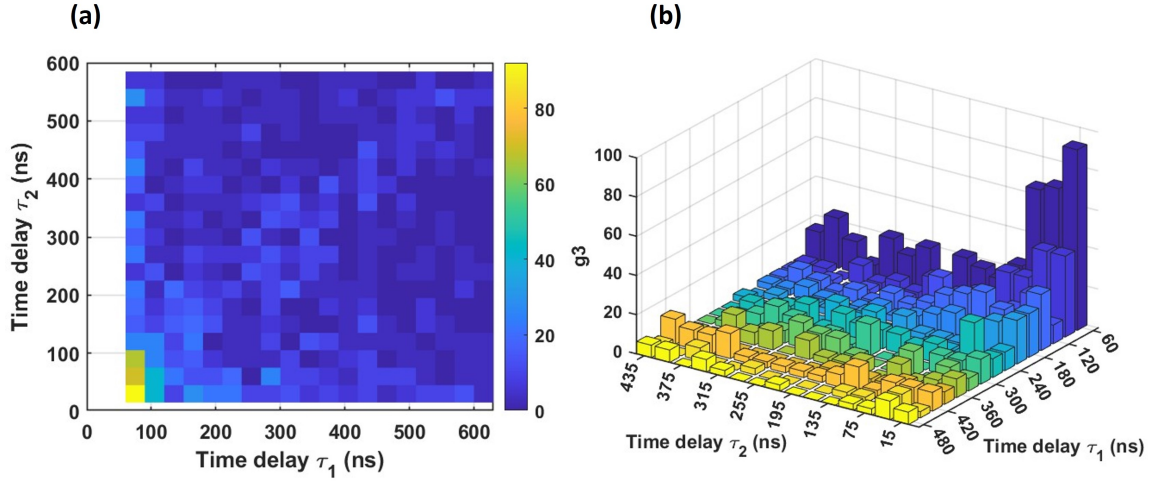

Figure A.4: The measured third order correlation function $g^{(3)}(\tau_1, \tau_2)$ with 30 ns time bin for better resolution. The data is from 78°C unfiltered thermal atomic beam. (a) A 2D color plot of $g^{(3)}(\tau_1, \tau_2)$. (b) A bar plot of $g^{(3)}(\tau_1, \tau_2)$.

MISCELLANEOUS WORK

This appendix will briefly talk about some of the works I have done that didn't result in any publication.

B.1 Rydberg atoms

A blue laser centered around 488 nm was built to create Rydberg atoms in our miniature atomic beams. The blue laser diode is bought from beamq.com at a price of $ 99. A Thorlabs TE-Cooled laser diode Mount was modified to accommodate this diode, and old homemade heat sinks and mounts were used to build this laser. Figure B.1 (a) shows the first beautiful blue light we got from this laser diode. The aspheric lens was installed later to collimate the laser beam, and a special laser grating was used to create an external cavity diode laser (ECDL). Figure B.1 (b) shows the diagram for generating Rydberg atoms. The probe beam is from our standard Toptica laser at 780
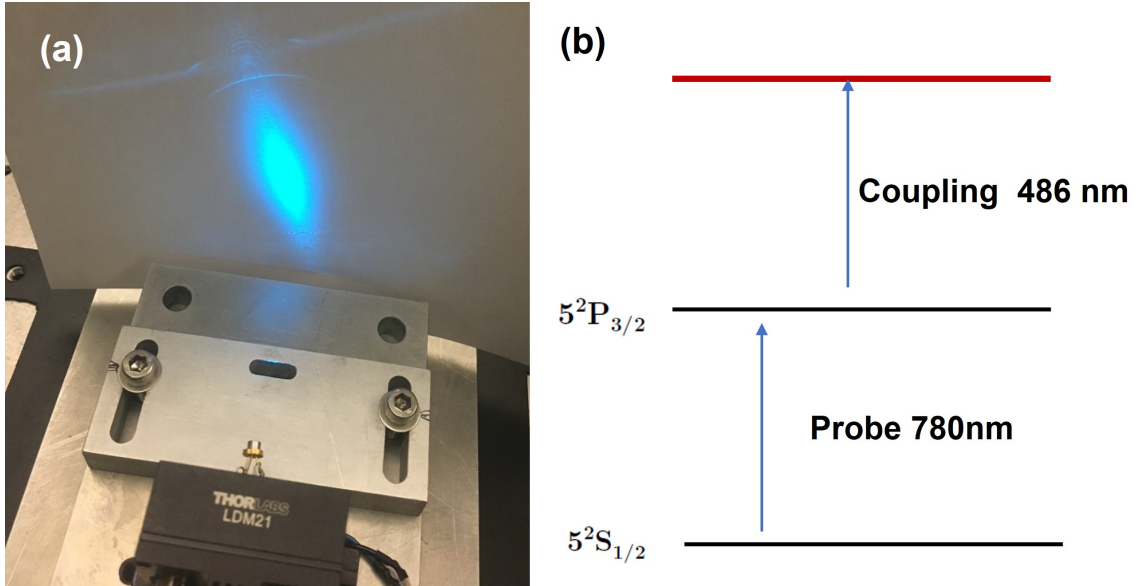

Figure B.1: (a) The first light of the homemade blue laser. The grating and aspheric lens for the diode has not been added. (b) The diagram for generating Rydberg states with rubidium atoms.
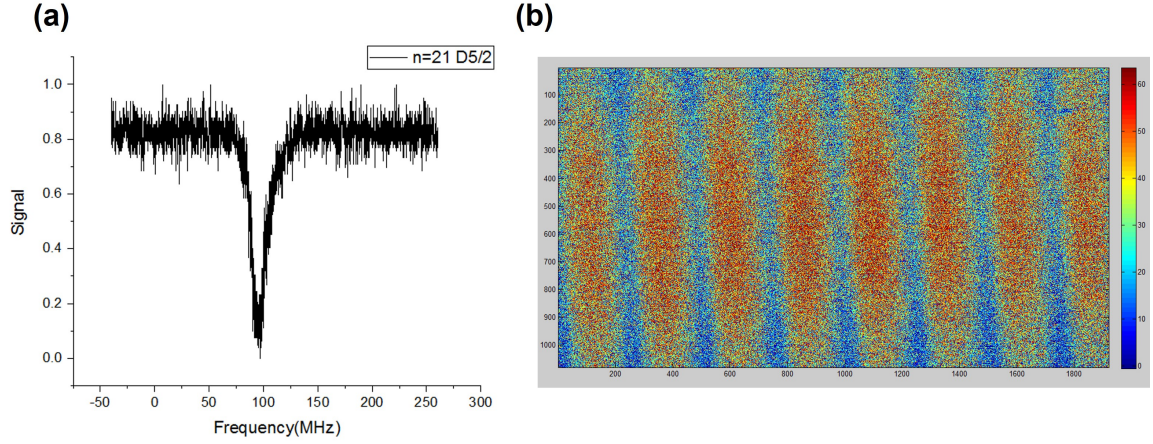
Figure B.2: (a) The EIT effect data showing rydberg atoms generation. The x-axis is the frequency detuned from some point near 486 nm, and the y-axis is the normalized fluorescence signal. (b) The spatial image of the reduced fluorescence indicates the distribution of Rydberg atoms.

nm, which is tuned to $5^2S_{1/2}$ to $5^2P_{3/2}$. The coupling beam is from the blue laser tuned around 486 nm to couple $5^2P_{3/2}$ to $n^2D_{3/2}$ and $n^2D_{5/2}$. Figure B.2 shows the data we collected. The probe beam is locked to $5^2S_{1/2}$ to $5^2P_{3/2}$ transition, and the frequency of the coupling beam is scanned to find the Rydberg resonance transition. The reduced absorption of the probe beam is also called electromagnetically-induced transparency (EIT) effect. The peak in Figure B.2 (a) has a FWHM of 18 MHz, which shows that Rydberg atoms were created and can be used to detect external fields. The frequency of the coupling beam was monitored, and its frequency at 617279.466 GHz will couple the atoms into 21 $^2D_{5/2}$. Figure B.2 (b) showed the spatial distribution of the reduced fluorescence, indicating the distribution of Rydberg atoms.

Figure B.3: (a) The SolidWorks model of the chip integrated with fibers on a copper adapter. (b) The Solidworks model for the Teflon fiber feedthrough we used.

B.2   Fiber on chip

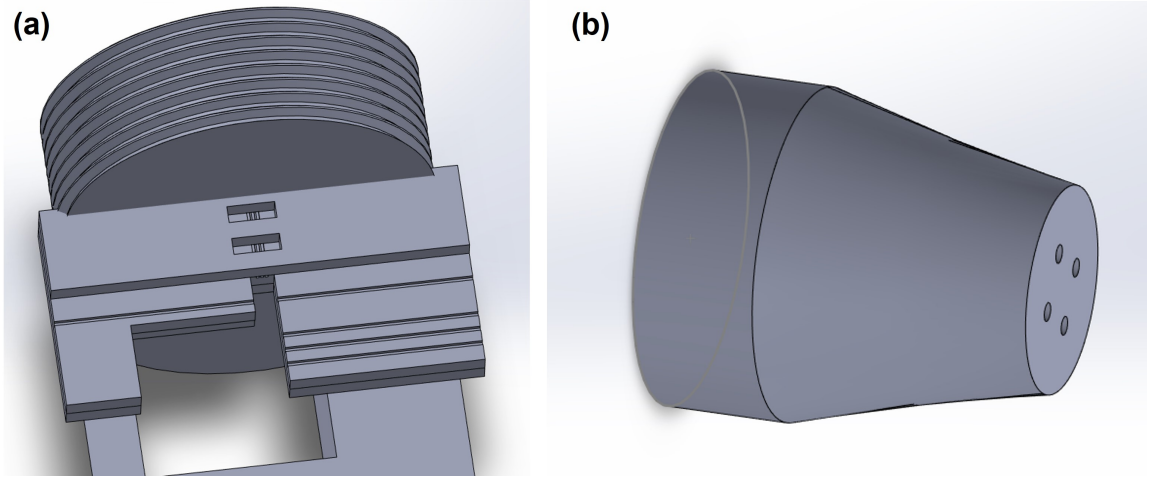Fibers are integrated with atomic channels on the same silicon chip to form a miniature device. As shown in Figure B.3, this chip composes of three layers of 500 μm thick silicon wafers. All three wafers and the channels on the wafers are cut by using the femtosecond laser micromachining techniques. The bottom layer is a flat wafer to provide a smooth surface and thermal uniformity for the other two layers. Three atomic channels were cut in the middle layer with $100 \ \mu m \times 100 \ \mu$m cross-section. Five fiber channels were also cut to align the fiber center with the atomic channels. Two gaps were cut on the top capping wafer to allow off-axis atoms to escape, forming a cascaded collimator. Three layers are glued together by Masterbond epoxy to form an integrated device. The device is then fixed on a copper adapter for further connection with rubidium vapors.

A great fiber feedthrough inspired by Ref [83] was fabricated and tested. As shown in Figure B.4, we found that we can have one or four holes (possibly even more) on the Teflon feedthrough to accommodate multiple fibers. The Teflon feedthrough is then used with a KF40 to Swagelock adapter. With the fibers installed, we first hand tightened it mildly, then tightened it 180 degrees with a wrench. A leak detection was conducted, and no leak was detected. We also found that the fiber was fine with this procedure, and the feedthrough can be used multiple times.

After using the fiber feedthrough, the fibers were cleaved, aligned within the fiber channels, fixed by a self-locking tweezer, and glued with Masterbond epoxy. The coating section of the fiber

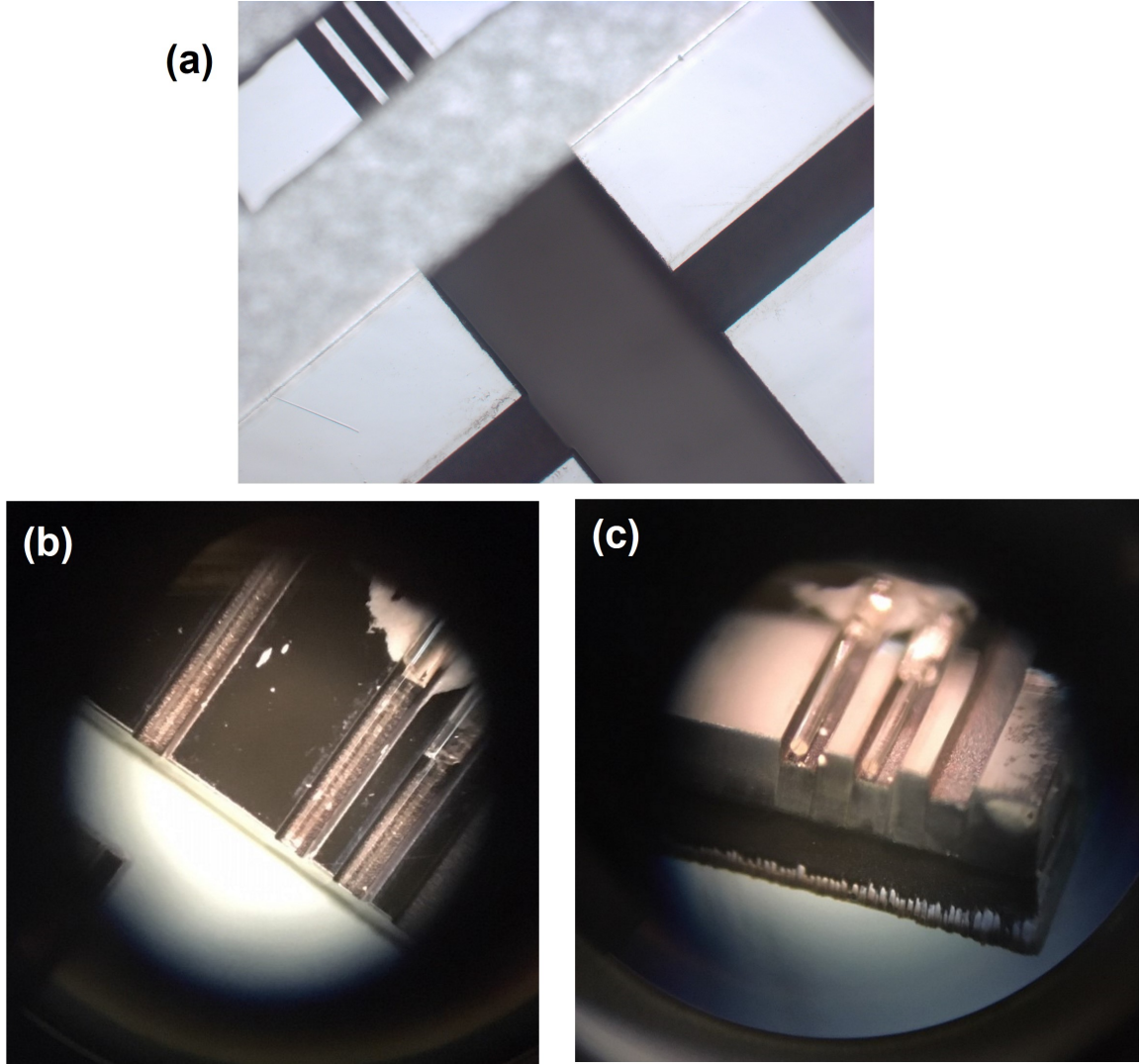Figure B.4: The optical images of the fiber on chip. (a) Three atomic channels and gaps in the capping wafer to form a cascaded collimator can be seen in the top left. Two fiber channels can be seen facing each other can be seen in the bottom right. (b) and (c) The images after fibers are glued on the channels on chip.

is glued on the chip to avoid cracking the fiber. Figure B.4 shows the optical image of the final device.

REFERENCES

[1] W. S. Bakr, J. I. Gillen, A. Peng, S. Fölling, and M. Greiner, "A quantum gas microscope for detecting single atoms in a hubbard-regime optical lattice," *Nature*, vol. 462, no. 7269, pp. 74–77, 2009.

[2] L. W. Cheuk *et al.*, "Quantum-gas microscope for fermionic atoms," *Physical review letters*, vol. 114, no. 19, p. 193 001, 2015.

[3] A. Reiserer and G. Rempe, "Cavity-based quantum networks with single atoms and optical photons," *Reviews of Modern Physics*, vol. 87, no. 4, p. 1379, 2015.

[4] S. Daiss *et al.*, "A quantum-logic gate between distant quantum-network modules," *Science*, vol. 371, no. 6529, pp. 614–617, 2021.

[5] M. Brekenfeld, D. Niemietz, J. D. Christesen, and G. Rempe, "A quantum network node with crossed optical fibre cavities," *Nature Physics*, vol. 16, no. 6, pp. 647–651, 2020.

[6] M. Endres *et al.*, "Atom-by-atom assembly of defect-free one-dimensional cold atom arrays," *Science*, vol. 354, no. 6315, pp. 1024–1027, 2016.

[7] H. Bernien *et al.*, "Probing many-body dynamics on a 51-atom quantum simulator," *Nature*, vol. 551, no. 7682, pp. 579–584, 2017.

[8] A. M. Kaufman and K.-K. Ni, "Quantum science with optical tweezer arrays of ultracold atoms and molecules," *Nature Physics*, vol. 17, no. 12, pp. 1324–1333, 2021.

[9] J. Kitching, "Chip-scale atomic devices," *Applied Physics Reviews*, vol. 5, no. 3, p. 031 302, 2018.

[10] M. Keil, O. Amit, S. Zhou, D. Groswasser, Y. Japha, and R. Folman, "Fifteen years of cold matter on the atom chip: Promise, realizations, and prospects," *Journal of modern optics*, vol. 63, no. 18, pp. 1840–1885, 2016.

[11] J. McGilligan, K. Gallacher, P. Griffin, D. Paul, A. Arnold, and E. Riis, "Micro-fabricated components for cold atom sensors," *Review of Scientific Instruments*, vol. 93, no. 9, p. 091 101, 2022.

[12] M. Trupke *et al.*, "Pyramidal micromirrors for microsystems and atom chips," *Applied physics letters*, vol. 88, no. 7, p. 071 116, 2006.

[13] M. Vangeleyn, P. F. Griffin, E. Riis, and A. S. Arnold, "Single-laser, one beam, tetrahedral magneto-optical trap," *Optics express*, vol. 17, no. 16, pp. 13 601–13 608, 2009.

[14] C. Nshii *et al.*, "A surface-patterned chip as a strong source of ultracold atoms for quantum technologies," *Nature nanotechnology*, vol. 8, no. 5, pp. 321–324, 2013.

[15] J. P. McGilligan, P. F. Griffin, R. Elvin, S. J. Ingleby, E. Riis, and A. S. Arnold, "Grating chips for quantum technologies," *Scientific reports*, vol. 7, no. 1, pp. 1–7, 2017.

[16] R. Elvin *et al.*, "Cold-atom clock based on a diffractive optic," *Optics Express*, vol. 27, no. 26, pp. 38 359–38 366, 2019.

[17] W. Hänsel, P. Hommelhoff, T. Hänsch, and J. Reichel, "Bose–einstein condensation on a microelectronic chip," *Nature*, vol. 413, no. 6855, pp. 498–501, 2001.

[18] R. Folman, P. Krüger, D. Cassettari, B. Hessmo, T. Maier, and J. Schmiedmayer, "Controlling cold atoms using nanofabricated surfaces: Atom chips," *Physical Review Letters*, vol. 84, no. 20, p. 4749, 2000.

[19] T. M. Roach and D. Henclewood, "Novel rubidium atomic beam with an alkali dispenser source," *Journal of Vacuum Science & Technology A: Vacuum, Surfaces, and Films*, vol. 22, no. 6, pp. 2384–2387, 2004.

[20] H. Nishino, Y. Furuya, and T. Ono, "Micro-fabricated vapor cells with sealed rb atoms by distillation at wafer level and two-step bonding for miniature atomic clocks," *Optics Express*, vol. 29, no. 26, pp. 44 316–44 321, 2021.

[21] S. Knappe *et al.*, "A microfabricated atomic clock," *Applied Physics Letters*, vol. 85, no. 9, pp. 1460–1462, 2004.

[22] V. Maurice *et al.*, "Microfabricated vapor cells filled with a cesium dispensing paste for miniature atomic clocks," *Applied Physics Letters*, vol. 110, no. 16, p. 164 103, 2017.

[23] M. T. Hummon *et al.*, "Photonic chip for laser stabilization to an atomic vapor with 10- 11 instability," *Optica*, vol. 5, no. 4, pp. 443–449, 2018.

[24] Y. Sebbag, E. Talker, A. Naiman, Y. Barash, and U. Levy, "Demonstration of an integrated nanophotonic chip-scale alkali vapor magnetometer using inverse design," *Light: Science & Applications*, vol. 10, no. 1, pp. 1–8, 2021.

[25] D. Sheng, A. R. Perry, S. P. Krzyzewski, S. Geller, J. Kitching, and S. Knappe, "A microfabricated optically-pumped magnetic gradiometer," *Applied physics letters*, vol. 110, no. 3, p. 031 106, 2017.

[26] W. C. Griffith, S. Knappe, and J. Kitching, "Femtotesla atomic magnetometry in a microfabricated vapor cell," *Optics express*, vol. 18, no. 26, pp. 27 167–27 172, 2010.

[27] R. Thompson, G. Rempe, and H. Kimble, "Observation of normal-mode splitting for an atom in an optical cavity," *Physical Review Letters*, vol. 68, no. 8, p. 1132, 1992.

[28] X. Maitre *et al.*, "Quantum memory with a single photon in a cavity," *Physical review letters*, vol. 79, no. 4, p. 769, 1997.

[29] R. G. Hulet and D. Kleppner, "Rydberg atoms in" circular" states," *Physical review letters*, vol. 51, no. 16, p. 1430, 1983.

[30] K. Safinya, J. Delpech, F. Gounand, W. Sandner, and T. Gallagher, "Resonant rydberg-atom-rydberg-atom collisions," *Physical Review Letters*, vol. 47, no. 6, p. 405, 1981.

[31] H. J. Kimble, M. Dagenais, and L. Mandel, "Photon antibunching in resonance fluorescence," *Physical Review Letters*, vol. 39, no. 11, p. 691, 1977.

[32] M. Brune *et al.*, "Quantum rabi oscillation: A direct test of field quantization in a cavity," *Physical review letters*, vol. 76, no. 11, p. 1800, 1996.

[33] M. Brune *et al.*, "Observing the progressive decoherence of the "meter" in a quantum measurement," *Physical Review Letters*, vol. 77, no. 24, p. 4887, 1996.

[34] Q. A. Turchette, C. J. Hood, W. Lange, H. Mabuchi, and H. J. Kimble, "Measurement of conditional phase shifts for quantum logic," *Physical Review Letters*, vol. 75, no. 25, p. 4710, 1995.

[35] P. Blythe and B. Varcoe, "A cavity-qed scheme for cluster-state quantum computing using crossed atomic beams," *New Journal of Physics*, vol. 8, no. 10, p. 231, 2006.

[36] G. M. Carter and D. E. Pritchard, *Recirculating atomic beam oven*, 1978.

[37] A. Pailloux, T. Alpettaz, and E. Lizon, "Candlestick oven with a silica wick provides an intense collimated cesium atomic beam," *Review of scientific instruments*, vol. 78, no. 2, p. 023 102, 2007.

[38] C. Li *et al.*, "Cascaded collimator for atomic beams traveling in planar silicon devices," *Nature Communications*, vol. 10, no. 1, pp. 1–8, 2019.

[39] H. Beijerinck and N. Verster, "Velocity distribution and angular distribution of molecular beams from multichannel arrays," *Journal of Applied Physics*, vol. 46, no. 5, pp. 2083–2091, 1975.

[40] P. Clausing, "Stationary flow of very dilute gases," *Physica*, vol. 9, pp. 65–80, 1929.

[41] R. Senaratne, S. V. Rajagopal, Z. A. Geiger, K. M. Fujiwara, V. Lebedev, and D. M. Weld, "Effusive atomic oven nozzle design using an aligned microcapillary array," *Review of Scientific Instruments*, vol. 86, no. 2, p. 023 105, 2015.

[42] C. Li *et al.*, "Robust characterization of microfabricated atomic beams on a six-month time scale," *Physical Review Research*, vol. 2, no. 2, p. 023 239, 2020.

[43] D. A. Steck, *Quantum and atom optics*, 2007.

[44] W. Demtröder, *Laser spectroscopy*. Springer, 1982, vol. 2.

[45] R. Kersevan and J.-L. Pons, "Introduction to molflow+: New graphical processing unit-based monte carlo code for simulating molecular flows and for calculating angular coefficients in the compute unified device architecture environment," *Journal of Vacuum Science & Technology A: Vacuum, Surfaces, and Films*, vol. 27, no. 4, pp. 1017–1023, 2009.

[46] SAES Getters USA Inc., Colorado Springs, CO.

[47] C. Wieman, G. Flowers, and S. Gilbert, "Inexpensive laser cooling and trapping experiment for undergraduate laboratories," *American Journal of Physics*, vol. 63, no. 4, pp. 317–330, 1995.

[48] J. Fortágh, A. Grossmann, T. W. Hänsch, and C. Zimmermann, "Fast loading of a magneto-optical trap from a pulsed thermal source," *Journal of Applied Physics*, vol. 84, no. 12, pp. 6499–6501, 1998.

[49] K. L. Moore, T. P. Purdy, K. W. Murch, S. Leslie, S. Gupta, and D. M. Stamper-Kurn, "Collimated, single-pass atom source from a pulsed alkali metal dispenser for laser-cooling experiments," *Review of Scientific Instruments*, vol. 76, no. 2, p. 023 106, 2005.

[50] A. E. Dorche, B. Wei, C. Raman, and A. Adibi, "High-quality-factor microring resonator for strong atom–light interactions using miniature atomic beams," *Optics Letters*, vol. 45, no. 21, pp. 5958–5961, 2020.

[51] H. Alaeian, R. Ritter, M. Basic, R. Löw, and T. Pfau, "Cavity qed based on room temperature atoms interacting with a photonic crystal cavity: A feasibility study," *Applied Physics B*, vol. 126, no. 2, pp. 1–10, 2020.

[52] B. Wei, A. Crawford, Y. Andeweg, L. Zhuo, C. Li, and C. Raman, "Collimated versatile atomic beam source with alkali dispensers," *Applied Physics Letters*, vol. 120, no. 14, p. 144 001, 2022.

[53] P. Molenaar, P. Van der Straten, H. Heideman, and H. Metcalf, "Diagnostic technique for zeeman-compensated atomic beam slowing: Technique and results," *Physical Review A*, vol. 55, no. 1, p. 605, 1997.

[54] N. Ramsey, *Molecular beams*. Oxford University Press, 1985.

[55] J.-M. Raimond, M. Brune, and S. Haroche, "Manipulating quantum entanglement with atoms and photons in a cavity," *Reviews of Modern Physics*, vol. 73, no. 3, p. 565, 2001.

[56] D. Chang, J. Douglas, A. González-Tudela, C.-L. Hung, and H. Kimble, "Colloquium: Quantum matter built from nanoscopic lattices of atoms and photons," *Reviews of Modern Physics*, vol. 90, no. 3, p. 031 002, 2018.

[57] A. Frisk Kockum, A. Miranowicz, S. De Liberato, S. Savasta, and F. Nori, "Ultrastrong coupling between light and matter," *Nature Reviews Physics*, vol. 1, no. 1, pp. 19–40, 2019.

[58] J. P. Dowling and G. J. Milburn, "Quantum technology: The second quantum revolution," *Philosophical Transactions of the Royal Society of London. Series A: Mathematical, Physical and Engineering Sciences*, vol. 361, no. 1809, pp. 1655–1674, 2003.

[59] H. J. Kimble, "The quantum internet," *Nature*, vol. 453, no. 7198, pp. 1023–1030, 2008.

[60] C. Hood, M. Chapman, T. Lynn, and H. Kimble, "Real-time cavity qed with single atoms," *Physical review letters*, vol. 80, no. 19, p. 4157, 1998.

[61] A. Boca, R. Miller, K. Birnbaum, A. Boozer, J. McKeever, and H. Kimble, "Observation of the vacuum rabi spectrum for one trapped atom," *Physical review letters*, vol. 93, no. 23, p. 233 603, 2004.

[62] C. Hamsen, K. N. Tolazzi, T. Wilk, and G. Rempe, "Two-photon blockade in an atom-driven cavity qed system," *Physical review letters*, vol. 118, no. 13, p. 133 604, 2017.

[63]   T. Aoki *et al.*, "Observation of strong coupling between one atom and a monolithic microresonator," *Nature*, vol. 443, no. 7112, pp. 671–674, 2006.

[64]   B. Dayan, A. Parkins, T. Aoki, E. Ostby, K. Vahala, and H. Kimble, "A photon turnstile dynamically regulated by one atom," *Science*, vol. 319, no. 5866, pp. 1062–1065, 2008.

[65]   S. Kato and T. Aoki, "Strong coupling between a trapped single atom and an all-fiber cavity," *Physical review letters*, vol. 115, no. 9, p. 093 603, 2015.

[66]   S. Kato *et al.*, "Observation of dressed states of distant atoms with delocalized photons in coupled-cavities quantum electrodynamics," *Nature communications*, vol. 10, no. 1, pp. 1–6, 2019.

[67]   J. D. Thompson *et al.*, "Coupling a single trapped atom to a nanoscale optical cavity," *Science*, vol. 340, no. 6137, pp. 1202–1205, 2013.

[68]   A. P. Burgers, L. S. Peng, J. A. Muniz, A. C. McClung, M. J. Martin, and H. J. Kimble, "Clocked atom delivery to a photonic crystal waveguide," *Proceedings of the National Academy of Sciences*, vol. 116, no. 2, pp. 456–465, 2019.

[69]   T.-H. Chang, B. M. Fields, M. E. Kim, and C.-L. Hung, "Microring resonators on a suspended membrane circuit for atom–light interactions," *Optica*, vol. 6, no. 9, pp. 1203–1210, 2019.

[70]   T. Aoki *et al.*, "Efficient routing of single photons by one atom and a microtoroidal cavity," *Physical review letters*, vol. 102, no. 8, p. 083 601, 2009.

[71]   L. C. Andreani, G. Panzarini, and J.-M. Gérard, "Strong-coupling regime for quantum boxes in pillar microcavities: Theory," *Physical Review B*, vol. 60, no. 19, p. 13 276, 1999.

[72]   A. Yariv, "Universal relations for coupling of optical power between microresonators and dielectric waveguides," *Electronics letters*, vol. 36, no. 4, pp. 321–322, 2000.

[73]   V. Van, *Optical microring resonators: theory, techniques, and applications*. CRC Press, 2016.

[74]   M. L. Gorodetsky, A. D. Pryamikov, and V. S. Ilchenko, "Rayleigh scattering in high-q microspheres," *JOSA B*, vol. 17, no. 6, pp. 1051–1057, 2000.

[75]   Y. Zhao *et al.*, "Visible nonlinear photonics via high-order-mode dispersion engineering," *Optica*, vol. 7, no. 2, pp. 135–141, 2020.

[76] K. Dieckmann, R. Spreeuw, M. Weidemüller, and J. Walraven, "Two-dimensional magneto-optical trap as a source of slow atoms," *Physical Review A*, vol. 58, no. 5, p. 3891, 1998.

[77] J. Ramirez-Serrano, N. Yu, J. M. Kohel, J. R. Kellogg, and L. Maleki, "Multistage two-dimensional magneto-optical trap as a compact cold atom beam source," *Optics Letters*, vol. 31, no. 6, pp. 682–684, 2006.

[78] D. O'Shea, C. Junge, J. Volz, and A. Rauschenbeutel, "Fiber-optical switch controlled by a single atom," *Physical Review Letters*, vol. 111, no. 19, p. 193 601, 2013.

[79] I. Shomroni, S. Rosenblum, Y. Lovsky, O. Bechler, G. Guendelman, and B. Dayan, "All-optical routing of single photons by a one-atom switch controlled by a single photon," *Science*, vol. 345, no. 6199, pp. 903–906, 2014.

[80] M. B. Squires *et al.*, "Ex vacuo atom chip bose-einstein condensate," *Applied Physics Letters*, vol. 109, no. 26, p. 264 101, 2016.

[81] J. A. Stickney *et al.*, "Tunable axial potentials for atom-chip waveguides," *Physical Review A*, vol. 96, no. 5, p. 053 606, 2017.

[82] L. Cheng, S. Mao, Z. Li, Y. Han, and H. Fu, "Grating couplers on silicon photonics: Design principles, emerging trends and practical issues," *Micromachines*, vol. 11, no. 7, p. 666, 2020.

[83] E. R. Abraham and E. A. Cornell, "Teflon feedthrough for coupling optical fibers into ultrahigh vacuum systems," *Applied optics*, vol. 37, no. 10, pp. 1762–1763, 1998.

[84] R. Marchetti, C. Lacava, L. Carroll, K. Gradkowski, and P. Minzioni, "Coupling strategies for silicon photonics integrated chips," *Photonics Research*, vol. 7, no. 2, pp. 201–239, 2019.

[85] X. Mu, S. Wu, L. Cheng, and H. Fu, "Edge couplers in silicon photonic integrated circuits: A review," *Applied Sciences*, vol. 10, no. 4, p. 1538, 2020.

[86] T.-H. Chang, X. Zhou, M. Zhu, B. M. Fields, and C.-L. Hung, "Efficiently coupled microring circuit for on-chip cavity qed with trapped atoms," *Applied Physics Letters*, vol. 117, no. 17, p. 174 001, 2020.

[87] S.-P. Yu *et al.*, "Nanowire photonic crystal waveguides for single-atom trapping and strong light-matter interactions," *Applied Physics Letters*, vol. 104, no. 11, p. 111 103, 2014.

[88]   X. Luan, J.-B. Béguin, A. P. Burgers, Z. Qin, S.-P. Yu, and H. J. Kimble, "The integration of photonic crystal waveguides with atom arrays in optical tweezers," *Advanced Quantum Technologies*, p. 2 000 008, 2020.

[89]   S. Ashraf *et al.*, "Determination of complex refractive index of su-8 by kramers–kronig dispersion relation method at the wavelength range 2.5–22.0 μm," *Journal of Quantitative Spectroscopy and Radiative Transfer*, vol. 224, pp. 309–311, 2019.

[90]   A. N. Otte, D. Garcia, T. Nguyen, and D. Purushotham, "Characterization of three high efficiency and blue sensitive silicon photomultipliers," *Nuclear Instruments and Methods in Physics Research Section A: Accelerators, Spectrometers, Detectors and Associated Equipment*, vol. 846, pp. 106–125, 2017.

[91]   S. Gundacker and A. Heering, "The silicon photomultiplier: Fundamentals and applications of a modern solid-state photon detector," *Physics in Medicine & Biology*, vol. 65, no. 17, 17TR01, 2020.

[92]   C. Shu *et al.*, "Subnatural-linewidth biphotons from a doppler-broadened hot atomic vapour cell," *Nature communications*, vol. 7, no. 1, pp. 1–5, 2016.

[93]   R. Willis, F. Becerra, L. Orozco, and S. Rolston, "Correlated photon pairs generated from a warm atomic ensemble," *Physical Review A*, vol. 82, no. 5, p. 053 842, 2010.

[94]   T.-M. Zhao, Y. S. Ihn, and Y.-H. Kim, "Direct generation of narrow-band hyper-entangled photons," *Physical review letters*, vol. 122, no. 12, p. 123 607, 2019.

[95]   D. Main *et al.*, "Preparing narrow velocity distributions for quantum memories in room-temperature alkali-metal vapors," *Physical Review A*, vol. 103, no. 4, p. 043 105, 2021.

[96]   G. Buser, R. Mottola, B. Cotting, J. Wolters, and P. Treutlein, "Single-photon storage in a ground-state vapor cell quantum memory," *PRX Quantum*, vol. 3, p. 020 349, 2 Jun. 2022.

[97]   F. Ripka, H. Kübler, R. Löw, and T. Pfau, "A room-temperature single-photon source based on strongly interacting rydberg atoms," *Science*, vol. 362, no. 6413, pp. 446–449, 2018.

[98]   F. Becerra, R. Willis, S. Rolston, and L. Orozco, "Nondegenerate four-wave mixing in rubidium vapor: The diamond configuration," *Physical review A*, vol. 78, no. 1, p. 013 834, 2008.

[99]   T. Fukuhara *et al.*, "Microscopic observation of magnon bound states and their dynamics," *Nature*, vol. 502, no. 7469, pp. 76–79, 2013.

[100] R. Ozeri, N. Katz, J. Steinhauer, and N. Davidson, "Colloquium: Bulk bogoliubov excitations in a bose-einstein condensate," *Reviews of Modern Physics*, vol. 77, no. 1, p. 187, 2005.

[101] D. M. Stamper-Kurn and M. Ueda, "Spinor bose gases: Symmetries, magnetism, and quantum dynamics," *Reviews of Modern Physics*, vol. 85, no. 3, p. 1191, 2013.

[102] J. Wilson *et al.*, "Trapping alkaline earth rydberg atoms optical tweezer arrays," *Physical review letters*, vol. 128, no. 3, p. 033 201, 2022.

[103] C. D. Bruzewicz, J. Chiaverini, R. McConnell, and J. M. Sage, "Trapped-ion quantum computing: Progress and challenges," *Applied Physics Reviews*, vol. 6, no. 2, p. 021 314, 2019.

[104] K. Singer *et al.*, "Colloquium: Trapped ions as quantum bits: Essential numerical tools," *Reviews of Modern Physics*, vol. 82, no. 3, p. 2609, 2010.

[105] C. Kurtsiefer, P. Zarda, S. Mayer, and H. Weinfurter, "The breakdown flash of silicon avalanche photodiodes-back door for eavesdropper attacks?" *Journal of Modern Optics*, vol. 48, no. 13, pp. 2039–2047, 2001.

[106] R. Newman, "Visible light from a silicon p- n junction," *Physical review*, vol. 100, no. 2, p. 700, 1955.

[107] T. A. Laurence, S. Fore, and T. Huser, "Fast, flexible algorithm for calculating photon correlations," *Optics letters*, vol. 31, no. 6, pp. 829–831, 2006.

[108] R. Loudon, *The quantum theory of light*. OUP Oxford, 2000.

[109] H. Kimble, M. Dagenais, and L. Mandel, "Multiatom and transit-time effects on photon-correlation measurements in resonance fluorescence," *Physical Review A*, vol. 18, no. 1, p. 201, 1978.

[110] F. Diedrich and H. Walther, "Nonclassical radiation of a single stored ion," *Physical review letters*, vol. 58, no. 3, p. 203, 1987.

[111] S. Gerber, D. Rotter, L. Slodička, J. Eschner, H. Carmichael, and R. Blatt, "Intensity-field correlation of single-atom resonance fluorescence," *Physical review letters*, vol. 102, no. 18, p. 183 601, 2009.

[112] M. K. Tey *et al.*, "Strong interaction between light and a single trapped atom without the need for a cavity," *Nature Physics*, vol. 4, no. 12, pp. 924–927, 2008.

[113] S. Du, J. Wen, M. H. Rubin, and G. Yin, "Four-wave mixing and biphoton generation in a two-level system," *Physical review letters*, vol. 98, no. 5, p. 053 601, 2007.

[114] A. Aspect, G. Roger, S. Reynaud, J. Dalibard, and C. Cohen-Tannoudji, "Time correlations between the two sidebands of the resonance fluorescence triplet," *Physical Review Letters*, vol. 45, no. 8, p. 617, 1980.

[115] C. Schrama, G. Nienhuis, H. Dijkerman, C. Steijsiger, and H. Heideman, "Intensity correlations between the components of the resonance fluorescence triplet," *Physical Review A*, vol. 45, no. 11, p. 8045, 1992.

[116] S.-Y. Baek and Y.-H. Kim, "Spectral properties of entangled photon pairs generated via frequency-degenerate type-i spontaneous parametric down-conversion," *Physical Review A*, vol. 77, no. 4, p. 043 807, 2008.

[117] C. Couteau, "Spontaneous parametric down-conversion," *Contemporary Physics*, vol. 59, no. 3, pp. 291–304, 2018.

[118] M. Khoshnegar *et al.*, "A solid state source of photon triplets based on quantum dot molecules," *Nature communications*, vol. 8, no. 1, pp. 1–8, 2017.

[119] S. Krapick, B. Brecht, H. Herrmann, V. Quiring, and C. Silberhorn, "On-chip generation of photon-triplet states," *Optics express*, vol. 24, no. 3, pp. 2836–2849, 2016.

[120] H. Hübel, D. R. Hamel, A. Fedrizzi, S. Ramelow, K. J. Resch, and T. Jennewein, "Direct generation of photon triplets using cascaded photon-pair sources," *Nature*, vol. 466, no. 7306, pp. 601–603, 2010.

[121] K. Mølmer, Y. Castin, and J. Dalibard, "Monte carlo wave-function method in quantum optics," *JOSA B*, vol. 10, no. 3, pp. 524–538, 1993.

[122] M. Genovese, "Real applications of quantum imaging," *Journal of Optics*, vol. 18, no. 7, p. 073 002, 2016.

[123] J. Hofmann *et al.*, "Heralded entanglement between widely separated atoms," *Science*, vol. 337, no. 6090, pp. 72–75, 2012.